Power Scaling of Ultrashort Pulses by Spatial and Temporal Coherent Combining

Dissertation

zur Erlangung des akademischen Grades

doctor rerum naturalium (Dr. rer. nat.)

vorgelegt dem Rat der Physikalisch-Astronomischen Fakultät

der Friedrich-Schiller-Universität Jena

von M.Sc. Marco Kienel

geboren am 28. September 1984 in Meerane

Gutachter

1. Prof. Dr. Jens Limpert, Universität Jena

2. Prof. Dr. Malte Kaluza, Universität Jena

3. Prof. Dr. Almantas Galvanauskas, Universität Michigan

Tag der Disputation: 12.09.2017

Contents

1. Introduction

Solid-state lasers are the tool of choice for the generation of intense ultrashort optical pulses, which are key for a plethora of applications, for example in industry [1], medicine [2] and science [3–5]. The demands on the driving laser system (for example to initiate a desired physical process, maximize the processing speed or minimize the data acquisition time) go hand in hand with the continuous advances of these applications. Particularly prominent scientific examples of such demanding applications are the generation of coherent extreme ultraviolet radiation with high harmonic generation [6–8], the generation of attosecond pulses [4, 9] and, even more ambitious, laser-particle acceleration [10–12]. The driving-laser requirements for these applications target at peak powers of multiple-GW and multiple-TW, respectively, while multi-kHz repetition rates are desired. Thus, a lot of effort has been made to push the performance of laser systems towards high pulse energy at high repetition rate, i.e. high average power, while simultaneously maintaining a high beam quality and all other system parameters.

There are established laser concepts available today that either operate at extremely high pulse energy [13] and peak power (up to the PW-level [14–17]) or at high average power (up to the kW-level [18–21]). However, a multitude of physical effects, such as beam-quality degradation induced by thermo-optic effects [22] or mode instabilities [23–25], as well as pulse-quality degradation induced by nonlinear effects [26] or even optically-induced damage [27], hamper the simultaneous maximization of both parameters. Despite some further advances, favored by established power-scaling techniques such as chirped-pulse amplification (CPA) [28], it is not expected that those ambitious requirements will be fulfilled in the near future.

Coherent combination of the ultrashort pulses [29] delivered by an amplifier array, referred to as spatial combination, has proven to be a promising power-scaling approach. With each amplifier being added to the array, an improvement in both pulse energy and average power can be achieved. As the amplifier count has to considerably grow to reach the ambitious energy being targeted, divided-pulse amplification (DPA) [30–32], in the scope of temporal combination, can be applied as another scaling concept. This concept involves the coherent pulse stacking of pulse bursts and can be employed to improve the

energy extraction from an amplifier.

Although both techniques are applicable to numerous laser concepts [33–36], fibers are particularly well-suited for them. This is, in part, because their waveguide structure provides reproducible and excellent beam quality, which is a requirement for efficient combination. Moreover, their high single-pass gain and their simple design allows for straightforward amplifier-array architectures. While fibers can handle very high average powers [21] (limited currently only by the onset of mode instabilities), the high signal intensities arising from the confinement of the light in small cores cause detrimental nonlinearities or even damage, hampering the energy extraction [37]. A further increase in pulse energy, and therewith peak power, requires larger core diameters of the fibers, but this approach is currently limited by manufacturing tolerances. It is true that this can be improved using a longer stretched pulse duration in state-of-the-art fiber-CPA systems. However, this would require extremely large and expensive gratings in the compressor in order to keep the pulse compression efficient. These are difficult to manufacture and increase the system footprint. This brings DPA into the spotlight, as a means to access more of the extractable energy from the fiber, which will be the focus of this thesis.

In particular, fiber amplifiers doped with ytterbium are considered in this work. At the beginning of this thesis, the highest reported pulse energy achieved with DPA (temporal combination) was $430\,\mu\text{J}$ at an average power of $77\,\text{W}$ [38], corresponding to a peak power of $\sim 1\,\text{GW}$. In terms of spatial combination an average power of $88\,\text{W}$ with $500\,\mu\text{J}$ [39] pulse energy or $30\,\text{W}$ with $3\,\text{mJ}$ [40], corresponding to a peak power of $5.4\,\text{GW}$, were demonstrated. In this work, average-power and energy values well above those performance figures could be achieved by merging both combination concepts.

The thesis is structured as follows: In Chapter 2 the mathematical description of ultrashort pulses and polarization properties is introduced. Furthermore, the amplification of ultrashort pulses and saturation-induced dynamics are considered. In Chapter 3, a distinction is made between spatial and temporal combination techniques that are briefly introduced and categorized. Using a polarization-based combination approach, the impact of beam- and pulse-parameter mismatches on the combination efficiency are discussed. Subsequently, these considerations are transferred to the principle of DPA and the effect of saturation at high energy extraction is analyzed. The requirements for the experimental realization are finalized in Chapter 4 by discussing the active stabilization techniques required for coherent combination and pulse stacking. In Chapter 5, the experiments done in the frame of this thesis are presented. First, the focus is on the temporal combination, i.e. DPA, and the experimental results are compared with theoretical simulations based on the model described in previous chapters. Finally, both combination approaches

are merged and the spatio-temporal combination of ultrashort pulses is demonstrated in a proof-of-principle experiment. In this regard, the phase stabilization of actively-controlled temporal and spatio-temporal combination setups is investigated. Applying the findings to a high-power fiber amplification system, a performance beyond current state-of-the-art has been achieved. The thesis will be summarized in Chapter 6, after a brief discussion of future perspectives.

2. Fundamentals

In this chapter, the fundamentals of the physical phenomena that can be found in ultrafast fiber amplifiers and that are relevant for this work are summarized. Thus, in Sec. 2.1 and in Sec. 2.2, ytterbium-doped fibers are briefly explained and the amplification of ultrashort pulses is considered. Subsequently, the polarization states of light and their manipulation are described in Sec. 2.3. Finally, the propagation of ultrashort pulses through nonlinear dispersive media is considered in Sec. 2.4. This knowledge will be necessary for the amplification of divided pulses and the pulse-division and -combination technique employed in this work.

2.1. Ytterbium-Doped Fibers

Fibers possess unique properties, such as an efficient heat dissipation which results in an excellent power-independent beam quality. These properties are rooted in their waveguide nature and makes fibers robust against environmental perturbations [41]. Today, the most common host material for high-power active fibers is silica glass doped with ytterbium (Yb) [42]. In Fig. 2.1a the effective emission and absorption cross-sections in Yb-doped germanosilicate glass are shown. They provide a broad amplification range ($\sim 970\,\text{nm}$ to $\sim 1200\,\text{nm}$ [43]), which is advantageous for the amplification of ultrashort pulses that are typically centered around $1030\,\text{nm}$. There are two absorption local maxima (at $\sim 915\,\text{nm}$ and $\sim 976\,\text{nm}$), which are addressable by commercially available semiconductor pump diodes. When pumping at $976\,\text{nm}$ and emitting at $1030\,\text{nm}$, the quantum defect[1] is comparably small ($\sim 5\%$), keeping the thermal load at low levels and allowing for high amplification efficiency.

More importantly, the achievable performance with a fiber depends on its particular design. In Fig. 2.1b the schematic cross-sectional index profile of a standard step-index fiber is depicted. This is the simplest structure to guide several transverse modes, which is achieved by total internal reflection between the core and the cladding that have slightly different refractive indexes $n_{\text{clad}} < n_{\text{co}}$. The number of supported modes is determined

---

[1]The quantum defect is the difference between the pump photon energy and the signal photon energy.
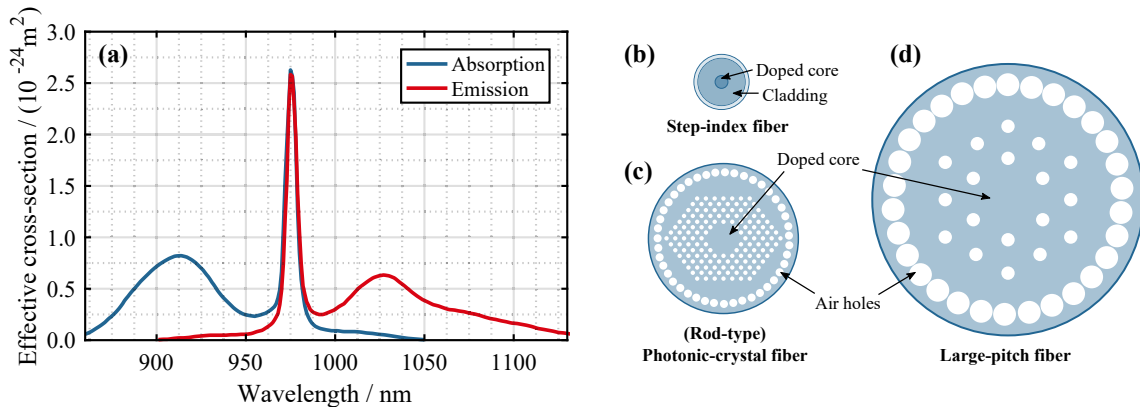
Figure 2.1.: (a) Effective absorption and emission cross-sections in Yb-doped germanosilicate glass [42]. Representation of different fiber designs: (b) step-index fiber [45], (c) photonic-crystal fiber [46], and (d) large-pitch fiber [41] (illustration not to scale).

by the normalized frequency parameter $V = k r_{co} \text{NA}$, where $\text{NA} = \sqrt{n_{co}^2 - n_{clad}^2}$ is the numerical aperture, r_{co} is the radius of the core and $k = 2\pi/\lambda$ is the wave number with the wavelength λ [44]. Single-mode operation is ensured in case of $V \lesssim 2.4$, which is typically the preferred regime, since this fundamental mode (for weakly guiding fibers the so-called LP_{01}) possesses a nearly Gaussian shape (compare to Fig. 2.2 in the following section).

State-of-the-art high-power fibers utilize the double-cladding technique. While the signal is guided by the inner cladding, the pump is guided by a larger surrounding cladding. This allows the use of low-brightness high-power pump diodes, whose light can be easily coupled in the cladding and absorbed by the core as it propagates along the fiber. An essential parameter for double-clad fibers is the overlap of both the pump (p) and the signal (s) with the doped area and is given by[2]

$$\Gamma_{s/p} = \frac{\int_{A_{dop}} |F(x,y)|^2 dA}{\int |F(x,y)|^2 dA} = \left\{ \begin{array}{l} \Gamma_s \approx 1 - \exp\left(-2\dfrac{A_{dop}}{A_{mod}}\right), \\[2ex] \Gamma_p \approx \dfrac{A_{dop}}{A_{clad}}, \end{array} \right\} \tag{2.1}$$

with $F(x,y)$ being the transverse mode profile and A_{dop}, A_{mod} and A_{clad} being the doped, the mode and the cladding areas, respectively.

For the amplification of ultrashort pulses, nonlinear effects (see Subsec. 2.4.2) can have a detrimental effect on the pulse. The crucial factors are the fiber length, which is kept as short as possible to still provide sufficient gain, and the effective mode-field diameter [41]

---

[2]Γ_s is obtained assuming a Gaussian beam with cross-section A_{mod} (the beam radius is defined at $1/e^2$) being transmitted through a circular aperture with A_{dop}. Γ_p is obtained assuming the pump radiation within A_{clad} as flat-top profile.

$$\mathrm{MFD} = 2\sqrt{\frac{A_{\mathrm{eff}}}{\pi}}, \tag{2.2}$$

with the effective area A_{eff} (depending on the modal distribution and, therefore, on the fiber parameters) being defined as [26]

$$A_{\mathrm{eff}} = \frac{\left[\int\limits_{-\infty}^{\infty}\int\limits_{-\infty}^{\infty}|F(x,y)|^2 \mathrm{d}x\mathrm{d}y\right]^2}{\int\limits_{-\infty}^{\infty}\int\limits_{-\infty}^{\infty}|F(x,y)|^4 \mathrm{d}x\mathrm{d}y}. \tag{2.3}$$

A large MFD is essential for high-peak-power operation. Today, the largest possible MFD of a step-index fiber still supporting single-mode operation is approximately 15 µm (at 1030 nm) [41]. This is due to the achievable production tolerance of the required small refractive index difference between the core and the cladding. However, with more sophisticate fiber designs, such as the photonic-crystal fiber (PCF) [46] as depicted in Fig. 2.1c, larger MFDs are still possible. Here the bulk material surrounding the doped core is microstructured with several air holes of wavelength or sub-wavelength scale, effectively reducing the refractive index of this region of the fiber. With this technology MFDs up to 50 µm [47] are feasible.

There are also fibers with even larger MFDs employing a different guiding mechanism. These exhibit a higher-order-mode content, since also cladding modes guided by a second air cladding exist. Here the overlap of the different modes with the doped region has to be taken into account. Since the fundamental mode has the largest overlap, it will undergo the highest gain and higher-order modes are suppressed during amplification, which is referred to as effectively single-mode operation. If additionally the size and the pitch of the air holes are increased, higher-order modes will be delocalized from the core, allowing for a preferential gain of the fundamental mode. The first representatives of these fiber designs were the large-pitch fibers (LPFs) [41], shown in Fig. 2.1d, and allow for MFDs > 50 µm. For the high-power experiments within this work LPFs with MFDs of up to ∼ 80 µm have been employed.

2.2. Amplification of Ultrashort Pulses

In this section, a theoretical model describing ultrashort pulses and their amplification in optical fibers is presented, which will be used both to investigate the dynamics occurring during pulse amplification and to quantitatively underpin the experiments in the following

chapters. In particular, the physics of gain and energy extraction are discussed, while gain saturation will play an important role for temporally separated amplification. In this regard, dispersion and nonlinear effects will be presented and discussed in Sec. 2.4, since they impact the pulse propagation through the fiber. Moreover, it will be shown that these effects can affect the efficiency of the pulse-combination process, as it will be considered later on in Chap. 3.

2.2.1. Definition of Ultrashort Pulses

Light is an electromagnetic wave as described by Maxwell's equations[3]. Generally, a pulsed light beam (i.e. a wave packet of finite transverse and temporal width) is polychromatic and can be considered as a superposition of stationary plane monochromatic waves with different propagation directions and frequencies. Thus, the electric field is [48]

$$\mathcal{E}(\mathbf{r}, t) = \frac{1}{2} \Re \left(\int\limits_{-\infty}^{\infty} \int\limits_{-\infty}^{\infty} \tilde{\mathbf{E}}(\mathbf{k}, \omega) \exp\left\{ i \left[\mathbf{k}(\omega)\mathbf{r} - \omega t \right] \right\} \mathrm{d}\mathbf{k}\mathrm{d}\omega \right), \qquad (2.4)$$

with ω being the angular frequency, t the time, $\mathbf{r}$ the position in three-dimensional space[4], $\mathbf{k}$ the wave vector[5], and $\tilde{\mathbf{E}}(\mathbf{k}, \omega)$ the spatial and spectral components of the field vector. In the following it is assumed that the electric field oscillates only along the x-direction. Moreover, the pulse propagates along the z-direction and the transverse beam profile $F(x, y)$ is assumed to be constant over the pulse. Since for pulse durations $> 100\,\mathrm{fs}$ (at a central wavelength of $1\,\mu\mathrm{m}$) the spectral bandwidth $\Delta\omega$ is much narrower than the central frequency of the light ω_0 (where ω_0 is the carrier angular frequency), the pulse is said to be quasi-monochromatic [26, 48]. Separating the fast-oscillating carrier from the slower-varying amplitude, Eq. (2.4) can be approximated to [48]

$$\mathcal{E}(\mathbf{r}, t) \approx \frac{1}{2} F(x, y) \Re \left(\exp(-i\omega_0 t) \int\limits_{\omega_0 - \frac{\Delta\omega}{2}}^{\omega_0 + \frac{\Delta\omega}{2}} \tilde{E}(\omega) \exp\left\{ i \left[k(\omega)z - (\omega - \omega_0)t) \right] \right\} \mathrm{d}\omega \right) \hat{\mathbf{x}}, \quad (2.5)$$

with $k = k_\mathrm{z}$ denoting the wave number[6] and $\hat{\mathbf{x}}$ being the unit vector in x-direction. This is also known as slowly-varying-envelope approximation, since the pulse envelope varies

---

[3]Within the scope of this work all media are considered as non-magnetizable and in absence of free charges.

[4]Bold typefaces represent vectors.

[5]$\mathbf{k} = k_\mathrm{x}\hat{\mathbf{x}} + k_\mathrm{y}\hat{\mathbf{y}} + k_\mathrm{z}\hat{\mathbf{z}}$, where $\hat{\mathbf{x}}$, $\hat{\mathbf{y}}$ and $\hat{\mathbf{z}}$ are the unit vectors in x-, y- and z-direction.

[6]$|\mathbf{k}| = k = \sqrt{k_\mathrm{x}^2 + k_\mathrm{y}^2 + k_\mathrm{z}^2}$, where $k_\mathrm{x} = k_\mathrm{y} = 0$.

slowly compared to the carrier. Developing the wave number at the carrier frequency in a Taylor series results in

$$k(\omega) \approx k(\omega_0) + \sum_{m=1}^{M} \frac{\mathrm{d}^m k(\omega)}{m!\,\mathrm{d}\omega^m}\bigg|_{\omega=\omega_0} (\omega - \omega_0)^m = \sum_{m=0}^{M} \frac{\beta_m}{m!}\bigg|_{\omega=\omega_0} (\omega - \omega_0)^m, \qquad (2.6)$$

with β_m defining the expansion coefficients that correspond to mth-order dispersion terms [26] (see Subsec. 2.4.1). The phase velocity of the fast carrier is given by $v_{\mathrm{ph}} = \omega_0 \beta_0^{-1}$ and the group velocity of the slow envelope is given by $v_{\mathrm{g}} = \beta_1^{-1}$. Finally, introducing the complex pulse envelope $A(z,t)$, Eq. (2.5) can be expressed as

$$\mathcal{E}(\mathbf{r},t) = \frac{1}{2}F(x,y)\Re\left\{A(z,t)\exp\left[i(\beta_0 z - \omega_0 t)\right]\right\}\hat{\mathbf{x}}. \qquad (2.7)$$

Please note that commonly $A(z,t)$ is normalized such that $|A(z,t)|^2$ results in the optical power[7].

The periodicity at which pulses are emitted, for example by a mode-locked oscillator, is called repetition rate $f_{\mathrm{rep}} = T_{\mathrm{rep}}^{-1}$, where T_{rep} is the pulse repetition time, with a corresponding average power $\bar{P}$. Moreover, for particular applications, there are other characteristics of the pulse which are important. One of them is the pulse energy

$$E = \int_{-T_{\mathrm{rep}}/2}^{T_{\mathrm{rep}}/2} |A(z,t)|^2 \mathrm{d}t = \frac{\bar{P}}{f_{\mathrm{rep}}}, \qquad (2.8)$$

which summarizes the energy content of a pulse at position z. The full width at half maximum (FWHM) is used throughout this thesis, to define the temporal duration of a pulse. The shortest achievable pulse duration T_0 is given by the available spectral bandwidth, which is related to T_0 via the time-bandwidth product [49]. Typically, for $T_0 \lesssim 1\,\mathrm{ps}$ a pulse is said to be ultrashort. Commonly, a Gaussian pulse envelope

$$A(0,t) = \sqrt{P_{\mathrm{peak}}}\exp\left[-2\ln(2)\frac{t^2}{T_0^2}\right], \qquad (2.9)$$

is assumed[8], where P_{peak} is the peak power. This definition is applied as an initial ansatz for numeric simulations within this work.

The spatial laser beam profile depends on the properties of the surrounding medium.

---

[7] $A(z,t)$ is defined such that $|A(z,t)|^2 \equiv \frac{1}{2}\epsilon_0 c n |A'(z,t)|^2 \int\int_{-\infty}^{\infty} |F(x,y)|^2 \mathrm{d}x\mathrm{d}y$, so that $[|A(z,t)|^2]_{\mathrm{SI}} = \mathrm{W}$ and $[A'(z,t)]_{\mathrm{SI}} = \mathrm{Vm}^{-1}$; c is the vacuum speed of light and n is the refractive index of the medium [26].
[8] The term $2\ln(2)$ is used so that T_0 becomes the FWHM of the pulse power.

While in free-space it can be almost arbitrary, in optical fibers it depends on the waveguide geometry. Typically, a Gaussian beam profile with a flat spatial phase is sought after, since it provides the smallest focus and, thus, the highest light intensity, which is crucial for many applications. This makes fibers an attractive active media, since their fundamental mode (in a step-inex fiber) can, in most cases, be approximated by [26]

$$F(x,y) \approx \exp\left(-\frac{x^2 + y^2}{w_0^2}\right),\tag{2.10}$$

with w_0 being the beam radius[9] (at $z = 0\,\mathrm{m}$), as depicted in Fig. 2.2 (left). Using Eqs. (2.2), (2.3) and (2.10), then $A_{\mathrm{mod}} \approx A_{\mathrm{eff}} = \pi w_0^2$ and MFD $= 2w_0$.

For large beam diameters and short propagation distances $F(x,y)$ can be assumed to be constant. However, for large propagation distances the spatial Gaussian beam evolution has to be taken into account. Assuming Eq. (2.10) as the initial beam profile, at position z it has changed to [49]

$$F(x,y,z) = \frac{1}{q(z)} \exp\left(-ik\frac{x^2 + y^2}{2q(z)}\right),\tag{2.11}$$

with the complex beam parameter [49]

$$\frac{1}{q(z)} = \frac{1}{R(z)} - i\frac{\lambda}{\pi w^2(z)}.\tag{2.12}$$

Thereby, the wavelength is λ, the radius of curvature at z is $R(z) = z[1 + (z_{\mathrm{R}}/z)^2]$, the beam radius at z is $w(z) = w_0\sqrt{1 + (z/z_{\mathrm{R}})^2}$ and the Rayleigh length is $z_{\mathrm{R}} = \pi w_0^2/(M^2\lambda)$
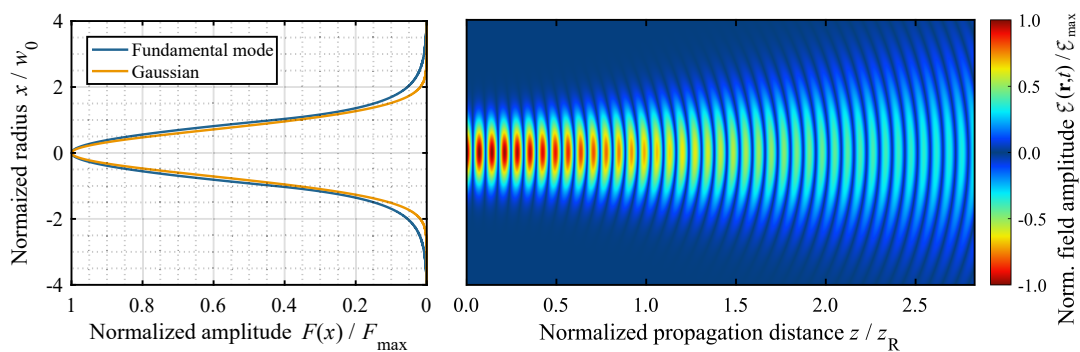

Figure 2.2.: Quality of the Gaussian approximation to the fundamental fiber mode of a step-index fiber (LP$_{01}$ at $V = 2.4$, compare to Sec. 2.1) on the left. Illustration of the real field amplitude evolution of the Gaussian beam on the right.

---

[9]The beam radius is defined as the distance from the beam axis at which $F(x,y)$ is reduced to $1/e$.

with the beam quality factor M^2 [50]. The evolution of the real field amplitude of a Gaussian beam is illustrated in Fig. 2.2 (right). The spatial beam properties will be important for the efficiency of the free-space beam-combination process, as will be considered in Chap. 3. In the following, a model describing the amplification of pulses is introduced.

2.2.2. One-Dimensional Rate Equations

The amplification of a signal in an active medium can be numerically modeled by solving the rate equations [51–53]. These are coupled differential equations that can be formulated for a certain number of signals being present in the amplifier. In this section, a one-dimensional approach is considered, assuming that the signals are propagating in the $\pm z$-direction without any transverse dependence. Furthermore, amplified spontaneous emission (ASE) will be neglected[10]. Indicating the signals to be amplified (s) and the pump signals (p) with j, the evolution of the local population density of the upper laser level[11] $N_2(z,t)$ and of the signal powers $P_j(z,t)$ at position z and time t are

$$\frac{\partial N_2(z,t)}{\partial t} = \sum_j \frac{\sigma(\omega_j)}{\hbar\omega_j} \frac{P_j(z,t)\Gamma_j}{A_{\text{dop}}} \left[N_{2,\text{tr}}(\omega_j) - N_2(z,t) \right] - \frac{N_2(z,t)}{\tau_2}, \quad (2.13)$$

$$\pm \left[\frac{\partial}{\partial z} + \beta_{1,j}\frac{\partial}{\partial t} \right] P_j(z,t) = \left\{ \sigma(\omega_j)\left[N_2(z,t) - N_{2,\text{tr}}(\omega_j) \right] - \alpha(\omega_j) \right\} P_j(z,t)\Gamma_j, \quad (2.14)$$

with the photon energy[12] $\hbar\omega_j$, the upper state lifetime τ_2, the loss factor $\alpha(\omega_j)$ and the overlap factor $\Gamma_j = \Gamma_{\text{s/p}}$ according to Eq. (2.1) (assumed to be z-independent). In terms of fibers, each signal $P_j(z,t)$ can be interpreted as a sum of fiber modes [44]. The effective absorption cross-sections $\sigma_{\text{abs}}(\omega_j)$ and the effective emission cross-sections $\sigma_{\text{em}}(\omega_j)$ (as depicted in Fig. 2.1a for Yb-doped germanosilicate glass) are grouped into $\sigma(\omega_j) = \sigma_{\text{abs}}(\omega_j) + \sigma_{\text{em}}(\omega_j)$. Then, the transparency inversion density is given by

$$N_{2,\text{tr}}(\omega_j) = N_{\text{tot}}\frac{\sigma_{\text{abs}}(\omega_j)}{\sigma(\omega_j)}, \quad (2.15)$$

with the total active-ion concentration N_{tot} being the sum of the population densities of the upper and the lower laser level.

---

[10]ASE can be added, e.g. by introducing several frequency channels [51].
[11]Note that N_2 is considered locally in one-dimensional direction as an average integrated over the transverse direction.
[12]$\hbar$ denotes the reduced Planck constant $\dfrac{h}{2\pi}$.

Inversion Build-Up

A steady-state case is considered to obtain an expression for the evolution of the population density of the upper laser level during the pump process. Since the time scale on which the signal pulse is present in the amplifier is much shorter than the time between consecutive pulses ($T_0 \ll 1/f_{\mathrm{rep}}$), the effect of the pump during the signal transit time will be neglected. Assuming a constant pump power $\bar{P}_{\mathrm{p}}$ at angular frequency ω_{p}, the inversion build-up time is [49]

$$\tau_{\mathrm{inv}} = \frac{\tau_2}{1 + \dfrac{\bar{P}_{\mathrm{p}}}{P_{\mathrm{p,sat}}}}, \tag{2.16}$$

with the saturation power of the pump $P_{\mathrm{p,sat}}$ being

$$P_{\mathrm{p,sat}} = \frac{\hbar\omega_{\mathrm{p}}}{\sigma(\omega_{\mathrm{p}})} \frac{A_{\mathrm{dop}}}{\Gamma_{\mathrm{p}}\tau_2}. \tag{2.17}$$

With this, the temporal evolution of the population density N_2 is

$$N_2(t) = N_{2,\mathrm{max}} + (N_{2,0} - N_{2,\mathrm{max}}) \exp\left(-\frac{t}{\tau_{\mathrm{inv}}}\right), \tag{2.18}$$

with $N_{2,0}$ being the initial population level and $N_{2,\mathrm{max}}$ being the maximum population density for a given pump $\bar{P}_{\mathrm{p}}$, which is

$$N_{2,\mathrm{max}} = N_{2,\mathrm{tr}}(\omega_{\mathrm{p}}) \frac{\dfrac{\bar{P}_{\mathrm{p}}}{P_{\mathrm{p,sat}}}}{1 + \dfrac{\bar{P}_{\mathrm{p}}}{P_{\mathrm{p,sat}}}}. \tag{2.19}$$

The maximum reachable inversion depends on the pump photon energy. For $\bar{P}_{\mathrm{p}} \gg P_{\mathrm{p,sat}}$, regarding Eqs. (2.15) and (2.19) and using the cross-sections from Fig. 2.1a, it results in $N_{2,\mathrm{max}} \approx 0.5 N_{\mathrm{tot}}$ if pumped at 976 nm wavelength and $N_{2,\mathrm{max}} > 0.95 N_{\mathrm{tot}}$ when pumping around 915 nm. But the increased quantum defect may lead to an increased thermal load in the fiber, which can enforce mode instabilities [25].

2.2.3. Pulse Dynamics using the Frantz-Nodvik Model

Transient gain dynamics have to be taken into account for the amplification of pulses. If the effects that occur during the amplification are fast compared to the inversion build-up time and upper state lifetime, i.e. the pulse duration $T_0 \ll \tau_{\mathrm{inv}} \ll \tau_2$, then Eqs. (2.13)

and (2.14) will be simplified to[13]

$$\frac{\partial \Delta N(z,t)}{\partial t} = -\frac{\sigma(\omega_0)}{\hbar \omega_0} \frac{P(z,t) \Gamma_s}{A_{dop}} \Delta N(z,t), \tag{2.20}$$

$$\pm \left[\frac{\partial}{\partial z} + \beta_1 \frac{\partial}{\partial t} \right] P(z,t) = \sigma(\omega_0) P(z,t) \Gamma_s \Delta N(z,t), \tag{2.21}$$

restricting to a single pulse with the power $P_s(z,t) = P(z,t)$, central angular frequency $\omega_s = \omega_0$ and group velocity $\beta_{1,s}^{-1} = \beta_1^{-1}$ being present in the amplifier. Moreover, the abbreviation $\Delta N(z,t) = N_2(z,t) - N_{2,tr}(\omega_0)$ is introduced. An analytic solution of these equations was found by Frantz and Nodvik [55] and is[14]

$$P(z,t) = \frac{P_0(t - \beta_1 z)}{1 - \left[1 - G_0^{-1}(z) \right] \exp \left(-E_{sat}^{-1} \int_{-\infty}^{t - \beta_1 z} P_0(t') \mathrm{d}t' \right)}, \tag{2.22}$$

$$\Delta N(z,t) = \frac{\Delta N_0(z)}{1 + G_0(z) \left[\exp \left(E_{sat}^{-1} \int_{-\infty}^{t - \beta_1 z} P_0(t') \mathrm{d}t' \right) - 1 \right]}. \tag{2.23}$$

These so-called Frantz-Nodvik equations provide the evolution of any arbitrary pulse shape $P_0(t)$ and any build-up inversion distribution $\Delta N_0(z)$ at each position z and time t along the amplifier. Important parameters are the saturation energy

$$E_{sat} = \frac{\hbar \omega_0}{\sigma(\omega_0)} \frac{A_{dop}}{\Gamma_s}, \tag{2.24}$$

and the small-signal gain

$$G_0(z) = \exp \left(\sigma(\omega_0) \Gamma_s \int_0^z \Delta N_0(z') \mathrm{d}z' \right). \tag{2.25}$$

The maximum gain is given by the small-signal gain and, hence, by a fixed number of active ions being available. Therefore, this gain cannot be maintained for arbitrarily high signal energy due to energy conservation. Thus, for increasing signal energy the gain is reduced, which is referred to as saturation. As a pulse propagates through an amplifier its

---

[13]Furthermore, an instantaneous response of the material polarization $\mathbf{P}(\mathbf{r},t)$ (see Subsec. 2.4.2) is assumed [54].

[14]Basically, Eqs. (2.22) and (2.23) are valid for four-level and inverse three-level systems of the amplifying medium, which is related to a pump wavelength of 915 nm and 976 nm, respectively, assuming a 1030 nm signal. In the case of a three-level system a factor of two within the exponential terms has to be considered [49, 55]. Furthermore, Eqs. (2.22) and (2.23) are general expressions. As periodic signals are considered (see Subsec. 2.2.1), the integration limits are restricted to $\pm T_{rep}/2$.

leading edge experiences an unadulterated inversion, whereas its trailing edge experiences the residual inversion that has not been depleted by the leading edge. This results in a decreasing gain factor over the pulse envelope and in a deformation of its shape. But the amount of pulse deformation is given by the total inversion level in the fiber and not by a particular inversion distribution. Furthermore, from Eq. (2.23) it can be seen that the inversion distribution after a pulse was propagating through the amplifier, is determined by the total input pulse energy, not by a particular pulse shape [56]. In Fig. 2.3a the normalized shapes of the amplified pulses according to Eq. (2.22) are depicted as an illustration of the pulse deformation. A Gaussian pulse shape, according to Eq. (2.9), at different fractions of E_{sat} and $G_0(L) = 30\mathrm{dB}$ are assumed. The corresponding normalized final inversion across the amplifier, according to Eq. (2.23), is depicted in Fig. 2.3b. It can be seen that the closer the energy of the initial pulse gets to the saturation energy of the amplifier, the stronger the inversion is depleted and the more the pulse is deformed. In order to compensate for this effect, the initial pulse can be pre-shaped [56].
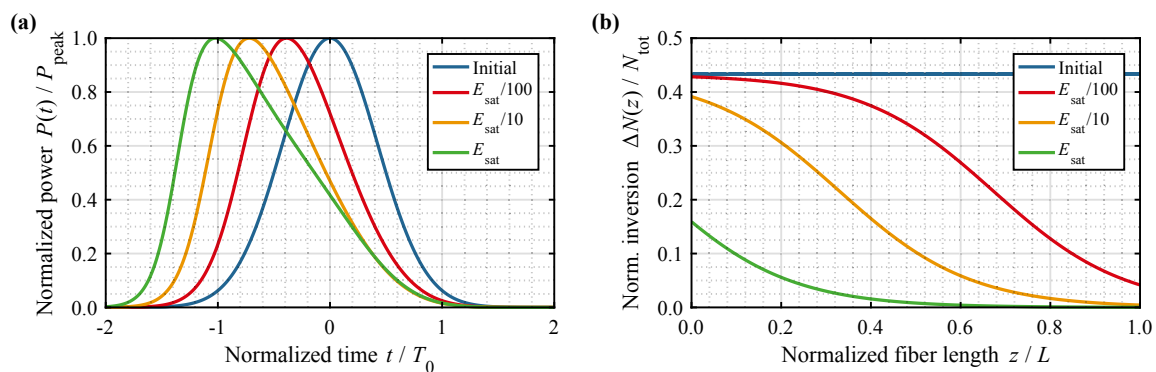

Figure 2.3.: (a) Pulse-shape deformation due to saturation of the amplifier for an initial Gaussian pulse with seed pulse energies at different fractions of E_{sat} (depicted normalized to the respective peak powers P_{peak} and to the pulse duration T_0) and (b) the corresponding final inversion distribution along the fiber (normalized to the total ion concentration N_{tot} and to the length L). A small-signal gain of $G_0 = 30\mathrm{dB}$ is assumed.

2.2.4. Energy and Efficiency Considerations

As mentioned in Subsec. 2.2.3, the relation between the input and the output energy of an amplifier does not depend on the dynamics of the amplification process. Thus, the pulse energy at a particular position z within the amplifier is obtained by the temporal

integration of Eq. (2.22) and results in [55]

$$E(z) = E_{\text{sat}} \ln \left\{ 1 + G_0(z) \left[\exp \left(\frac{E_0}{E_{\text{sat}}} \right) - 1 \right] \right\},\tag{2.26}$$

where E_0 is the initial pulse energy. Hence, the energy gain is

$$G(z) = \frac{E(z)}{E_0},\tag{2.27}$$

which can either be calculated for the whole amplifier length with $z = L$ or at each position z (step-wise) for numerical simulations. The outcomes of Eq. (2.26) and Eq. (2.27) for different $G_0(L)$ and E_0/E_{sat} ratio are depicted in Fig. 2.4a and Fig. 2.4b, respectively. Achieving a desired amplified pulse energy requires either a small initial pulse energy and a high small-signal gain or a higher initial pulse energy and a lower small-signal gain. There are two extreme operation regimes of an amplifier that can be emphasized. In the small-signal regime, a low energy of the initial pulse does not affect the inversion and the energy growth is exponential, such that $G(z) \approx G_0(z)$. In the saturated regime, the inversion gets strongly depleted (compare to Fig. 2.3b) and the energy growth becomes slower, such that $G(z) \approx 1 + \ln \left[G_0(z) \right] E_{\text{sat}}/E_0$ [27].

A measure for the overall energy content stored in an amplifier is the stored energy. It is determined both by the pump frequency and power and by the active volume of the amplifier. However, due to the quantum defect, the energy that can be extracted by a pulse at the signal frequency with a certain energy and spatial overlap with the doped area is always less than the stored energy. For an infinitely high initial pulse energy, the
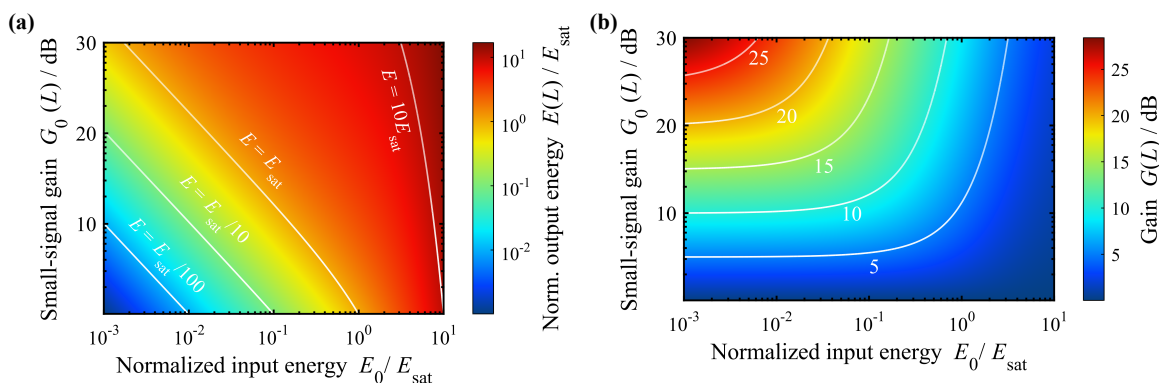

Figure 2.4.: (a) Amplified pulse energy $E(L)$ and (b) energy gain $G(L)$ as a function of the small-signal gain $G_0(L)$ and the input pulse energy E_0 normalized to the saturation energy E_{sat} (after [56]).

extractable energy approaches its maximum, which is [49]

$$E_{\mathrm{extr}}^{\mathrm{max}} = \hbar\omega_0 A_{\mathrm{dop}} \int_0^L \Delta N_0(z)\mathrm{d}z = E_{\mathrm{sat}} \ln\left[G_0(L)\right], \qquad (2.28)$$

using Eqs. (2.24) and (2.25). This extractable energy, as can be seen in Eq. (2.28), is determined by the small-signal gain. In Fig. 2.5a $E_{\mathrm{extr}}^{\mathrm{max}}$ is depicted as a function of the doped-core diameter (for a fiber length of 1 m) at a signal wavelength of 1030 nm and for both a pump wavelength of 915 nm and 976 nm, respectively. The maximum extractable energy if pumped at 915 nm will be about twice as large as that obtained by pumping at 976 nm.

The ratio between the actual extracted energy E_{extr} and the maximum extractable energy $E_{\mathrm{extr}}^{\mathrm{max}}$ is represented by the extraction efficiency [49]

$$\eta_{\mathrm{extr}} = \frac{E_{\mathrm{extr}}}{E_{\mathrm{extr}}^{\mathrm{max}}} = \frac{E(L) - E_0}{E_{\mathrm{sat}} \ln\left[G_0(L)\right]}. \qquad (2.29)$$

In Fig. 2.5b the extraction efficiency is depicted for the same parameters used in Fig. 2.4b. A direct comparison demonstrates that there has to be a trade-off in either obtaining maximum gain or maximum extraction efficiency. This is the reason for the so-called master-oscillator power-amplifier (MOPA) architectures. In these, low-energy pulses delivered by an oscillator are amplified in several stages. The first amplification stages operate at high gain and provide sufficient energy for efficient energy extraction in the
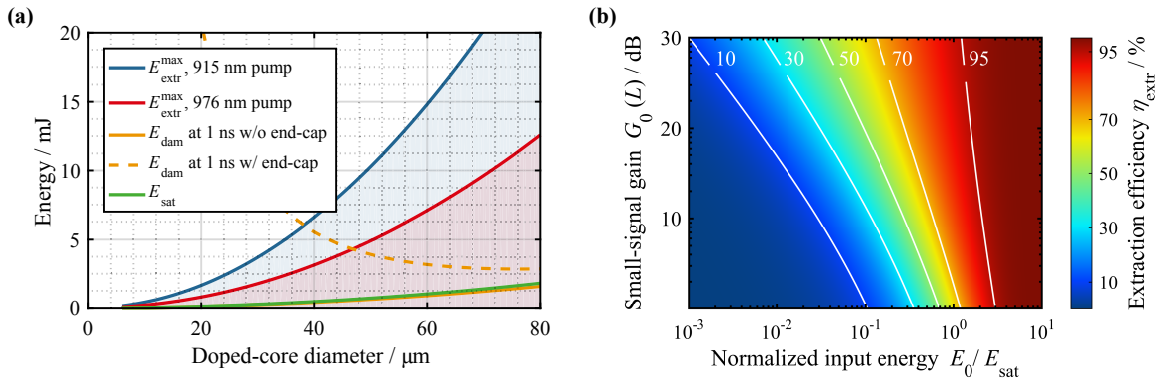

Figure 2.5.: (a) Maximum extractable energy $E_{\mathrm{extr}}^{\mathrm{max}}$ as a function of the doped-core diameter for the pump wavelengths 915 nm and 976 nm assuming a fiber length of $L = 1$ m and a signal wavelength of 1030 nm ($N_{\mathrm{tot}} = 3 \cdot 10^{25}\,\mathrm{m}^{-3}$ [57]). Additionally, the saturation energy E_{sat} and the energy damage threshold E_{dam} with and without end-caps ($d = 5$ mm, $M^2 = 1.1$) and assuming a pulse duration of $T_0 = 1$ ns are shown (note that for these a constant $\Gamma_{\mathrm{s}} = 0.8$ is assumed). (b) Extraction efficiency η_{extr} as a function of the small-signal gain $G_0(L)$ and the input energy E_0 normalized to the saturation energy E_{sat} (after [56]).

final amplifier.

Irrespective of higher order effects, it is not straightforward to extract arbitrarily high energy from an amplifier with an arbitrary pulse. Typically, for sufficiently high energy surface damage occurs due to a breakdown caused by a field intensification at imperfections on the surface. Within the bulk material fracture occurs either due to local heat deposition (for pulse durations $T_0 > 100\,\mathrm{ps}$) or, ultimately, due to electron avalanche breakdown caused by multi-photon ionization (for $T_0 < 20\,\mathrm{ps}$) [27]. However, for silica glass at an operation wavelength around $1\,\mathrm{\mu m}$ and pulse durations of $T_0 > 20\,\mathrm{ps}$ the empiric formula [27, 53]

$$E_{\mathrm{dam}} \approx \left[1 + \left(\frac{d\lambda M^2}{A_{\mathrm{eff}}} \right)^2 \right] A_{\mathrm{eff}} T_0^{0.4} \cdot 10^9 \, \frac{\mathrm{J}}{\mathrm{m}^2 \mathrm{s}^{0.4}} \tag{2.30}$$

provides a reasonably good estimation for this optically-induced damage that compares well with the experimental observations in fiber-based chirped-pulse-amplification systems (see Subsec. 2.4.1). The term within the brackets describes the impact of fused silica end-caps with thickness d that can be spliced to the fiber-end facet. Within these the beam expands, which increases the damage threshold. For example, assuming a fiber with MFD $= 80\,\mathrm{\mu m}$, $d = 5\,\mathrm{mm}$ and $T_0 = 1\,\mathrm{ns}$ ($\lambda = 1030\,\mathrm{nm}$, $M^2 = 1.1$), the use of end-caps results in an improvement of E_{dam} by a factor of ~ 3. In Fig. 2.5a both the damage energy threshold assuming a pulse duration of $1\,\mathrm{ns}$ (which is appropriate for stretched pulses and a moderate stretcher/compressor size) and the saturation energy, according to Eq. (2.24), are depicted. For this pulse duration E_{dam} is in the order of E_{sat} making it difficult to extract much of the available energy. With end-caps it can be increased above E_{sat}, as additionally shown in Fig. 2.5a. However, there is even more energy available from the fiber, but damage still limits the energy extraction. In order to make this energy accessible, the energy of a pulse can be distributed on several pulses. This constitutes the basic concept of divided-pulse amplification, which will be introduced in Chap. 3.

2.3. Polarization of Light

In the scope of this work, the division of beams or pulses using their polarization is considered. Therefore, the description of polarization as a property of light will be explained in the following. Moreover, the phenomenon of birefringence is described in Subsec. 2.3.2, which can be used to alter the state of polarization of the light. Therefore, a calculus describing this manipulation is introduced in Subsec. 2.3.3.

2.3.1. Description of Polarization

In Subsec. 2.2.1 the electric field vector was restricted to only one transverse component. This can be generalized, since the polarization of the field is a property in three-dimensional space[15]. Polarization describes the trajectory described by the electric field vector tip with time. For paraxial fields propagating along z only the field components lying on the transverse x-y-plane are of concern. Following Eq. (2.7) this can be expressed as [58]

$$\mathcal{E}(\mathbf{r}, t) = \frac{1}{2} F(x, y) \Re \left\{ [A_\mathrm{x}(z, t)\hat{\mathbf{x}} + A_\mathrm{y}(z, t)\hat{\mathbf{y}}] \exp\left[i(\beta_0 z - \omega_0 t)\right] \right\}, \qquad (2.31)$$

with $\hat{\mathbf{x}}$ and $\hat{\mathbf{y}}$ being the unit vectors orienting the field in x- and y-direction and the complex envelope amplitudes being

$$\left.\begin{aligned}
A_\mathrm{x}(z, t) &= |A_\mathrm{x}(z, t)| \exp\left[i\phi_\mathrm{x}(z, t)\right], \\
A_\mathrm{y}(z, t) &= |A_\mathrm{y}(z, t)| \exp\left[i\phi_\mathrm{y}(z, t)\right].
\end{aligned}\right\} \qquad (2.32)$$

The relation between the individual field vector components determines a specific state of polarization. Hence, the polarization state is defined by two orthogonal oscillating amplitudes and their relative phase $\Delta\phi = \phi_\mathrm{y} - \phi_\mathrm{x}$, which can by visualized in the x-y-projection plane. The field is linearly polarized for $\Delta\phi = m\pi$ with $m \in \mathbb{Z}$ or for one of both amplitudes vanishing (e.g. $A_\mathrm{x} = 0$). Circular polarization is obtained for $|A_\mathrm{x}| = |A_\mathrm{y}|$ and a phase difference of multiples of $\pi/2$. It can be distinguished between right-handed circularly polarized for $\Delta\phi = \pi/2 + 2m\pi$ with $m \in \mathbb{Z}$ and left-handed circularly polarized for $\Delta\phi = 3/2\pi + 2m\pi$. For any other arbitrary amplitude and phase relation the field is elliptically polarized. Figure 2.6 summarizes these possible states for $|A_\mathrm{x}| = |A_\mathrm{y}|$ [48].

Within a set coordinate system, there is a notation regarding the interaction of the electric field in the vicinity of a surface. The polarization components lying in the plane of incidence and those perpendicular to that are called p and s [58], respectively[16]. Throughout this thesis the x- and the y-component will be referred to as the p-polarized and s-polarized component, respectively.

2.3.2. Birefringence

The state of polarization of a polarized beam propagating through a linear anisotropic dielectric medium can change depending on the propagation direction and the initial state of polarization, which is referred to as birefringence. Such materials possess different op-

---

[15]In general the complex electric field vector is $\mathbf{E}(\mathbf{r}, t) = E_\mathrm{x}(\mathbf{r}, t)\hat{\mathbf{x}} + E_\mathrm{y}(\mathbf{r}, t)\hat{\mathbf{y}} + E_\mathrm{z}(\mathbf{r}, t)\hat{\mathbf{z}}$.
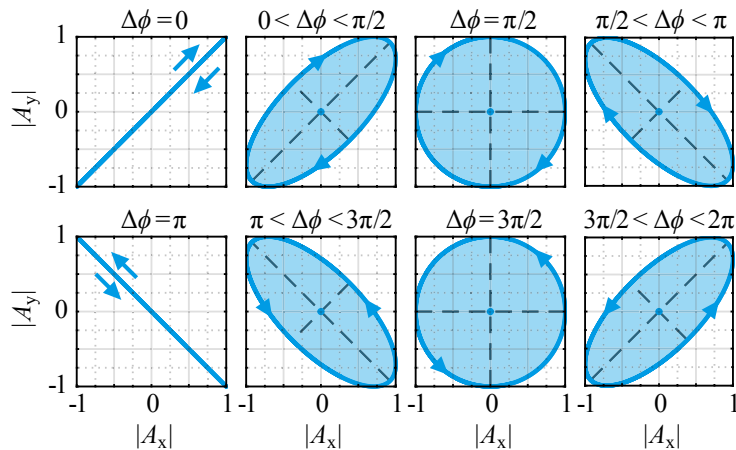[16]Inherited from the German notation *parallel* and *senkrecht* [58].

Figure 2.6.: Right- (top row) and left-handed (bottom row) elliptical polarization states at different relative phases $\Delta\phi$ and equal amplitudes $|A_\text{x}| = |A_\text{y}| = 1$ (after [48]).

tical properties on distinct axes in space stemming from the different polarizability of the molecules which are organized in periodic regular patterns, as for example in crystals [58]. Uniaxial crystals have one axis of symmetry, along which the properties are isotropic, which is called the optical axis. The polarization component of the electric field propagating perpendicular to it will experience a refractive index $n = n_\text{o}$ (ordinary index). On the other hand, the polarization component parallel to the optical axis will experience a refractive index n_e (extraordinary index). For $n_\text{e} > n_\text{o}$ the crystal is positive and for $n_\text{e} < n_\text{o}$ negative uniaxial birefringent [58]. In general, the index change with propagation direction can be expressed by an optical indicatrix or mathematically by a tensor of the dielectric permittivity [59].

Uniaxial crystals can be applied to deliberately manipulate the state of polarization of a beam. The maximum imposed phase difference between both polarization components, propagating parallel (phase φ_e) and orthogonally (phase φ_o) to the optical axis, is

$$\Delta\varphi = \varphi_\text{e} - \varphi_\text{o} = \frac{2\pi}{\lambda}d(n_\text{e} - n_\text{o}) = \frac{2\pi}{\lambda}d\Delta n, \tag{2.33}$$

where λ is the wavelength of the incident field and d is the thickness of the crystal. For the special cases of $\Delta\varphi = \pi$ and $\Delta\varphi = \pi/2$ a half-wave plate (HWP, $d\Delta n = \lambda/2$) and a quarter-wave plate (QWP, $d\Delta n = \lambda/4$) are obtained, respectively, which can be used, for example, to alternate between the states depicted in Fig. 2.6. While a QWP can be applied to change from linear to elliptic or circular polarization and vice-versa, an HWP can be used to rotate the orientation of the linear polarization state.

2.3.3. Jones Calculus

The state of polarization of a given electric field vector can be manipulated by optical elements, such as wave plates or polarizers. To evaluate this effect the so-called Jones calculus can be applied. As indicated by Eq. (2.32), the field is characterized by its complex envelopes A_x and A_y at any time t. These can now be expressed as a Jones vector [58, 60]

$$\mathbf{J} = \begin{bmatrix} A_x \\ A_y \end{bmatrix}. \tag{2.34}$$

The effect of an optical element on the different field components can be represented by a two-by-two matrix, assuming the element to be linear. Hence, with the input and the output vectors being defined by $\mathbf{J}_1$ and $\mathbf{J}_2$, respectively, the matrix notation

$$\mathbf{J}_2 = \mathcal{M}\mathbf{J}_1 \tag{2.35}$$

can be applied, with $\mathcal{M}$ denoting the Jones matrix describing the optical element. For a system containing n elements it follows:

$$\mathcal{M} = \mathcal{M}_n \mathcal{M}_{n-1} \cdots \mathcal{M}_2 \mathcal{M}_1. \tag{2.36}$$

Jones matrices for polarizing beam splitters (PBS), HWPs and QWPs are summarized in Tab. 2.1. Therefore, the parameters R_s, T_p and θ are introduced, denoting the power

Table 2.1.: Jones matrices for a linear polarizer and a wave plate [58, 60]. Please note that the constant phase factor in case of wave plates is omitted (for more information on these Jones matrices compare to Appendix A).

Optical element	Jones matrix
Linear polarizer (PBS)	ideal transmission $\qquad$ non-idealized transmission $$\mathcal{M}_T = \begin{bmatrix} 1 & 0 \\ 0 & 0 \end{bmatrix} \qquad \mathcal{M}_T(T_p, R_s) = \begin{bmatrix} \sqrt{T_p} & 0 \\ 0 & \sqrt{1-R_s} \end{bmatrix}$$ ideal reflection $\qquad$ non-idealized reflection $$\mathcal{M}_R = (i)\begin{bmatrix} 0 & 0 \\ 0 & 1 \end{bmatrix} \qquad \mathcal{M}_R(T_p, R_s) = (i)\begin{bmatrix} \sqrt{1-T_p} & 0 \\ 0 & \sqrt{R_s} \end{bmatrix}$$
Wave plate	HWP $(\Delta\varphi = \pi)$ $\qquad$ rotated HWP $$\mathcal{M}_{HWP} = \begin{bmatrix} 1 & 0 \\ 0 & -1 \end{bmatrix} \quad \mathcal{M}_{HWP}(\theta) = \begin{bmatrix} \cos(2\theta) & \sin(2\theta) \\ \sin(2\theta) & -\cos(2\theta) \end{bmatrix}$$ QWP $(\Delta\varphi = \pi/2)$ $\qquad$ rotated QWP $$\mathcal{M}_{QWP} = \begin{bmatrix} 1 & 0 \\ 0 & -i \end{bmatrix} \quad \mathcal{M}_{QWP}(\theta) = \begin{bmatrix} \cos^2(\theta) - i\sin^2(\theta) & (1+i)\sin(\theta)\cos(\theta) \\ (1+i)\sin(\theta)\cos(\theta) & \sin^2(\theta) - i\cos^2(\theta) \end{bmatrix}$$

reflectance of the *s*-polarization component, the power transmittance of the *p*-polarization component and the orientation angle between the optical axis and the *p*-polarization axis, respectively.

2.4. Propagation of Ultrashort Pulses in Nonlinear and Dispersive Media

The propagation of ultrashort pulses through optical fibers can change their temporal and spectral properties. Therefore, the impact of dispersion is discussed in Subsec. 2.4.1. Furthermore, the signal confinement in small cores can lead to high intensities upon amplification that, due to the long interaction lengths with the material, can give rise to nonlinear effects. The most important nonlinear effects for this work are considered in Subsec. 2.4.2.

2.4.1. Dispersion

Upon the propagation of a pulse through an optical fiber it can happen that its temporal width changes. The underlying phenomenon is called dispersion, which is the dependence of the refractive index on the frequency. Here, two different types of dispersion for single-mode fibers are considered, namely: material dispersion and waveguide dispersion.

If an optical pulse (which can be considered as a wavepacket comprising a number of distinct frequency components) propagates through silica glass, its frequency components will experience different phase velocities caused by slightly different refractive indexes. Thus, the pulse width spreads depending on its spectral bandwidth. In Fig. 2.7a the refractive index of fused silica as a function of the wavelength is shown and, in Fig. 2.7b, the corresponding pulse-width broadening for an ultrashort pulse propagating through fibers of different lengths is illustrated. Dispersion generally acts in the frequency domain and, according to Eq. (2.7), this can be expressed as

$$\mathcal{E}(\mathbf{r}, t) = \frac{1}{2} F(x, y) \Re \left\{ \exp\left(i\beta_0 z\right) \int_{-\infty}^{\infty} \tilde{A}(z, \Omega) \exp\left[i\left(\sum_{m=1}^{M} \frac{\beta_m}{m!} \Omega^m - \Omega t\right)\right] \mathrm{d}\Omega \right\} \hat{\mathbf{x}}, \quad (2.37)$$

with $\Omega = \omega - \omega_0$ and β_m being the mth expansion coefficients of the wave number, as defined by Eq. (2.6).
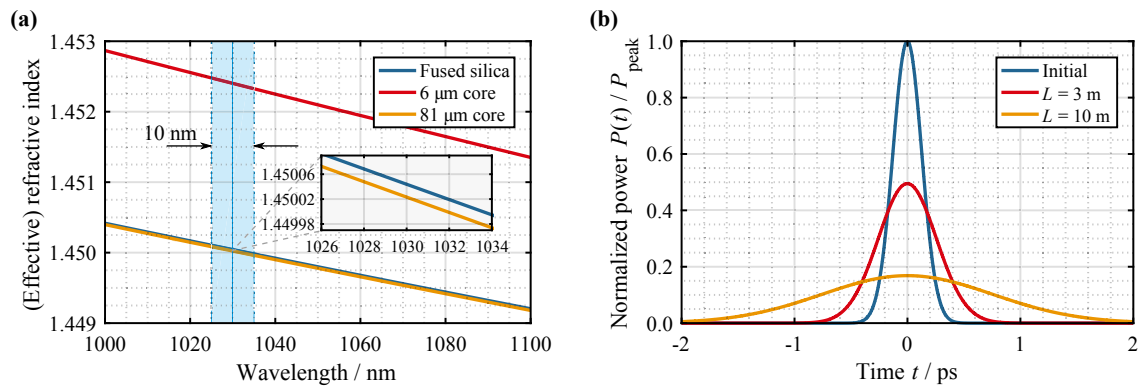
Figure 2.7.: (a) Refractive index for fused silica (material dispersion regarding Sellmeier equation [26]) and simulated effective refractive index (chromatic dispersion) for both a 6 µm-core step-index fiber and an 81 µm-core LPF as a function of the wavelength. A 10 nm bandwidth around 1030 nm is highlighted in blue. (b) Pulse broadening induced by dispersion assuming a pulse duration of $T_0 = 300$ fs and fiber lengths of $L = 3$ m and 10 m and $\beta_2 = 19 \, \text{fs}^2/\text{mm}$ [26] (the pulse form $P(t)$ is normalized to its initial peak power P_{peak}, after [26]).

Furthermore, the waveguide itself can have an impact on the propagation constant[17] $\beta(\omega) = k_0 n_{\text{eff}}(\omega)$. Here, the effective refractive index $n_{\text{eff}}(\omega)$ is affected by the waveguide design. Waveguide dispersion cannot be separated from the material dispersion and their sum is referred to as chromatic dispersion [58]. In Fig. 2.7a the chromatic dispersion of both a 6 µm-core step-index fiber and an 81 µm-core LPF is shown. As can be seen, for large-core fibers the impact of the waveguide dispersion is negligibly small and it is sufficient to consider only material dispersion.

Although dispersion is typically an unwanted effect in ultrafast amplifiers, it can be exploited to mitigate nonlinear effects. Here, an ultrashort pulse is stretched in time prior to amplification by using a large amount of dispersion which imprints a chirp (compare to Fig. 2.7b). The angular dispersion of optical gratings can be converted into a temporal delay (using multiple passes), which typically is orders of magnitude larger than what is reasonable exploiting material dispersion. After amplification, the pulse is compressed to its initial duration by removing the chirp (using dispersion of opposite sign), resulting in pulse-peak powers beyond the limitations of the amplifier medium using non-stretched pulses. This successful concept is known as chirped-pulse amplification (CPA) [28] and is the core of most state-of-the-art high-power ultrafast laser systems. For most simulations in this work, the pulses are considered to be in the so-called CPA regime, in which the temporal pulse shape resembles the spectrum [61].

---

[17]In the context of optical fibers, the propagation constant typically is denoted by $\beta(\omega)$ and not by $k(\omega)$, as done for free space.

2.4.2. Nonlinear Effects

In linear optics, the interaction of light with a dielectric medium causes a polarization density $\mathbf{P}(\mathbf{r}, t)$ in it that depends linearly on the electric field strength $\mathbf{E}(\mathbf{r}, t)$. This harmonic response to the field oscillations will become anharmonic, if the field is strong enough. In this case $\mathbf{P}(\mathbf{r}, t)$ can be approximated as a power series of the form [59]

$$\mathbf{P}(\mathbf{r}, t) = \epsilon_0 \left(\chi^{(1)} \cdot \mathbf{E}(\mathbf{r}, t) + \chi^{(2)} \vdots \mathbf{E}(\mathbf{r}, t)^2 + \chi^{(3)} \vdots \mathbf{E}(\mathbf{r}, t)^3 + \cdots \right), \qquad (2.38)$$

with ϵ_0 being the vacuum permittivity and $\chi^{(n)}$ being the nth-order susceptibility tensors[18]. Thus, while at low field strengths $\chi^{(1)}$ provides the dominant contributions, at high field strengths the contribution of the higher order terms of $\chi^{(n)}$ becomes significant. Since $\chi^{(2)}$ effects are only present in media without inversion symmetry (e.g. crystals), this term vanishes for silica glass (the common host material for optical fibers). On the other hand, in silica a variety of different $\chi^{(3)}$-effects exists, but in the following only those relevant for this work are considered.

Self-Phase Modulation (SPM)

At significant field strengths, the refractive index of an optical fiber becomes intensity-dependent. This is known as nonlinear refraction or optical Kerr effect. This dependence can be expressed as [26]

$$n(I) = n_0 + n_2 I, \qquad (2.39)$$

with n_0 being the linear refractive index and n_2 being the nonlinear-index coefficient[19]. The magnitude of n_2 varies across literature, while $n_2 = 3.2 \cdot 10^{-20}\,\mathrm{m^2/W}$ [59] at a wavelength of $1\,\mu\mathrm{m}$ fits best most of the experimental observations. Due to the tensor nature of $\chi^{(3)}$ this value depends on the state of polarization of the electric field. Thus n_2 is 1.5 times lower for circularly polarized light than for linearly polarized light [62].

Since an optical pulse has a time-varying shape, the Kerr effect will cause a temporal phase change upon propagation [26]:

$$\phi_{\mathrm{NL}}(z, T) = \gamma \int_0^z |A(z', T)|^2 \mathrm{d}z', \qquad (2.40)$$

---

[18]Please note that Eq. (2.38) implies an instantaneous response of the medium (e.g. neglecting the Raman effect) [26].

[19]The term $n_2 I$ requires the definition $n_2 = \dfrac{3}{4n_0^2 \epsilon_0 c} \Re\left\{\chi^{(3)}\right\}$, such that $[n_2] = 1\,\mathrm{m^2/W}$ [59].

where $A(z,T)$ is the pulse envelope, see for example Eq. (2.9), considered in the moving frame $T = t - \beta_1 z$. The nonlinear parameter γ is given by

$$\gamma = \frac{\omega_0 n_2}{c A_{\text{eff}}}, \tag{2.41}$$

with the effective area A_{eff} given by Eq. (2.3). As a result of Eq. (2.40), new frequency components are generated, which broadens the spectrum of the pulse and may transfer some amount of the energy from the main pulse into side pulses[20]. This phenomenon is referred to as self-phase modulation (SPM). The maximum nonlinear phase generated by the pulse-peak power P_{peak} and accumulated along an amplifier of length L is defined by the so-called B-integral, which is [63]

$$B = \gamma \int_0^L P_{\text{peak}}(z) \mathrm{d}z. \tag{2.42}$$

Assuming stretched pulses with a Gaussain-like shape and no phase compensation being applied, the B-integral should be kept somewhere below $B \lesssim 3 \dots 5\,\text{rad}$ at the output of high peak-power laser systems to avoid serious pulse distortions [49].

Self-Focusing (SF)

The spatial counterpart of SPM is self-focusing (SF), which is caused by the intensity-dependent refractive index (Eq. (2.39)), changing across the spatial beam profile rather than along the temporal pulse shape. Hence, according to Eq. (2.10), the beam center experiences a higher refractive index than its periphery, resulting in a focusing lens. The point where self-focusing balances the diffraction of the beam is given by the critical power [59]

$$P_{\text{cr}} = \frac{\pi (0.61)^2 \lambda_0^2}{8 n_0 n_2}, \tag{2.43}$$

for which the beam width remains constant. At powers $P > P_{\text{cr}}$ the beam will be focused and may cause unavoidable damage of the material. Equation (2.43) holds, in good approximation, also for fibers [64]. For fused silica ($n_0 = 1.45$ [65]) and a wavelength of $1030\,\text{nm}$, $P_{\text{cr}} \approx 3\,\text{MW}$ for linearly polarized light and can be increased to $P_{\text{cr}} \approx 5\,\text{MW}$ for circular polarization [62].

---

[20]This holds for transform-limited pulses. Depending on the initial chirp of the pulse frequency components can also vanish.

Nonlinear Polarization Rotation (NLPR)

Nonlinear polarization rotation (NLPR) in optical fibers [66–68] is a phenomenon that is caused by the effects of SPM, cross-phase modulation (XPM) [26] and a weak birefringence (see Subsec. 2.3.2), which leads to a peak-power-dependent change in the polarization state of a pulse coupled into a fiber. Typically, fibers are assumed to exhibit negligible birefringence, which may only be caused by production tolerances of the particular fiber, due to, for example, frozen tensions, torsion or geometrical deviations from a perfectly shaped structure. In particular, considering a (weakly) linear birefringent fiber, an axis of symmetry is introduced allowing to split both polarization components (see Sec. 2.3 Eq. (2.32)) with respect to that axis. The phase difference between both polarization components created by this intrinsic birefringence will be enhanced by the effect of XPM, inducing nonlinear birefringence[21] [69]. Degenerated four-wave-mixing [26] then can cause an energy transfer between both polarization components resulting in a rotation of the polarization ellipse.

2.4.3. Pulse Propagation Equation

The evolution of linearly polarized pulses in optical fibers including both nonlinear effects and dispersion is governed by the so-called nonlinear Schrödinger equation [26]. Assuming a perfectly cylindrical fiber cross-section with only one linearly polarized pulse present in the fiber it is

$$\frac{\partial A(z,T)}{\partial z} + \frac{i\beta_2}{2}\frac{\partial^2 A(z,T)}{\partial T^2} + \frac{\alpha}{2}A(z,T) = i\gamma|A(z,T)|^2 A(z,T), \qquad (2.44)$$

with γ being the nonlinear parameter given by Eq. (2.41), α being, depending on its sign, either an absorption or gain coefficient and β_2 being the second-order expansion coefficient of the propagation constant[22].

A popular approach for solving these equations numerically is the so-called split-step Fourier method [26]. Herein, the propagation of the optical field is divided in small slices where nonlinear effects and dispersion are considered to act independently from one another. Thus, the respective effect can be applied alternately in time and frequency domain, where the numeric calculation works best.

---

[21]Note that this phase difference leads to a change of its ellipticity and not of the orientation of the ellipse (see Sec. 2.3 Fig. 2.6).

[22]For the simulations done within this work only the second-order dispersion is considered. If necessary, higher-order dispersion terms can be added according to Eq. (2.6) [26].

3. Spatial and Temporal Combination of Ultrashort Pulses

In many performance-hungry fields, in which the capacity of a single processing unit is exhausted, parallelization is the scaling technique of choice. Very similarly, this concept has also been transferred to lasers. The combination of pulses or beams from several lasers or amplifiers allows for the operation above the limits of a single-emitter. The first demonstrations of the combination of continuously emitting lasers date back to the 70's with the evanescent coupling of adjacent semiconductor oscillators [70, 71].

Although there is a diversity of combination techniques that do not exclude each other, two major differentiations are made within this work, which are represented by Fig. 3.1. The first one is between phase-sensitive and non-phase-sensitive combination [72]. While the phase-sensitive approaches refer to those with temporally stable phase relationships between the beams, in the non-phase-sensitive approaches this relative phase stability is not mandatory. Second, it can be distinguished between the signals having the same or different spectra. In both non-phase-sensitive cases, beams of separate lasers are either incoherently superposed [73, 74] or placed side-by-side [75], resulting simply in the addition of their average powers. Thus, these are viable approaches for continuously emitting lasers or pulsed lasers with pulse durations longer than nanoseconds [76]; the temporal triggering of shorter pulses is not feasible with current conventional electronic delays. Moreover, the narrow spectra are advantageous for spectral side-by-side packing. Such lasers are of interest for applications where the temporal and the spatial quality of the signal are not of concern, for example as in high-power pump diode bars. Today, the achievable average power from fiber-based systems combined using non-phase-sensitive methods reaches up
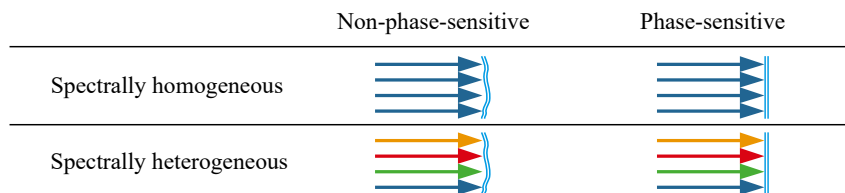

Figure 3.1.: Classification of the diverse combination approaches.

to 100 kW [77–79]. However, non-phase-sensitive combining approaches will not be further addressed within the scope of this work, since, in order to ensure the synchronization of ultrashort pulses, in practice phase-sensitive combining approaches have to be considered.

If all the signals have identical spectra and are coherent to each other, their superposition will lead to interference. Thus, their relative phases are either self-organized (referred to as passive stabilization) [80–86] or controlled by an external feedback loop (referred to as active stabilization) [87–90], such to result in constructive interference. As sources for the combination it is possible to use, for example, phase-locked continuously emitting lasers [87, 89, 91–93] or even femtosecond pulses that are amplified in separate fiber amplifiers [88, 90]. Furthermore, spectral synthesis for additional pulse shortening [94–96] or to counteract gain narrowing [97, 98] has also been demonstrated using phase-sensitive combination techniques.

In this chapter, the phase-sensitive combination of spectrally homogeneous ultrashort pulses will be considered in more detail. A further distinction is made between spatial and temporal combination, which are discussed in Sec. 3.1 and Sec. 3.2, respectively. Although these approaches are applicable to different laser architectures [33–36], the focus is set on ultrafast fiber-laser systems, since the unique properties of fibers make them ideal candidates for these concepts. First, polarization-based spatial pulse division and combination are introduced. In this context, the impact of beam- [99, 100] and pulse-parameter [101] mismatches on the combination efficiency is covered, which forms the basis of the combination process. As part of this work, the temporal combination is discussed as an energy-scaling concept. Therefore, the requirements on polarization-based temporal pulse division and combination are analyzed. Furthermore, the amplification of temporally divided pulses and their combination in passively phase-stable architectures are discussed. These considerations constitute the basis for the experiments, which will be presented in Chap. 5 and pursue the goal of merging both the spatial and the temporal combination approaches in a single power- and energy-scalable system. Finally, this could be demonstrated for the first time and allowed for unprecedented performance of up to 12 mJ femtosecond pulses at an average power of 700 W delivered by a fiber-based system.

3.1. Spatial Combination

The separation of the amplification process among several parallel amplifiers or lasers and the subsequent superposition of the emitted beams or pulses is referred to as spatial combination. A requirement for constructive superposition is mutual coherence. Although it has been demonstrated that pulses from independent oscillators can be synchronized

passively via optical coupling due to injection seeding [80], the focus in this thesis is on the combination of amplifiers. In order to ensure intrinsic mutual coherence between the pulses to be combined, a single source is used to seed an amplifier array, as illustrated in Fig. 3.2.
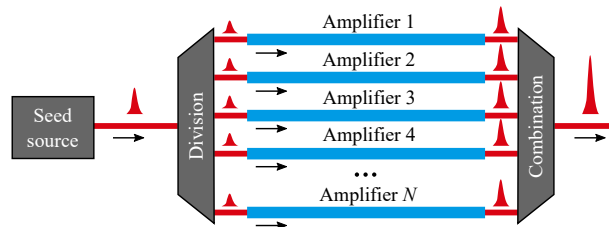

Figure 3.2.: Illustration of a coherent amplifier array comprising N parallel amplifiers seeded by a single source with subsequent combination.

The coherent combination allows operating the laser system at performance levels beyond the physical limitations of a single amplifier. From a simplified point of view, the use of N channels allows for scaling both the average power and the pulse energy by a factor of N. However, any beam- or pulse-parameter mismatch will affect the combination and, hence, reduce this factor, which will be discussed later on in Subsec. 3.1.3. In the following section, some beam division and combination approaches are considered.

3.1.1. Division and Combination Approaches

Usually, beam division is achieved via intensity beam splitters (IBSs) or polarizing beam splitters (PBSs). In Fig. 3.3a, these two possibilities are schematically depicted[1]. IBSs provide a fixed splitting ratio and maintain the state of polarization of the incident beam. PBSs are typically used in combination with a half-wave plate (HWP) to provide a variable splitting ratio between the separated orthogonally-polarized components. Both types of beam division can be cascaded, in order to end up with a number N of beams. Typically, tree-type implementations of these approaches are employed, as depicted in Fig. 3.3b. In this case, the power is equally distributed among the beams assuming a constant splitting ratio of one (50:50) for each beam splitter. Another possibility is, for example, a bus-type implementation, as shown in Fig. 3.3c. Here, a variable splitting ratio is required in order to obtain, again, an equal power distribution among the separated beams. Although there are IBSs that exhibit different splitting ratios commercially available, this can be achieved in a flexible way by employing combinations of HWPs and PBSs, which will be

---

[1]The approach based on using diffractive optical elements (DOEs) [102] is not considered here, since in the context of ultrashort pulses a lot of effort has to be made to compensate for angular dispersion [72]. However, this approach has already been demonstrated in continuous-wave operation [103, 104].
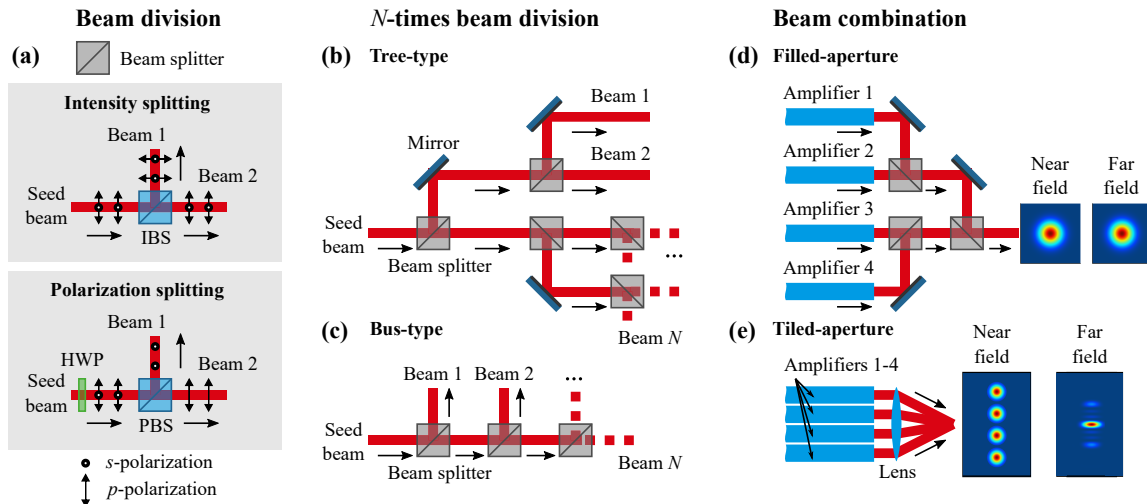
Figure 3.3.: (a) Beam division with an intensity beam splitter (IBS) or with a combination of a half-wave plate (HWP) and a polarizing beam splitter (PBS). Cascaded beam division into a number of N beams via a (b) tree-type and (c) bus-type implementation. Beam combination in (d) filled-aperture (illustrated for a tree-type implementation) and (e) tiled-aperture implementation. Beam profiles in the near and the far field are shown.

considered in more detail in Subsec. 3.1.2. Generally, for a division on N channels $N-1$ beam splitters are required. There is also an all-fiber solution with the advantage that an amplifier can be easily introduced in each dividing branch [105]. However, since in high-power operation the required initial seed power for N channels can become remarkable for a moderate N, nonlinear effects are severe and non-bendable rod-type fibers may have to be employed, for which fiber-beam splitters are not available, yet.

Beam combination is typically done in free space, due to the high intensities appearing. Here, a further differentiation can be made between tiled- or filled-aperture implementations [75]. In the former case, the beams from a parallel amplifier array are superposed in the far field. In the latter case, the beams are superposed both in the near and the far field employing a similar beam-splitter arrangement as for the beam division but in reverse order. As illustration, in Fig. 3.3d-e both implementations and their resulting beam profiles are shown for the combination of four beams emitted by parallel amplifiers. Assuming identical beam parameters at the output of each amplifier channel and with an ideal beam overlap, the beam parameters remain unchanged upon combination in the filled-aperture case. However, although the tiled-aperture implementation requires significantly less combination elements, it suffers from poor efficiency [72]. Therefore, the filled-aperture approach (illustrated in Fig. 3.3d for a tree-type implementation) is preferred in most situations, as long as the final combination element can withstand the envisioned laser parameters. In the following, beam division and filled-aperture combi-

nation via polarization are considered in more detail, since this is the technique used for the experiments within this work. As part of this thesis, the impact of non-idealized polarizers is discussed.

3.1.2. Polarization Beam Combination

In this section, the beam division and combination by means of polarization are considered in more detail. Figure 3.4 shows an illustration of a two-channel polarization beam combination setup employing combinations of HWPs and PBSs. Within this thesis, such a scheme will be referred to as tree-type implementation. We assume an initially p-polarized pulse defined by the Jones vector $\mathbf{J}_0 = A_\mathrm{p}\hat{\mathbf{p}}$ (note that $\hat{\mathbf{p}} = \hat{\mathbf{x}}$ and the temporal dependence is omitted) according to Eq. (2.34). Using now the Jones matrices for a rotated HWP and, for the more generalized case, a non-idealized polarizer from Tab. 2.1, the signals at both the transmission and reflection port of the PBS are

$$\left.\begin{aligned}\mathbf{J}_\mathrm{T} = \mathcal{M}_\mathrm{T}(T_\mathrm{p}, R_\mathrm{s})\mathcal{M}_\mathrm{HWP}(\theta)\mathbf{J}_0,\\ \mathbf{J}_\mathrm{R} = \mathcal{M}_\mathrm{R}(T_\mathrm{p}, R_\mathrm{s})\mathcal{M}_\mathrm{HWP}(\theta)\mathbf{J}_0,\end{aligned}\right\} \tag{3.1}$$

with the indices T and R denoting transmission and reflection at the PBS. In the idealized case of $T_\mathrm{p} = R_\mathrm{s} = 1$, an orientation angle $\theta = 22.5°$ of the HWP with respect to the p-polarization axis results in a rotation of the incoming linear polarization by $45°$. Hence, for incident p- or s-polarized pulses an equal power division for both orthogonal polarization components $|A_\mathrm{p}|^2 = |A_\mathrm{s}|^2$ is obtained. For clarity, an overview of the evolution of the
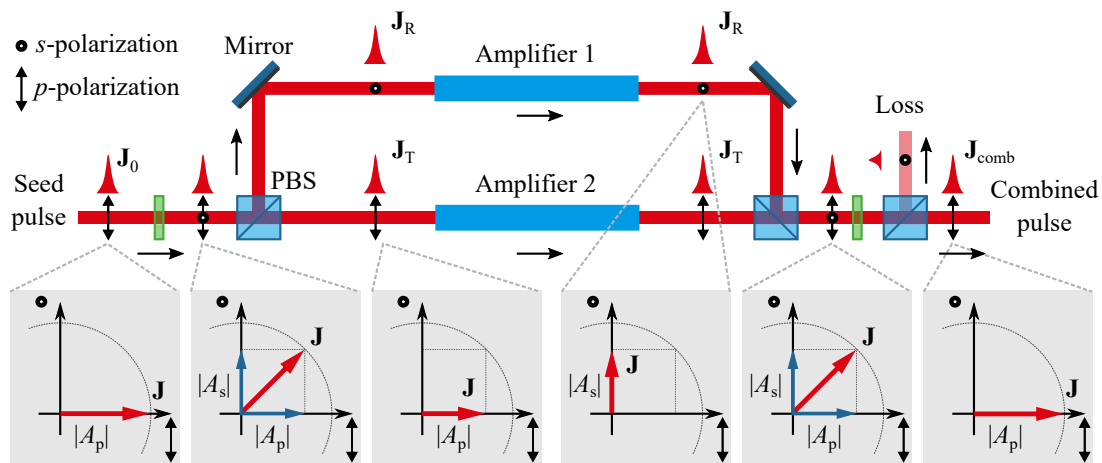

Figure 3.4.: Scheme of a two-channel polarization beam combination setup employing half-wave plates (HWPs) and (idealized) polarizing beam splitters (PBSs). The evolution of the state of polarization is illustrated under the setup via Jones vectors $\mathbf{J}$ (a phase jump between both polarization components has been omitted).

orientation of the polarization vector is additionally depicted in Fig. 3.4.

After amplification of the pulses in their respective channel, beam combination is achieved in an analogous way as beam division. The individual orthogonally-polarized pulses are superposed at a PBS, resulting in a 45° inclined linear polarization state. Deviations from the expected polarization state will cause a loss at a subsequent polarizer. Therefore, another HWP and PBS are employed in order to separate the combined and the uncombined parts, i.e. to clean the beam. Considering the combination of the two beams $\mathbf{J}_\mathrm{R} = A_\mathrm{s}\hat{\mathbf{s}}$ (note that $\hat{\mathbf{s}} = \hat{\mathbf{y}}$) and $\mathbf{J}_\mathrm{T} = A_\mathrm{p}\hat{\mathbf{p}}$ and assuming an additional final polarizer transmission, the combined output is

$$\mathbf{J}_\mathrm{comb} = \mathcal{M}_\mathrm{T}(T_\mathrm{p}, R_\mathrm{s})\mathcal{M}_\mathrm{HWP}(\theta)\left[\mathcal{M}_\mathrm{R}(T_\mathrm{p}, R_\mathrm{s})\mathbf{J}_\mathrm{R} + \mathcal{M}_\mathrm{T}(T_\mathrm{p}, R_\mathrm{s})\mathbf{J}_\mathrm{T}\right]. \qquad (3.2)$$

Finally, using Eq. (2.32), the intensity of the combined beam is

$$I_\mathrm{comb} \sim T_\mathrm{p}\left[T_\mathrm{p}\cos^2(2\theta)|A_\mathrm{p}|^2 + R_\mathrm{s}\sin^2(2\theta)|A_\mathrm{s}|^2 + \sqrt{T_\mathrm{p}R_\mathrm{s}}\sin(4\theta)A_\mathrm{s}A_\mathrm{p}^*\cos(\Delta\phi)\right]. \qquad (3.3)$$

Any phase mismatches $\Delta\phi = \phi_\mathrm{s} - \phi_\mathrm{p}$ between the orthogonally-polarized superposed beams will change the resulting polarization state from linear to elliptical (or even circular) polarization, equivalent to that shown in Fig. 2.6. Hence, this will cause a power loss at the final polarizer. The implementation shown in Fig. 3.4 is similar to a Mach-Zehnder interferometer. Thus, in order to obtain constructive interference at the output, the optical paths have to be matched. Moreover, any perturbations for that need to be compensated for to keep the constructive interference, making an active stabilization necessary, which will be covered in Chap. 4.

Typically, non-ideal PBSs are characterized by $T_\mathrm{p} < R_\mathrm{s} < 1$ [106], given by their particular dielectric reflection-layer design. In Fig. 3.5a, the effect on the beam division is illustrated. As a consequence, the residual amount of T_p and R_s lead to a leakage of the unintended polarization components to the opposite ports of the PBS, i.e. reflection of the p-component and transmission of the s-component. It is worth noting that an equal power-division will not result in orthogonal pulses at both output ports due to the leakage at the PBS. For illustration purposes, this impact is illustrated in Fig. 3.5b for arbitrarily chosen $T_\mathrm{p} = 0.8$ and $R_\mathrm{s} = 0.9$. Additionally, the idealized case of $T_\mathrm{p} = R_\mathrm{s} = 1$ is also shown as functions of the orientation angle θ of the HWP with respect to the p-polarization axis. Here, the power for the transmitted and reflected s- and p-polarization components are denoted by $|A_\mathrm{T/R,p}|^2$ and $|A_\mathrm{T/R,s}|^2$, respectively. In the perfect case, an equal power division is obtained at $\theta = 22.5°$, but this changes for the non-perfect case. Upon combination, those leakages lead to an intrinsic power loss for spatial combination
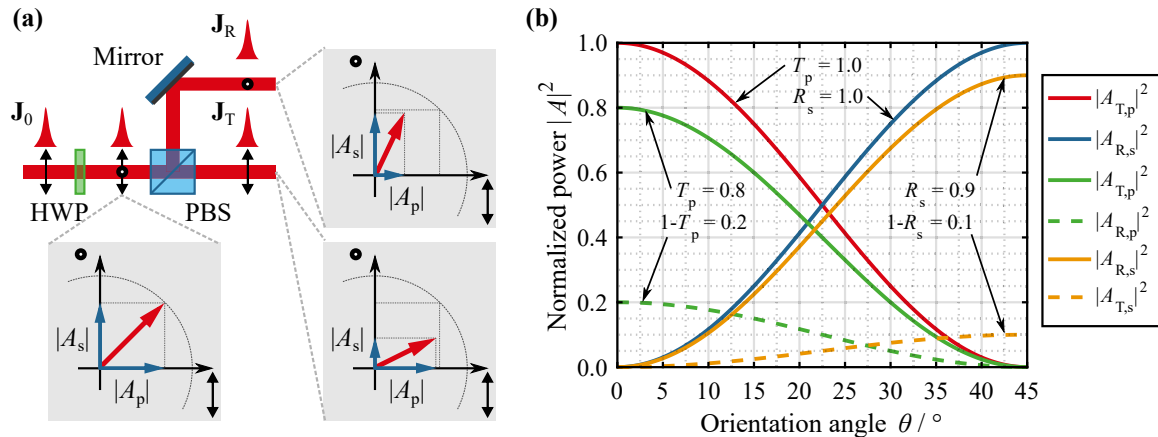
Figure 3.5.: (a) Polarizing pulse division using a combination of half-wave plate (HWP) and non-idealized polarizing beam splitter (PBS). An initially *p*-polarized pulse given by its Jones vector $\mathbf{J}_0$ is divided into both the reflected pulse $\mathbf{J}_R$ and the transmitted pulse $\mathbf{J}_T$. Additionally, the vectorial decomposition of a Jones vector $\mathbf{J}$ into its polarization components $|A_p|$ and $|A_s|$, respectively, is illustrated. (b) Transmitted and reflected powers $|A_{T/R,p}|^2$ and $|A_{T/R,s}|^2$ as a function of the orientation angle θ of the HWP with respect to the *p*-polarization axis. Both $T_p = R_s = 1.0$ for perfect division and $T_p = 0.8$ and $R_s = 0.9$ for non-perfect division are illustrated.

setups. In temporal combination additionally the pulse contrast is affected, which will be considered in Sec. 3.2.

In order to divide a beam into an array of $N > 2$ amplifiers, cascaded beam-splitter arrangements as depicted in Fig. 3.3b-c can be employed. There are slight differences between tree-type and bus-type implementations regarding the number of transmissions and reflections in PBSs. In general, the division procedure in a tree-type implementation can be considered, in the ideal case, as binary steps. For the final experiment, a combination of both implementations is applied. While the division step in two branches is done in a tree-type manner (Eq. (3.1)), further channels are added to each branch in a bus-type configuration. Thus, the *m*th beam at division step $m = 1, 2 \ldots, M$ can be expressed as[2]

$$\mathbf{J}_m = \mathcal{M}_R(T_p, R_s)\mathcal{M}_{HWP}(\theta_m) \left\{ \prod_{j=1}^{m-1} \mathcal{M}_T(T_p, R_s)\mathcal{M}_{HWP}(\theta_{m-j}) \right\} \mathbf{J}_{T/R}, \qquad (3.4)$$

with $\mathbf{J}_{T/R}$ defining either the initially transmitted or reflected beam, which results ultimately in M beams (that are reflected in PBSs) in each branch. The subsequent beam combination is achieved in a similar way as beam division. Finally, the efficiency of the combination is an important quantity. It depends on several parameters, which will be investigated in the following section.

---

[2]Please note that the matrix multiplication is not commutative.

3.1.3. Efficiency of the Combination Process

As mentioned earlier, theoretically, a linear improvement of both the average power and the pulse energy with the number of combined amplifier channels can be obtained. Unfortunately, in real experimental conditions beam- or pulse-parameter mismatches are unavoidable, which will reduce the theoretical scaling factor. In the following, an efficiency parameter for the combination process is defined and detrimental effects are discussed.

Definition of the Efficiency

In order to evaluate the beam and pulse combination, the so-called combination efficiency is introduced, which is the most common definition for spatial combination. It is, for N amplified pulses to be combined, given by

$$\eta_{\mathrm{comb}}^{\mathrm{spat}} = \frac{\bar{P}_{\mathrm{comb}}}{\sum\limits_{n=1}^{N} \bar{P}_n'}, \tag{3.5}$$

with $\bar{P}_{\mathrm{comb}}$ denoting the combined output average power and $\bar{P}_n'$ being the average power of the nth channel at the system output. The combination efficiency results in values between zero and one and considers strictly the physical combination of the pulses and beams disregarding any losses, for example, induced by the combination elements or depolarization of the amplifiers. Practically, its the ratio of the measured output average power $\bar{P}_{\mathrm{comb}}$ to the sum of the individual powers $\bar{P}_n'$ of each amplification channel measured at the output of the system. This definition is easy to measure under experimental conditions and, in good approximation, it cancels out the losses introduced by the combination elements. However, it does not allow for a correct comparison with single amplifier systems, since the additional number of optical elements placed in the beam path introduce losses. Therefore, the system efficiency [107] can be introduced, which is

$$\eta_{\mathrm{sys}}^{\mathrm{spat}} = \frac{\bar{P}_{\mathrm{comb}}}{\sum\limits_{n=1}^{N} \bar{P}_n}, \tag{3.6}$$

where $\bar{P}_n$ denote the average powers directly at the amplifier outputs with $\bar{P}_n \geq \bar{P}_n'$. Thus, any losses introduced by the combination elements are included, which may be of concern for a large element-count. However, for practical reasons it might be difficult to access these measuring points, making an estimation of the power-transmission for the individual channels through their respective combination branches necessary. In the following, the

impact of beam- and pulse-parameter mismatches on the efficiency of the combination is analyzed and the requirements on beam-alignment precision are given.

Beam-Parameter Mismatches

As mentioned above, any beam- or pulse-parameter mismatch results in a decrease of the combination efficiency. According to Eq. (2.7), typically the impact of spatial and temporal mismatches can be studied independently. For now, only spatial mismatches, such as beam-size differences, beam displacement, beam tilt, optical path differences and power variations, as schematically depicted in Fig. 3.6a, are considered.

Generally, the initial beam parameters are defined by the emitting fiber and they will remain constant over subsequent pulses. Thus, the same considerations as for continuous-wave operation hold [99, 100]. First, the impact of a beam tilt is discussed. For simplicity, the superposition of two beams, each being defined by Eq. (2.11) at position $z = 0\,\mathrm{m}$, is considered[3]. Assuming that beam 1 and beam 2 have the same beam waist diameters $2w_{01} = 2w_{02} = 2w_0$, the impact of a tilt of one of these beams by an angle α as a function of the beam size is shown in Fig. 3.6b. As can be seen, the effect of a misaligned beam pointing becomes stronger for larger beam sizes, since the spatial phase differences become more pronounced. For example, while a pointing accuracy of $\alpha \approx 60\,\mathrm{\mu rad}$ is required for beam diameters of $2w_0 = 2\,\mathrm{mm}$ to keep the combination efficiency $\eta_{\mathrm{comb}}^{\mathrm{spat}} \geq 99\%$, it has to be about five times more precise for a beam of $2w_0 = 10\,\mathrm{mm}$. Moreover, variations in the power[4] and the beam waist positions, i.e. a difference in the optical paths (Fig. 3.6a), can lead to a degradation of the efficiency, which is summarized in Fig. 3.6c. In absence of nonlinear effects (Subsec. 2.4.2), the power ratio P_2/P_1 between both beams has to be within about 30% to keep $\eta_{\mathrm{comb}}^{\mathrm{spat}} \geq 99\%$, i.e. it is rather tolerant. The optical path difference Δz has to be aligned within half the Rayleigh length z_{R}, i.e. it becomes more difficult for small beam sizes. Here, both slight differences in the beam size and in the wavefront curvature lead to a combination mismatch. The impact of these two parameters on the temporal pulse stacking will be considered in Chap. 5. Furthermore, relative differences in the beam waist sizes w_{02}/w_{01} and parallel beam displacement Δs (Fig. 3.6a) normalized to $2w_{01}$ as reference are summarized in Fig. 3.6d. Again for $\eta_{\mathrm{comb}}^{\mathrm{spat}} \geq 99\%$, while the relative beam waist sizes can differ by almost 20%, the lateral displacement

---

[3]Please note that due to the Gaussian beam propagation the combination efficiency can be different for beams being superposed at $z \neq 0\,\mathrm{m}$.

[4]Here, a constant spitting ratio (50:50) of the combination element is assumed and power variations related to that situation are considered. Please note that non-matched powers in polarization-beam-combination setups, according to Fig. 3.4, result in a departure from 45° of the orientation of the linear polarization of two superposed *s*- and *p*-polarized beams, which can be compensted by a subsequent HWP. In this way, the spitting ratio has to be adjusted, for example, for bus-type combination schemes.
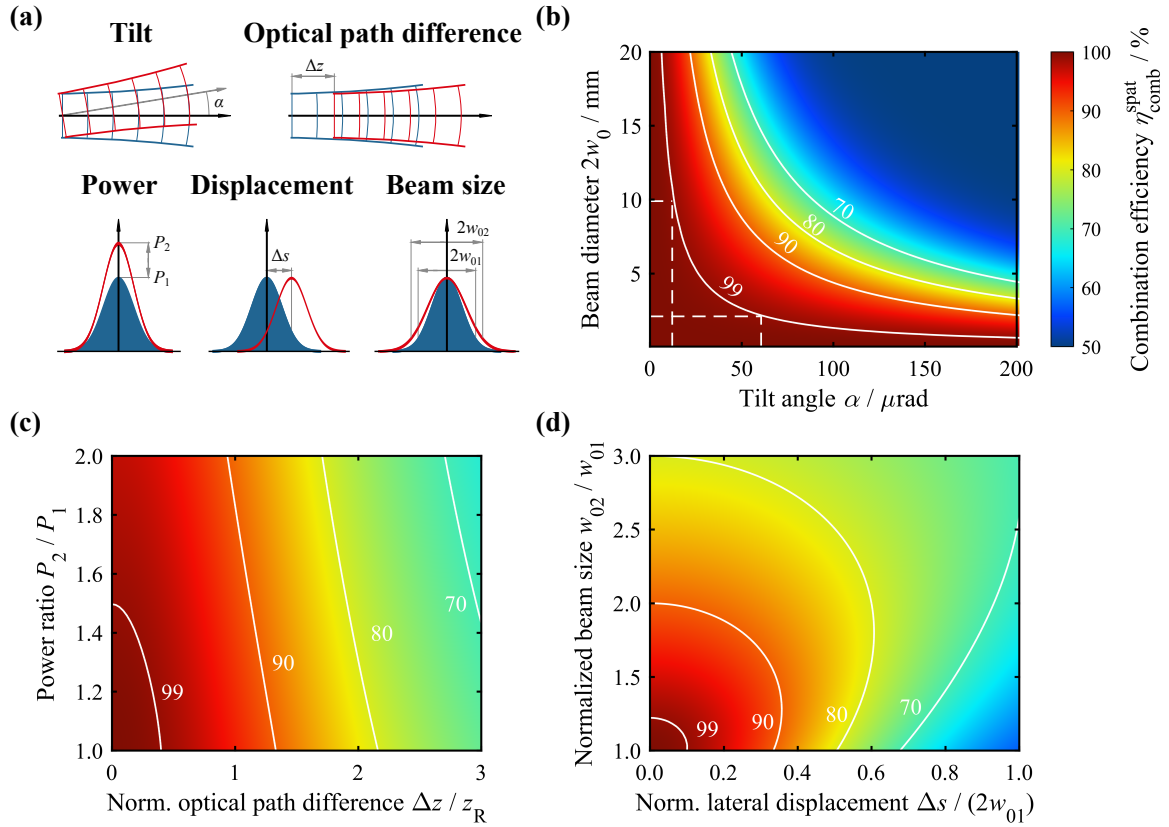
Figure 3.6.: (a) Pictographs describing spatial effects that have a detrimental impact on the combination efficiency between two beams. Dependence of the combination efficiency $\eta_{\text{comb}}^{\text{spat}}$: (b) on a beam tilt α between two beams having the same beam waist diameter $2w_0$; (c) on an optical path difference Δz normalized to the Rayleigh length z_{R} and on the power ratio P_2/P_1 between both beams; (d) on the ratio between both beam sizes w_{02}/w_{01} and on the lateral beam displacement Δs normalized to $2w_{01}$ (the carrier wavelength is $\lambda_0 = 1030\,\text{nm}$, the color code is identical for (b)-(d)).

with respect to the beam diameter needs to be within 10% (for $w_{01} = w_{02}$). Please note that a difference in the beam waists is equivalent to a difference in the divergence angles, since these parameters are connected by the beam-parameter product [49].

In fact, since all effects contribute to the total combination process, everyone of them should be optimized to keep the overall combination efficiency high. However, while the system is fairly tolerant against power variations, the beam sizes and optical path differences, the lateral beam displacement and tilt need to be adjusted more precisely. Under experimental conditions, this is more or less easy to realize with fibers by a careful geometrical beam matching in both the near and the far field. For the free-space beam sizes intended for the experiments, standard mirror mounts are available that allow for obtaining a beam pointing better than 20 µrad and good thermal stability [108, 109].

Pulse-Parameter Mismatches

On top of the beam-parameter mismatches described above, there are also pulse-parameter mismatches that will decrease the combination efficiency as well. In the following, the discussion will be restricted to temporal effects and a Gaussian-pulse shape, as given by Eq. (2.9), will be assumed.

For an efficient combination of two transform-limited pulses, these have to be superposed with sub-wavelength accuracy. As illustration, the superposition of two pulses is considered where one of them is delayed by τ (which manifests as a linear phase $\phi(\omega) = \tau\omega$ in the spectral domain). In Fig. 3.7a the resulting combination efficiency as a function of the delay normalized to the pulse duration T_0 is shown. The fast oscillations arise from interference between the underlying electric fields, which is constructive for $\tau = m\lambda_0/c$, expressed as integer multiples m of the carrier wavelength λ_0 (shown in the inset). Typically, an active stabilization control (see Chap. 4) maximizes the superposition of these oscillations within a certain frequency bandwidth. The walk-off between the pulse envelopes leads to both a decreasing interference contrast and to a lower achievable combination efficiency. This is additionally shown in Fig. 3.7a for pulse durations of $2T_0$ and $3T_0$. Obviously, the bearable delay depends strongly on the transform-limited pulse duration and, thus, on the bandwidth [101]. To keep $\eta_{\text{comb}}^{\text{spat}} > 99\%$ the delay should be matched within $\tau \lesssim 0.2T_0$, which corresponds to an adjustment of the optical path-length difference in the order of $9\,\mu\text{m}$ for $T_0 = 150\,\text{fs}$ with a carrier wavelength of $1030\,\text{nm}$. In first order, this can be easily realized by standard available translation stages [110]. It is worth noting that the same requirement will hold also for stretched femtosecond pulses. This results in a constant phase factor for each divided pulse (phase difference stays the same) and, thus, the bandwidth dependence remains unchanged [101].

As the pulse propagates through a fiber amplifier it accumulates a certain amount of spectral phase caused by dispersion (Subsec. 2.4.1). On top of that, it may accumulate an intensity-dependent temporal phase due to nonlinearities (Subsec. 2.4.2). In order to study the impact of these effects on the combination efficiency, the superposition of two pulses with an initial duration of $T_0 = 150\,\text{fs}$ (corresponding to a bandwidth of $\Delta\lambda \approx 10\,\text{nm}$) is shown in Fig. 3.7b. In this plot one of the pulses is modified by SPM with an absolute B-integral of ΔB and by material dispersion with an equivalent propagation length of ΔL and a refractive index $n(\omega)$ for fused silica (see Fig. 2.7a). The resulting modification of the carrier phase has been corrected for both parameters to have zero phase offset with respect to the envelope. Regarding the experiments in this work, the fibers used for spatial combination do not exceed lengths of about $1.1\,\text{m}$ and, typically, differ in length by less than $3\,\text{cm}$. Thus, the overall impact of this effect on the combination efficiency can
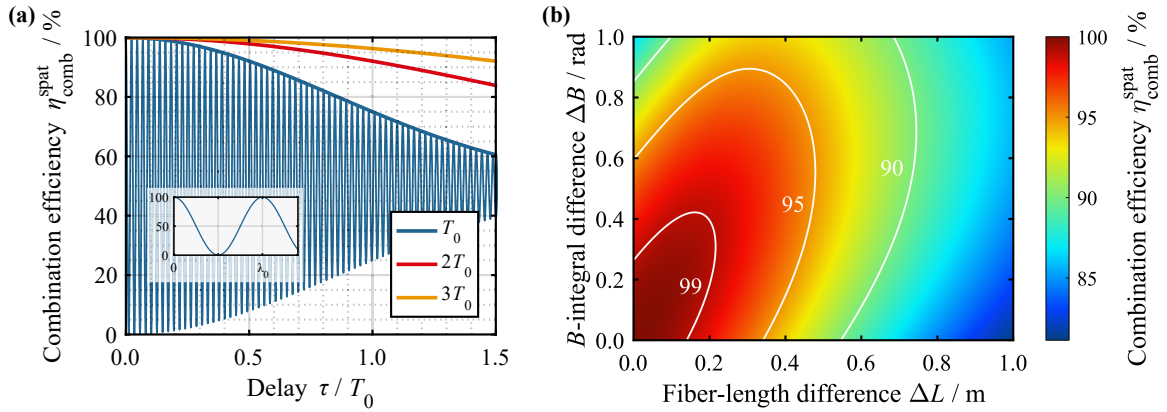
Figure 3.7.: Combination efficiency $\eta_{\text{comb}}^{\text{spat}}$ of two superposed Gaussian pulses of duration T_0 (the carrier wavelength is $\lambda_0 = 1030\,\text{nm}$): (a) Depicted as a function of the temporal delay τ between them ($2T_0$ and $3T_0$ are additionally shown). The oscillations arise from interference between the underlying electric fields and are shown in the inset as a function of the carrier wavelength λ_0. (b) $\eta_{\text{comb}}^{\text{spat}}$ depicted as a function of both the B-integral difference ΔB and the fiber-length difference ΔL for an initial pulse duration of $T_0 = 150\,\text{fs}$ (corresponding to a bandwidth of $\Delta\lambda \approx 10\,\text{nm}$ at $1030\,\text{nm}$).

be considered as negligible. The most important conclusion from Fig. 3.7b is that the B-integrals have to be matched. Within $\Delta L \leq 3\,\text{cm}$ the difference should be $\Delta B \lesssim 0.3\,\text{rad}$ to keep $\eta_{\text{comb}}^{\text{spat}} > 99\%$ for this particular bandwidth being considered. It is worth noting that, according to Eq. (2.42), the B-integral depends on the evolution of pulse-peak power in the fiber. Thus, a B-integral difference can be caused between pulses that are amplified in fibers of different lengths, even though the power at their outputs can be equalized by balancing the pump and/or the seed powers.

3.2. Temporal Combination

Contrary to the spatial combination case presented in the previous section, temporal combination refers to the distribution of the pulse energy among several pulse replicas within a single beam. After serial amplification in an amplifier, this temporal pulse spreading is reversed and the pulse replicas are coherently stacked into a single intense pulse. Generally, serial amplification of several pulse replicas allows operating an amplifier at an energy beyond the nonlinear or damage limitations associated with the amplification of a single intense pulse. In this regard, this strategy can be employed either as extension to or instead of the CPA technique.

There are different temporal combination approaches. In principle, they differ in the generation process of the initial sequence of pulse replicas and, ultimately, in the stack-

ing procedure. Moreover, the intended energy extraction from the amplifier determines whether it is operated in the small-signal amplification regime or in the saturated regime (see Subsec. 2.2.4). In this regard, the two extreme cases which will be referred to here as the continuously-pulsed mode and the burst operation mode, can be considered. These are schematically depicted in Fig. 3.8. In the continuously-pulsed mode the sequence of pulses is directly provided by the seed source typically operating at a high repetition rate (e.g. MHz-level) and, thus, low pulse energy. Therefore, depending on the energy being targeted, a large number of pulses need to be stacked in order to obtain the desired energy gain, making the use of optical cavities necessary [111–114]. On the contrary, in burst mode a sequence of pulse replicas is generated before amplification and it is stacked again afterwards. The repetition rate is typically lower than in the continuously-pulsed case (e.g. kHz-level), potentially providing higher initial pulse energy, which tends to improve the energy extraction. In this case, only a few pulses need to be stacked, for which simple, individual delay lines can be applied [30, 31].

The focus of this work is aimed at the burst mode, which will be extensively covered in the following sections. Within this thesis, pulse division and stacking schemes are discussed and their power-scalability is investigated.

3.2.1. Techniques for Pulse Burst Generation and Stacking

The burst mode has first been demonstrated on excimer lasers [30] and is commonly referred to as divided-pulse amplification (DPA) since its first demonstration using femtosecond pulses [32]. As mentioned above, an initial pulse is split into M temporally delayed pulse replicas prior to amplification. Thereby, the pulse peak power (at the amplifier output) is reduced by a factor of M which mitigates nonlinear effects (see Subsec. 2.4.2) and increases the achievable pulse energy. Ultimately, the pulse replicas are stacked into a single pulse. In the following, approaches to the generation and stacking of bursts of stretched and non-stretched ultrashort pulses are considered. Furthermore, the amplification of pulse bursts is also discussed.
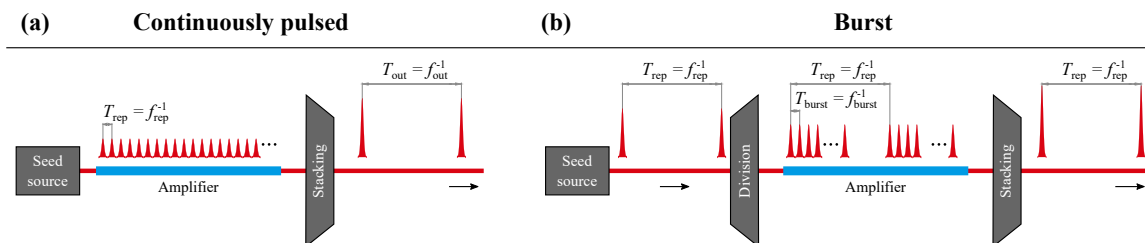

Figure 3.8.: Illustration of temporal combination employing (a) the continuously-pulsed mode and (b) the burst operation mode.

There are different approaches for generating bursts of ultrashort pulses. The most common one is to carve out a sequence out of a continuous pulse train using an acousto-optic modulator (AOM). This approach sets stringent requirements on the pulse-stacking approach (GHz electronics and phase shifters). Another straightforward technique is the temporal separation of the orthogonal polarization components of a linearly polarized pulse. This was first demonstrated using birefringent crystals [115–117]. The difference in the group velocities of the ordinary and extraordinary field components of a pulse (given by $v_{\mathrm{g,o}}$ and $v_{\mathrm{g,e}}$, respectively) traveling through the crystal causes a delay between them. If the crystal[5] is of thickness d, the orthogonally-polarized pulse envelopes will be separated in time by

$$\tau = \frac{d}{c}\left|n_{\mathrm{g,e}} - n_{\mathrm{g,o}}\right| = d\left|\frac{1}{v_{\mathrm{g,e}}} - \frac{1}{v_{\mathrm{g,o}}}\right|, \tag{3.7}$$

with $n_{\mathrm{g,o}}$ and $n_{\mathrm{g,e}}$ being the ordinary and extraordinary group indexes, respectively. For example, calcite provides a delay of $\sim 590\,\mathrm{fs\,mm^{-1}}$ and yttrium vanadate $\sim 740\,\mathrm{fs\,mm^{-1}}$ at $1030\,\mathrm{nm}$ [65]. Typically, these crystals are of several centimeters length at maximum and, thus, can be used to generate replicas of femtosecond and picosecond pulses, at most.

The relative intensity of the separated pulses depends on the orientation angle θ of the optical axis of the crystal with respect to the linear-polarization orientation of the initial pulse. Hence, for $\theta = 45°$ two orthogonally-polarized pulses of equal intensity are obtained. Further divisions can be achieved by cascading several crystals. Such an arrangement consists of crystals with alternating orientations, with those at odd-numbered positions being orientated at $\theta = 45°$ and those at even-numbered positions being orientated at $\theta = 0°$, which is illustrated in Fig. 3.9a. The thickness d_1 of the shortest crystal has to be chosen such that the temporal delay τ_1 leads to a complete separation of two consecutive pulses. Assuming the thickness of the kth subsequent crystal to be $d_k = 2^{k-1}d_1$, a total number K of crystals (where $k = 1, 2, \ldots, K$) results in a burst of $M = 2^K$ equally spaced pulse replicas [32]. The polarization pattern of the final pulse burst depends on the crystal order, which is additionally depicted in Fig. 3.9a. While a crystal stack of steadily increasing thickness generates a burst with the first half being orthogonally polarized to the second half, a stack of steadily decreasing thickness $d_k = 2^{K-k}d_K$ generates a burst of alternating orthogonal polarizations[6]. Please note that insufficient delays would result in an overlap of adjacent pulses. This may cause cross-phase modulation [26] when propagating through a fiber and, moreover, interference effects if they have the same

---

[5]So-called a-cut crystals are considered in which the optical axis lies in the x-y-plane, i.e. perpendicular to the propagation direction [118].

[6]Moreover, equal pulse spacing is no requirement such that the given d_k are rather minimum thicknesses. Furthermore, the crystals can be used in random order, which is not considered here.
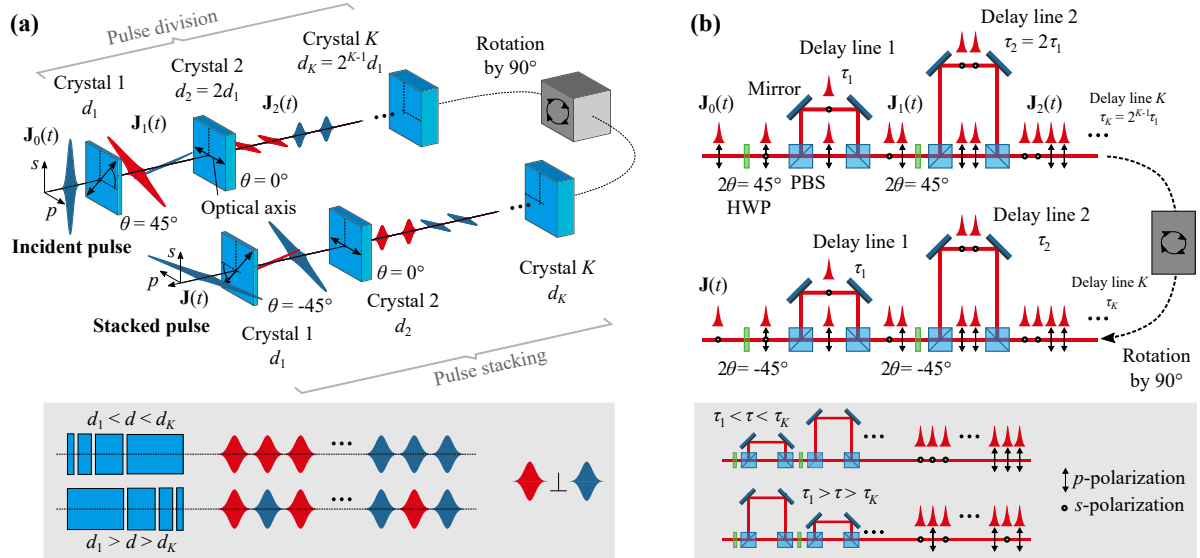
Figure 3.9.: Schematic of the generation and stacking of a pulse burst using (a) birefringent crystals and (b) free-space delay lines comprising half-wave plates (HWPs), polarizing beam splitters (PBSs) and mirrors. Additionally, the impact of the order of the delay-generating elements on the final polarization pattern is shown.

polarization [118].

In order to scale this technique to high pulse energy, stretched pulses are required. The delay provided by birefringent crystals is then insufficient, as the stretched pulse durations are typically longer than several tens of picoseconds. As an alternative, free-space delay lines [31, 119] can easily provide delays on a nanosecond scale. Therefore, combinations of HWPs and PBSs can be used, as depicted in Fig. 3.9b. In this case, the relative pulse intensities are set by the orientation angles θ of the HWPs. An initially p-polarized pulse will be rotated by 45° and, hence, equally split on a subsequent idealized PBS for $\theta_1 = 22.5°$ (compare to Fig. 3.5b). While the p-polarized component gets transmitted by both PBSs in a delay line, the s-polarized component is delayed by a free-space path and, finally, reflected along the direction of the previously transmitted pulse. Following the same considerations done for Eq. (3.1), two pulse replicas are generated after the first delay line producing a delay τ_1, given by

$$\mathbf{J}_1(t) = \mathcal{M}_{\mathrm{T}}^2(T_{\mathrm{p}}, R_{\mathrm{s}})\mathcal{M}_{\mathrm{HWP}}(\theta_1)\mathbf{J}_0(t) + \mathcal{M}_{\mathrm{R}}^2(T_{\mathrm{p}}, R_{\mathrm{s}})\mathcal{M}_{\mathrm{HWP}}(\theta_1)\mathbf{J}_0(t - \tau_1), \qquad (3.8)$$

which for further delay lines $k = 2, 3, \ldots, K$ can be iteratively expanded to

$$\mathbf{J}_k(t) = \mathcal{M}_{\mathrm{T}}^2(T_{\mathrm{p}}, R_{\mathrm{s}})\mathcal{M}_{\mathrm{HWP}}(\theta_k)\mathbf{J}_{k-1}(t) + \mathcal{M}_{\mathrm{R}}^2(T_{\mathrm{p}}, R_{\mathrm{s}})\mathcal{M}_{\mathrm{HWP}}(\theta_k)\mathbf{J}_{k-1}(t - \tau_k). \qquad (3.9)$$

An identical sequence of birefringent crystals [120] or free-space delay lines [30] has to

be applied in reverse order to stack the pulse burst again, which is additionally shown in Fig. 3.9. For an efficient stacking, the optical path lengths have to be matched. Passively stable implementations, such as Sagnac loops [30, 121] or double passes [31, 32] (as will be considered in Subsec. 3.2.3), are straightforward techniques free from the requirement on active stabilization (see Chap. 4), since pulses pass identical optical paths and there are no significant amplitude or phase changes among them. In these passive arrangements, however, for the pulse stacking to take place the linear polarization state of the generated pulse burst needs to be rotated by 90°. A Faraday rotator can be employed in case of a double-pass configuration. In this sense, previously non-delayed pulse replicas are delayed and vice-versa. Thus, the final stacked pulse is orthogonally polarized to the initial pulse, which can be easily separated from each other by an additional PBS.

As already indicated in Subsec. 3.1.2, the quality of the PBSs used for temporal combination can be a matter of concern. Therefore, pulse stacking will be considered in more detail, in the following. Within this work, an efficiency parameter is introduced, which is a measure for the quality of the pulse stacking. Moreover, the impact of polarization misalignments will be analyzed.

3.2.2. Pulse-Stacking Efficiency

In this section, the pulse-stacking efficiency and the pulse contrast are introduced as a means to evaluate the pulse-stacking process. Therefore, the requirements on the alignment precision of the HWPs and its impact on the generated pulse burst are discussed. The impact of the quality of the PBSs on the stacking efficiency and the pulse contrast is also considered. In order to obtain an estimate for the theoretical maximum, the amplification of the burst taking place between the pulse division and stacking stages is not taken into account, but it will be discussed in Subsec. 3.2.3.

In contrast to spatial combination, in the temporal case any combination mismatches are not ejected in the form of energy losses, but rather as parasitic side pulses. These parasitic pulses traveling along a wrong path lead to a reduction of the pulse contrast and the efficiency of pulse stacking. Therefore, a temporal pulse-stacking efficiency

$$\eta_{\text{stack}}^{\text{temp}} = \frac{E_{\text{p,main}}}{E_{\text{p,comb}}} \tag{3.10}$$

can be defined, with $E_{\text{p,main}}$ being the pulse energy contained within the main pulse and $E_{\text{p,comb}}$ being the overall combined output pulse energy including parasitic pulses. This efficiency considers only the energy distribution at the system output, but not any losses that occur during pulse stacking or from an additional spatial combination (as will be

introduced in Chap. 5). Thus, using Eq. (3.6) and Eq. (3.10), the total system efficiency is given by

$$\eta_{\text{sys}} = \eta_{\text{sys}}^{\text{spat}} \eta_{\text{stack}}^{\text{temp}}. \tag{3.11}$$

Equation (3.11) constitutes the most practical definition of efficiency for temporal and spatio-temporal implementations. It relates the energy confined in the main pulse after pulse stacking to the overall pulse energy at the output of the amplifier or, even, amplifier array [107].

Additionally, for certain applications the pulse contrast might be of concern. Within this thesis the pulse contrast is considered as the pulse-energy ratio of the main pulse to the strongest parasitic pulse $E_{\text{p,para}}$, i.e. pre- or post-pulse[7,8]:

$$\mathcal{C} = 10 \log_{10} \left(\frac{E_{\text{p,main}}}{E_{\text{p,para}}} \right) \text{dB}. \tag{3.12}$$

Under experimental conditions, intensity variations among the created burst and, consequently, an associated intrinsic combination loss may be unavoidable (largely caused by an imperfect angular alignment of the crystals[9] or the HWPs). In terms of crystals, the angle between the optical axis and the linear polarization of the pulses must be exactly $|\theta| = 45°$ to obtain an equal intensity splitting at each crystal. An alignment accuracy of $\pm\delta\theta$ may impact the splitting ratios and cause intensity variations among the individual pulse replicas of the generated burst. Considering delay lines employing HWP-PBS combinations, the effect is twice as large since the required angle of the HWP is $2|\theta \pm \delta\theta|$, with $|\theta| = 22.5°$ resulting in a rotation of the linear polarization state by $45°$ and, hence, equal intensity splitting at the subsequent PBS. Assuming K delay lines and a variation $\delta\theta$ of the orientation angle (in radians), the intensity ratio between the strongest and the weakest pulse replica is[10]

$$\mathcal{R} = \left[\frac{\cos(2\delta\theta) + \sin(2\delta\theta)}{\cos(2\delta\theta) - \sin(2\delta\theta)} \right]^{2K}. \tag{3.13}$$

---

[7]Particularly, the position of the temporal pre- or post-pulses considered for the pulse contrast is related to the delays provided by the delay lines. This means that the pulse quality of the compressed main pulse is not considered in this definition of pulse contrast. Since, for example, significant side-lobes may arise for $B \gtrsim 3$ rad, the Strehl ratio [56] could be used, too.

[8]Please note that a large number of parasitic pulses being present may have a detrimental impact for particular applications, which is not considered in this definition of the pulse contrast. The overall energy being lost to parasitic pulses at the system output is considered by the stacking efficiency.

[9]Additionally, the crystals might be tilt off the x-y-plane (or differ from non-perfect a-cut) producing a walk-off and a phase difference between orthogonal polarizations. This may also have an impact on the combination efficiency but it has been neglected in this work [118, 122, 123]. Moreover, a difference in dispersion of both optical paths has to be considered for very short pulses [124].

[10]In the case of crystals, $2\delta\theta$ has to be replaced by $\delta\theta$ in Eq. (3.13) [125].

The resulting intensity ratios for the generation of a burst of up to 64 pulse replicas with $K = 1, 2, \ldots, 6$ are shown in Fig. 3.10a, where different angle uncertainties $\delta\theta$ between 0.5° and 2° for each element are assumed. As can be seen from the figure, with an increasing number of pulse divisions care has to be taken for the alignment precision of the HWPs to obtain the desired energy distribution within the burst; in this case equalized pulse energies ($\mathcal{R} = 1$). It has been assumed that $\delta\theta = 1°$ is the practical accuracy, for which the corresponding bursts of four and 32 pulse replicas generated via HWP-PBS combinations (according to Fig. 3.9b) are exemplarily depicted in Fig. 3.10b. Pulse-peak variations are clearly observable with the resulting ratios of $\mathcal{R} \approx 1.3$ and $\mathcal{R} \approx 2$, respectively. Such undesired variations may promote distinct nonlinear phases within a subsequent fiber and, predominantly, have an impact on the final recombination. Thus, for few pulse division stages these are easier to handle whereas for a larger number of division stages a higher precision is required. While for these examples idealized PBSs with $T_{\mathrm{p}} = R_{\mathrm{s}} = 1$ have been assumed, non-idealized PBSs possessing $T_{\mathrm{p}} < R_{\mathrm{s}} < 1$ would further affect these pulse-peak variations and, additionally, distribute pulse energy in unintended polarization components of the individual pulse replicas.

As an example for non-idealized PBSs, a pulse division into four replicas and subsequent stacking in a double-pass setup is illustrated step-wise in Fig. 3.11. In this figure $T_{\mathrm{p}} = 0.97$ and $R_{\mathrm{s}} = 0.99$ have been assumed, which are typical specifications for commercially available high-power PBS cubes [106]. Disregarding the angle uncertainty discussed above, the polarization components being reflected or transmitted into unintended ports of the
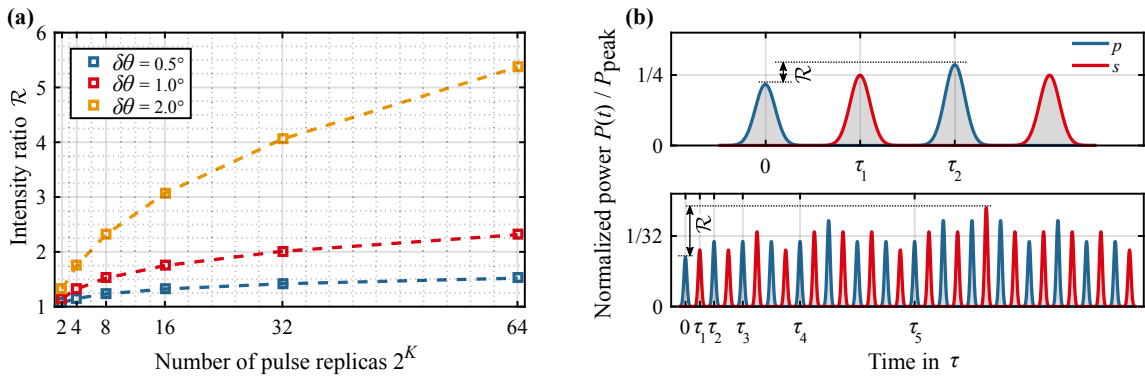

Figure 3.10.: (a) Intensity ratio $\mathcal{R}$ between the strongest and the weakest pulse replica in a burst as a function of the number of generated pulse replicas 2^K (with $K = 1, 2, \ldots, 6$) for angle uncertainties $\delta\theta$ of 0.5°, 1° and 2° (dashed lines are for the guidance of the eye). The bursts are generated with combinations of HWPs and PBSs ($T_{\mathrm{p}} = R_{\mathrm{s}} = 1$) assuming $\theta_k = \theta + \delta\theta = (22.5 + 1)°$ for each kth HWP, where $k = 1, 2, \ldots, K$. (b) Generated bursts of four ($K = 2$) and 32 ($K = 5$) pulse replicas (delay-line lengths in decreasing order). The blue and red lines represent p- and s-polarization, respectively.
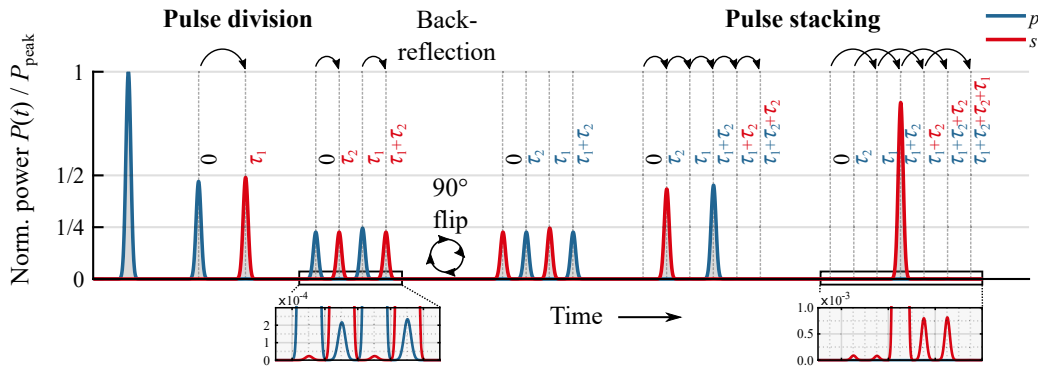
Figure 3.11.: Evolution of the pulse burst generation (delay-line lengths in decreasing order) and stacking for the example of four pulse replicas ($K = 2$) assuming $T_\mathrm{p} = 0.97$ and $R_\mathrm{s} = 0.99$ ($\delta\theta = 0°$). The generated delays τ_k and potential pre- and post-pulse positions are marked by dashed lines.

PBSs during the pulse division lead to slight deviations from the expected s- and p-polarizations, as indicated in Fig. 3.11. This, in turn, results in parasitic pulses during pulse stacking, as indicated below the stacked pulse. There are two reasons for this. First, polarization components of different pulse replicas leak into the wrong optical paths, i.e. parts that need to be delayed are non-delayed and vice-versa. For K delay lines, $2^{K+1} - 1$ time slots are possible with the main pulse being at the 2^Kth position. In Fig. 3.11, these slots, produced by the delays τ_k, are marked by dashed lines. Second, peak-power differences among the individual pulses of the burst result in an imbalance between p- and s-polarization components upon superposition. This translates into deviations from the expected $\pm 45°$ linear-polarization orientation before each HWP (which are required to obtain again p- and s-polarized pulses for the next stacking step). Eventually, while the occurrence of parasitic pulses can be evaluated by the stacking efficiency and the pulse contrast, the overall power loss, related to the reduced peak power of the stacked pulse in Fig. 3.11, is considered by the system efficiency.

The impact of the parameters T_p, R_s and $\delta\theta$ on the pulse stacking can be also simultaneously considered. For this, the intrinsic temporal stacking efficiency and the pulse contrast, according to Eqs. (3.10) and (3.12), can be calculated in a Monte Carlo simulation [126], which gives a statistical average on the achievable values. Considering a pure pulse division and subsequent stacking in a passive double-pass configuration (without amplifier) with again up to $K = 6$ delay lines, 10^5 iterations are carried out for random adjustments of each HWP with $\theta_k = 22.5° \pm \delta\theta$ within $\delta\theta = 1°$ and the Faraday rotator with $\theta = 45° \pm \delta\theta$ for $T_\mathrm{p} = R_\mathrm{s} = 1$ (related to idealized PBSs and similarly to crystals), $T_\mathrm{p} = 0.99$ and $R_\mathrm{s} = 0.999$ (typical for commercially available high-power thin-film polarizers [127]), and $T_\mathrm{p} = 0.97$ and $R_\mathrm{s} = 0.99$. The resulting temporal stacking efficiencies are

on average $\gtrsim 99\%$ for the considered cases and the loss in energy, in this regard, is negligible. However, the pulse contrast is degraded, which can be an important parameter for particular applications. The corresponding intrinsic pulse contrast is shown in Fig. 3.12a with the circles showing the mean values and the error bars the minimum and maximum deviations. In the case of $T_\mathrm{p} = R_\mathrm{s} = 1$ (blue) the theoretically infinite pulse contrast is reduced on average to $\sim 35\mathrm{dB}$ for the number of pulse replicas being considered. For a lower quality of the PBSs it gets more likely reduced to $\sim 30\mathrm{dB}$ for the case of $T_\mathrm{p} = 0.99$ and $R_\mathrm{s} = 0.999$ (orange) and $< 30\mathrm{dB}$ for the case of $T_\mathrm{p} = 0.97$ and $R_\mathrm{s} = 0.99$ (red). While the stacking efficiency and the pulse contrast describe the quality of the stacked pulse, the system efficiency considers the power loss upon pulse stacking. The corresponding intrinsic system efficiency[11], according to Eq. (3.11), for the considered parameters is shown in Fig. 3.12b. As can be seen, the system efficiency is drastically decreased for degrading PBS specifications (T_p and R_s) and for an increasing number of pulses. Thus, high-quality PBSs are preferred in order to improve both the intrinsic pulse contrast and the intrinsic system efficiency. Potentially, the reduction of the pulse contrast can be mitigated by placing high contrast polarizers [128] in the delay lines to reject undesired polarization components. Moreover, this parameter can be further improved by a more precise angle alignment of the HWPs (e.g. $\mathcal{C} \gtrsim 50\mathrm{dB}$ for $\delta\theta \lesssim 0.2°$). However, in terms of burst amplification to high energy, amplifier saturation plays the most critical role when
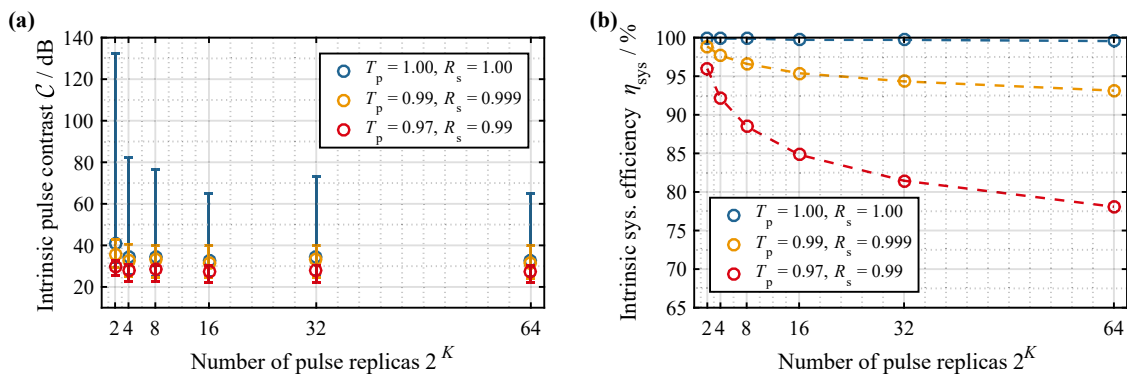

Figure 3.12.: (a) Monte Carlo simulation of the intrinsic pulse contrast $\mathcal{C}$ for 2^K generated pulse replicas (with $K = 1, 2, \ldots, 6$) that are stacked back in a double-pass configuration without amplification. Random settings of all $\theta_k = \theta \pm \delta\theta = (22.5 \pm 1)°$ for each HWP-PBS combination and $\theta = (45 \pm 1)°$ for the Faraday rotator are assumed. The simulation has been done for 10^5 iterations and for different T_p and R_s. The circles represent the mean values and the error bars the minimum and maximum deviations. (b) Corresponding mean system efficiency η_sys (dashed lines are for the guidance of the eye).

---

[11]As the total output energy from an amplifier is used as reference, which typically is placed after pulse division, the total energy of the divided pulses is used as reference, too, which omits losses introduced upon pulse division.

determining the pulse contrast and the system efficiency, as will be investigated in the following.

3.2.3. Amplification of Divided Pulses

As part of this work, the amplification of pulse bursts and its potential impact on their temporal stacking is analyzed in this section. In contrast to the spatial-combination case, the generated pulse replicas are amplified by a single amplifier and any mismatch in their relative peak powers and nonlinear phases can have severe consequences, depending on the type of implementation. In this regard, constraints on passive DPA implementations will be disclosed.

Following Subsec. 2.2.4, there are two extreme operation regimes of an amplifier that can be distinguished: small-signal amplification and amplifier saturation. In the former case, the inversion stays almost constant during amplification and, thus, the overall shape of the burst envelope is not affected by the amplification. Thus, the accumulated nonlinear phase, which depends on the particular fiber and pulse parameters, is almost identical for each pulse replica, which is beneficial for a good stacking efficiency. This phase, described by the B-integral defined in Eq. (2.42), is reduced by the number M of pulses, due to the reduction of the peak power of each individual pulse. Therefore, the total pulse energy can be increased by a factor of M without degrading the pulse quality. This can be attractive especially for systems that are limited by nonlinear effects, such as picosecond fiber lasers [32], for which the stretcher and compressor dimensions required for achieving a comparable stretching ratio with CPA are impractically large due to their limited bandwidth. Although DPA has also been demonstrated for stretcher-free femtosecond fiber-laser systems [32, 121, 129], the pulse energy achieved has just been in the order of a few microjoules. In order to reach a higher pulse energy it might be a better choice to use stretched pulses and DPA. In this sense, the grating size can be kept moderate and the stretched pulse duration can be increased further by the number of pulse replicas. This allows for operation in a deeper saturation regime of the amplifier than that possible with a single stretched pulse and a given amplifier. However, associated to this regime is a deformation of the pulses and the intensity envelope of the burst, as shown in Fig. 2.3a.

In this context, the effect of the amplification on a pulse burst and on the temporal combination is investigated both experimentally and theoretically. In order to do this, femtosecond pulses stretched to 1.3 ns are used, from which a burst of four pulses with a constant intensity envelope is generated. This pulse burst is amplified in an LPF with a core diameter of 81 µm. This experiment is done in the fiber-CPA system, which

will also be employed for the final experiment and which will be described in detail in Subsec. 5.2.4. At a constant average power of $1\,\mathrm{W}$, the seed energy is increased from $4\,\mathrm{\mu J}$ ($f_\mathrm{rep} = 2.1\,\mathrm{MHz}$) to $118\,\mathrm{\mu J}$ ($f_\mathrm{rep} = 76\,\mathrm{kHz}$) in order to increase the extracted energy from the fiber. In Fig. 3.13a the corresponding amplified bursts at different output energy are shown. Due to the time-frequency mapping for large stretching ratios, the pulse shapes in both time and frequency domain are the same. As can be seen, at an output energy of $50\,\mathrm{\mu J}$ the shape of the input burst remains quasi unchanged, which in principle corresponds to the small-signal case for the amplifier. If the energy is increased, the amplifier will start to saturate. Thus, the first pulse replica experiences the highest gain and partially depletes the initial inversion. Consequently, the gain available for subsequent pulse replicas is reduced, which ultimately deforms the overall shape of the burst envelope. This is clearly observable in Fig. 3.13a for increasing burst energy of up to $1.3\,\mathrm{mJ}$. Furthermore, the
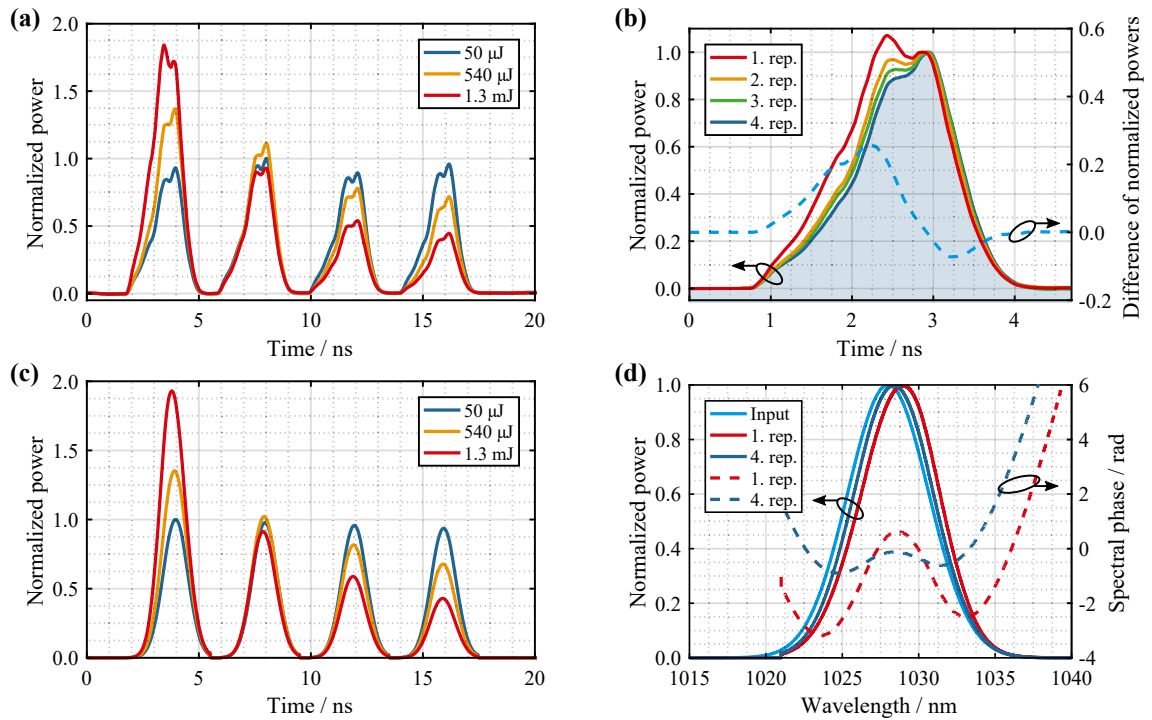

Figure 3.13.: (a) Photo-diode traces (measured with a $< 18\,\mathrm{ps}$ rise-time photo-diode together with a $30\,\mathrm{GS/s}$ sampling oscilloscope) showing pulse bursts comprising four stretched pulse replicas amplified to burst energies of $50\,\mathrm{\mu J}$ (at $f_\mathrm{rep} = 2.1\,\mathrm{MHz}$), $540\,\mathrm{\mu J}$ (at $200\,\mathrm{kHz}$) and $1.3\,\mathrm{mJ}$ (at $76\,\mathrm{kHz}$). The seed power is $1\,\mathrm{W}$ and the peak powers of the pulse replicas in the initial burst are equal. (b) Pulse-shape deformation within the burst of $1.3\,\mathrm{mJ}$. The pulse replicas at the output of the amplifier are laid on top of each other. The difference of the normalized powers between the first and the fourth pulse replica is additionally shown as dashed line. (c) Simulated pulse burst analogously to the measurement. (d) Spectral deformation and residual spectral phase (dashed lines with the corresponding colors) between the first and the fourth pulse replica at $1.3\,\mathrm{mJ}$.

differential gain over the course of the pulse leads, additionally, to a deformation of its shape, as discussed in Subsec. 2.2.3. This effect is illustrated in Fig. 3.13b by laying the individual pulse replicas for the case of 1.3 mJ on top of each other. The front of the pulse experiences higher gain than its tail, effectively tilting the pulse shape towards its front. As a result of the decreasing gain along the burst, this effect is most dominant for the first pulse and weakened for subsequent ones. The difference between the normalized shape of the first and the fourth pulse replica is additionally illustrated in Fig. 3.13b.

Associated to the different amplitude evolution of each pulse replica along the amplifier is a mismatch of their nonlinear phase. In order to study this effect, a numeric model based on the split-step Fourier method, including second-order dispersion, SPM and the Frantz-Nodvik amplification model has been developed using the information given in Sec. 2.2 and Sec. 2.4. Fitting the simulation parameters[12] to the experiment, a good agreement between the simulation and experimental results can be found, which is shown in Fig. 3.13c. With this, the saturation energy[13] has been estimated to be $E_{\text{sat}} = 1\,\text{mJ}$. The pulse-shape deformation affects the spectral shape, which is shown in Fig. 3.13d for the case of 1.3 mJ. Additionally, the residual spectral phase (after compression) for both the first and the fourth pulse replica is depicted. As clearly seen in Eq. (2.40), the different evolution of the pulse amplitudes along the amplifier leads to different nonlinear phases. The B-integral difference between the first and the fourth pulse is $\Delta B = 3.9\,\text{rad}$, which would result in a significant drop in the combination efficiency according to Fig. 3.7b. Moreover, the different pulse-shape deformations get imprinted on the nonlinear phases resulting in additional phase differences between the pulses.

In fact, both pulse amplitude and shape mismatches, as well as nonlinear phase mismatches, will have a detrimental impact on the efficiency of the subsequent pulse stacking, especially for passive implementations [131]. To emphasize this statement, a double-pass DPA scheme, as shown in Fig. 3.14a, will be considered in the following. For this, the simulations are restricted to SPM and the Frantz-Nodvik equations (2.22) and (2.23), as the impact of dispersion is the same for each pulse replica and makes the calculations more involved. To gain a deeper insight about the interplay of saturation and nonlinear phase, a variable maximum B-integral B_{max} is used as a normalization constant, such

---

[12]The main simulation parameters are: $\bar{P}_{\text{s}} = 1\,\text{W}$, $f_{\text{rep}} = 76\,\text{kHz}\ldots2.1\,\text{MHz}$, $\bar{P}_{\text{p}}^{\text{max}} = 250\,\text{W}$ (counter propagation), $\lambda_{\text{s}} = 1028\,\text{nm}$, $\lambda_{\text{p}} = 976\,\text{nm}$, $T_0 = 250\,\text{fs}$ (spectral hard-cut considered), $L = 1\,\text{m}$, MFD = 60 µm, $d_{\text{clad}} = 255\,\text{µm}$, $d_{\text{dop}} = 63\,\text{µm}$, $n_2 = 3.2 \cdot 10^{-20}\,\text{m}^2/\text{W}$, $\beta_2 = 19\,\text{fs}^2/\text{mm}$, $N_{\text{tot}} = 3 \cdot 10^{25}\,\text{m}^{-3}$, $\tau_2 = 800\,\text{µs}$ and the cross-sections shown in Fig. 2.1a.

[13]According to Eq. (2.24) E_{sat} depends on the MFD. The MFD of a fiber with a core diameter of 81 µm is about 78 µm, which shrinks depending on the heat load [130]. Assuming an MFD of 60 µm provides a good agreement between simulation and measurement, for the operation at $\sim 100\,\text{W}$ amplified power. Moreover, E_{sat} corresponds to the average saturation energy weighted by the spectral shape.
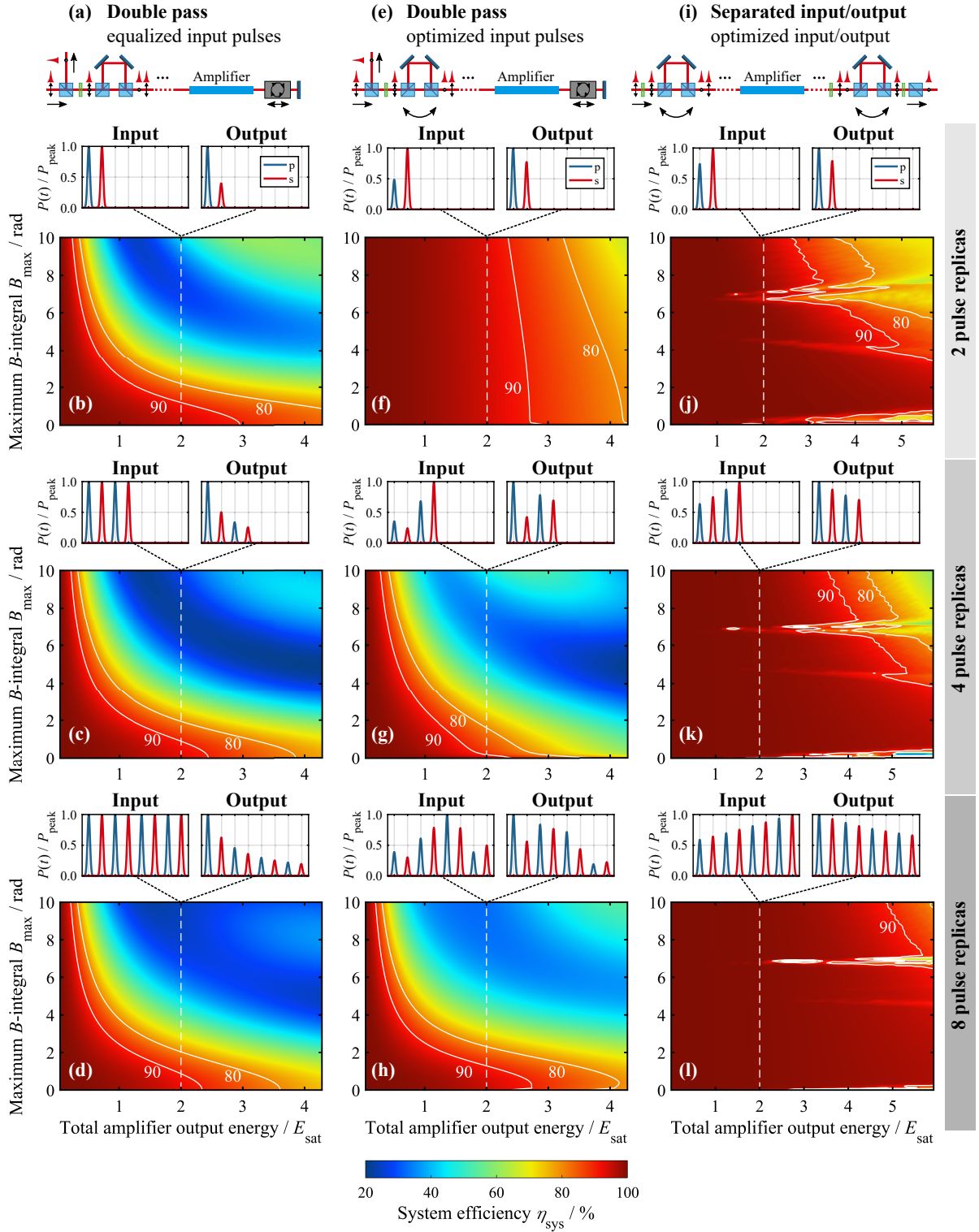
Figure 3.14.: Simulated system efficiency as a function of the maximum B-integral $B_{\max}$ and the total amplified pulse energy normalized to the saturation energy E_{sat} for DPA (a) in a double pass without optimization applying two, four and eight pulse replicas (b)-(d), (e) in a double pass with optimization (f)-(h), and (i) using the optimization of two separated stages for pulse division and stacking (j)-(l). For all $T_{\mathrm{p}} = R_{\mathrm{s}} = 1$ is assumed. Input and output bursts at $2E_{\mathrm{sat}}$ are illustrated above the figures.

that $B(t) = B_{\max}/P_{\text{peak}}(L) \int_0^L |A(z,t)|^2 \mathrm{d}z$, which is the integrated evolution of the burst envelope $|A(z,t)|^2$ normalized to the maximum peak power $P_{\text{peak}}(L)$ at the amplifier output $z = L$. With this, 250 fs pulses stretched to 1.3 ns are divided and amplified[14] in a double-pass amplifier configuration. In forward direction, pulse division is achieved by free-space delay lines with decreasing lengths comprising HWPs and PBSs (see Fig. 3.9b). Pulse stacking is achieved in the backward path using the same delay lines, while a Faraday rotator is used in front of the back-reflecting mirror. In Fig. 3.14b-d the system efficiencies as defined by Eq. (3.11) are shown as functions of both $B_{\max}$ and the total amplified pulse energy for the cases of generating two, four and eight pulse replicas. From the figures it can be inferred that gain saturation and nonlinear phase mismatches become more pronounced at both high pulse energy and high $B_{\max}$. As discussed above, a burst of constant amplitude envelope (generated with the HWPs at angles of $\theta = 22.5°$) gets deformed after amplification. The magnitude of this deformation depends on the saturation level, resulting in different B-integrals for the individual pulse replicas. This, in turn, degrades the system efficiency. As illustration, the input and output bursts are depicted above Fig. 3.14b-d for an output energy of $2E_{\text{sat}}$. In the limiting case of $B_{\max} = 0$ rad, a comparably small efficiency decrease is observable. The residual degradation is due to pulse-amplitude mismatches during the backward pulse stacking, which lead to combination losses at the PBSs caused by deviations from the expected linear-polarization inclination. For $K > 1$ delay lines this is translated into pre- and post-pulses. In the second limiting case, i.e. in the small-signal regime, the burst shape stays almost constant and, thus, the B-integral difference among the pulses is negligible. Hence, high system efficiencies are achievable even for large $B_{\max}$. As the amplifier starts to saturate both the pulse-amplitude and B-integral differences become more pronounced, start degrading and, thus, the system efficiency at higher nonlinearities, which will be shown later on.

The HWPs can be used for optimization in order to find an intermediate orientation between the optima for the forward and backward propagating bursts. Since the B-integral has the most severe impact, an optimization routine is implemented that tries to minimize the B-integral differences between the pulse replicas in the burst. Considering the same double-pass scheme (Fig. 3.14e), but now with the optimization, the resulting system efficiency (again for two, four and eight pulse replicas) is shown in Fig. 3.14f-h. Except for the case of two pulse replicas, no noticeable improvement can be achieved with the optimization. The reason is the limited number of degrees of freedom for the optimization, something that becomes obvious from the pulse bursts above the figures.

---

[14]The changed simulation parameters are: $\bar{P}_\text{s} = 1$ W, f_{rep} is varied in order to obtain a total seed-pulse energy up to 150 µJ, $\bar{P}_\text{p} = 200$ W (counter propagation).

Due to saturation the symmetry of the setup is broken, which cannot be compensated for in both propagation directions. In the special case of two pulse replicas, a trade-off between B-integral matching and pulse-stacking losses due to amplitude mismatches can be found to some extent. However, already at pulse energies in the order of the saturation energy a drop in efficiency is observable making any further scaling difficult.

A solution is to break the symmetry of such a DPA implementation. Therefore, the pulse division has to be separated from the pulse stacking, as depicted in Fig. 3.14i. With this, enough degrees of freedom can be introduced for arbitrary pulse-burst shaping independently from the pulse stacking. For example, this can be realized electronically applying modulators in conjunction with arbitrary waveform generators or optically using the HWPs. Additionally, the HWPs from the pulse stacker can be optimized[15], too. For the simulations a single-pass amplification is assumed while the amplifier is kept the same as in previous simulations. In Fig. 3.14j-l the achieved system efficiency is depicted. Evidently, the efficiency is strongly improved when matching the B-integrals, even at higher pulse energy. The impact of slight nonlinear-phase differences arising from the different pulse-shape deformations seems to be negligible. Moreover, increasing the number of pulse replicas allows for a further scaling of the pulse energy. Please note that in this simulation only the optimization of the B-integrals has been considered. In fact, at high saturation levels and low B-integrals the amplitude mismatch becomes more pronounced than the B-integral mismatch, which is not compensated for by the algorithm and, hence, leads to a much worse efficiency than what would actually be possible (clearly visible in Fig. 3.14j-l bottom right). However, it can be estimated, in the context of a few pulse replicas, that for small B-integrals (in this case $\lesssim 1$ rad) amplitude optimization should be preferred (analogously to the impact of a power mismatch shown in Fig. 3.6c and the B-integral mismatch shown in Fig. 3.7b).

Pulse-amplitude and B-integral differences can degrade both the system efficiency and the pulse contrast. As an example, the pulse contrast $\mathcal{C}$ is shown in Fig. 3.15a as a function of the total amplifier output energy normalized to E_{sat}, considering the case of four pulse replicas for the three scenarios depicted in Fig. 3.14c,g,k (double pass with and without optimization and separated pulse division and stacking with optimization) at $B_{\mathrm{max}} = 5$ rad. For passively stable double-pass implementations the pulse contrast degrades drastically with increasing energy, i.e. amplifier saturation, which cannot be optimized by the HWPs due to the limited degrees of freedom. In contrast, by separating the pulse division from the pulse stacking this situation can be tremendously improved.

---

[15]The optimization includes the variation of the HWPs and a constant compensation phase, as done by an active stabilization (see Chap. 4), for each pulse stacking step.
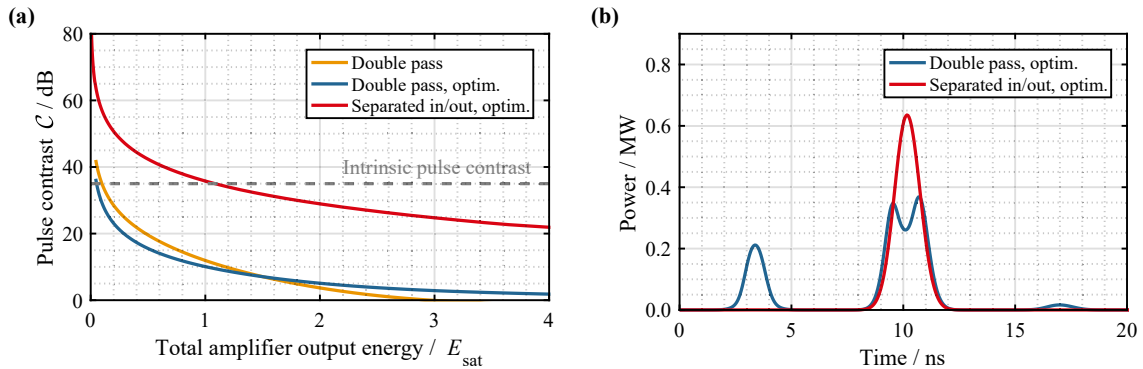
Figure 3.15.: (a) Pulse contrast $\mathcal{C}$ as a function of the total amplified pulse energy normalized to the saturation energy E_{sat} for a maximum B-integral $B_{\mathrm{max}} = 5\,\mathrm{rad}$ and using four pulse replicas for DPA in a double pass with (blue) and without (orange) optimization. Additionally, the results using the optimization of two separated stages for pulse division and stacking (red) are also shown. In all cases $T_{\mathrm{p}} = R_{\mathrm{s}} = 1$ is assumed. The intrinsic pulse contrast (see Subsec. 3.2.2) is shown as grey dashed line. (b) Stacked pulses (uncompressed) for both cases using the optimization at an amplified energy of $2E_{\mathrm{sat}}$.

Therefore, a pulse contrast of $\gtrsim 25\mathrm{dB}$ can be achieved at high pulse energy, which can be further improved with additional pulse-division steps. Please note that these are best case estimates and no uncertainty on the HWP orientation is considered, as for the intrinsic pulse contrast ($\sim 35\mathrm{dB}$, grey dashed line in Fig. 3.15a) from Subsec. 3.2.2. As an example, the corresponding (uncompressed) stacked pulses for both optimized cases are shown in Fig. 3.15b at an energy of $2E_{\mathrm{sat}}$. Besides the deformation of the main pulse, strong pre- and post-pulses occur for the double-pass case. This can be drastically improved by shaping the burst-amplitude envelope in order to match the nonlinear phases of the individual pulse replicas, which is possible by separating the pulse division stage from the stacking stage.

As it has been shown in this section, the amplification of divided pulses can have a negative impact on the intrinsic pulse contrast (see Subsec. 3.2.2). With the separation of the pulse division and the pulse stacking stages, the pulse contrast can be strongly improved in comparison to passively stable (double-pass) implementations. In fact, the achievable contrast is good enough for most applications (e.g. high harmonic generation [8]). However, there are other applications, such as laser-particle acceleration [12], which have even higher requirements on the pulse contrast. For these advanced applications further contrast-improving concepts need to be applied, which should be taken into account for future investigations. Examples of such concepts could potentially be a peak-power-sensitive process, such as nonlinear pulse compression [132] in which the peak power of the main pulse can be tremendously increased compared to that of the parasitic pulses, or a plasma mirror [133].

3.3. State of the Art

In the last decade, there has been a very fast development of the mentioned combining approaches. The experimental demonstrations of actively-stabilized spatial combination schemes and passive DPA applied to femtosecond Yb-doped fiber-laser systems are summarized in Fig. 3.16 in terms of pulse energy and average power. These are results that have been demonstrated both before the beginning and during the duration of this thesis. Since the beginning of this work, the highest pulse energy demonstrated has been 5.7 mJ (corresponding to a peak power of 22 GW) at an average power of 230 W [136]. This demonstration used the spatial combination of four LPFs with a core diameter of 90 μm. Recently, the average power could be further scaled to 1 kW with a pulse energy of 1 mJ, using the spatial combination of eight LPFs with a core diameter of 81 μm [137]. The author of this thesis has been also actively involved in the experiments leading to those results. Recently, DPA of two pulse replicas in a passive Sagnac-type implementation, comprising two large-mode-area fibers with MFDs of 60 μm, allowed for a pulse energy of 1.1 mJ at an average power of 55 W [138]. The results stemming from this work are marked as enlarged solid symbols. Thus, a pulse energy of 12 mJ with an average power of 700 W has been achieved. This is a record for ultrafast fiber lasers, obtained by merging the spatial and temporal combination approaches in a scalable architecture.

In the scope of this work, both the spatial and the temporal combination concepts are used in conjunction with an active-stabilization loop to ensure stable long-term operation. The stabilization techniques applied will be briefly explained in the following chapter.
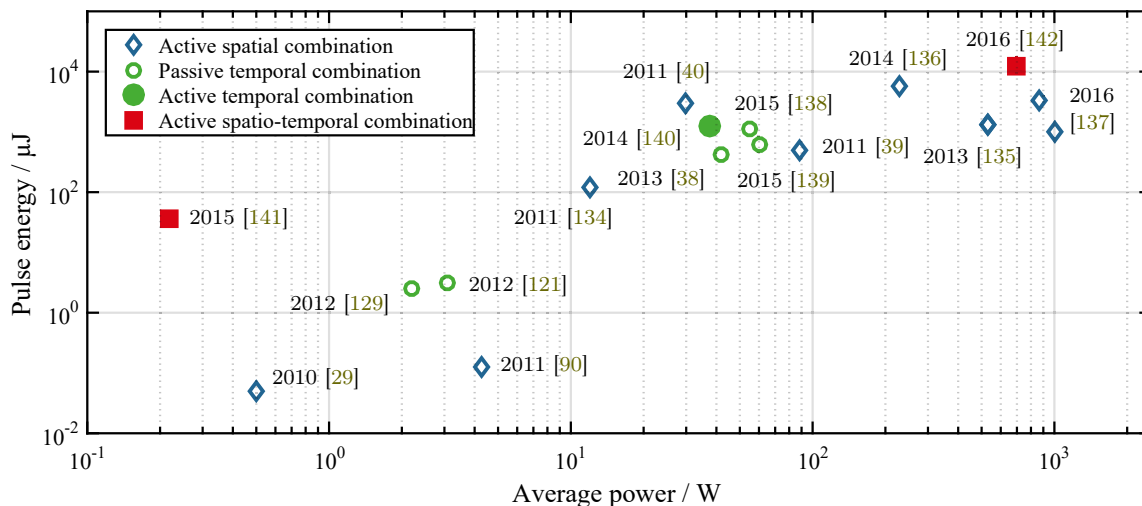

Figure 3.16.: Pulse-energy and average-power demonstrations of actively-stabilized spatial combination (blue diamonds), passively-stabilized temporal combination (green circles), actively-stabilized temporal combination (green solid circle) and actively-stabilized spatio-temporal combination (red solid square) of femtosecond Yb-doped fiber-laser systems over the last decade. The results obtained during this thesis are shown as enlarged symbols.

4. Phase-Stabilization Techniques

Coherent combination is a promising power-scaling technique, as it was explained in the previous chapter. In general, each pair of beams being generated and recombined, for example within an amplifier array, can be thought of as an interferometer. Thus, the relative optical phases of these beams are sensitive against environmental perturbations (such as atmospheric turbulences, mechanical vibrations and thermal drifts in the laser system) and need to be controlled in order to ensure constructive superposition.

In Sec. 3.1, the impact of a delay as a result of an optical path-length mismatch for the superposition of ultrashort pulses was investigated. The optical path-length difference can be aligned on a micrometer scale, in a first order approximation, but actually it needs to be optimized on a sub-wavelength scale to match the carrier oscillations (compare to Fig. 3.7a). This can be achieved with passively stable implementations, such as Sagnac loops. They provide intrinsically matched optical paths as the beam paths are identical (with the beams simply counter-propagating through them). However, these setups are not easily scalable to large channel-counts in spatial combination and have too few degrees of freedom for the temporal combination to operate efficiently in the saturated amplifier regime (e.g. in a double-pass implementation as a special case of a Sagnac loop). Hence, another scalable interferometer architecture is required. A common choice are cascaded Mach-Zehnder-type interferometers that can be realized in tree- or bus-type implementations (see Fig. 3.3) and have to be actively phase-locked.

Active phase-stabilization techniques are, in principle, based on phase-difference detection. From this phase difference, an error signal can be retrieved which is then fed back to a phase-shifting element. Such elements can be piezo actuators with mirrors attached to them (e.g. [29]), acousto-optic modulators (AOMs, e.g. [143]) or electro-optic modulators (EOMs, e.g. [144]). The choice of the phase-shifting element depends on the amplitude and frequency range of the perturbations. Previous investigations in laboratory conditions demonstrated that the phase noise that needs to be compensated extends only to the lower kilohertz range [91]. Prominent phase detection techniques are heterodyne detection [87, 91, 144], Hänsch-Couillaud (HC) [145], Locking of Optical Coherence by Single-detector Electronic-frequency Tagging (LOCSET) [146] and Stochastic Parallel

Gradient Descent (SPGD) [147]. In the following, the active stabilization techniques used in the experiments in this work are explained.

4.1. Hänsch-Couillaud Method

The Hänsch-Couillaud (HC) method was developed for locking the frequency of an oscillator to a reference cavity by measuring the state of polarization of their superposed outputs [145]. This phase-sensitive measurement can be applied to polarization-based spatial-combination implementations. A phase difference between orthogonally-polarized superposed beams changes the resulting polarization state and, thus, the ratio between the transmitted and reflected power at a subsequent PBS (Subsec. 3.1.2). Hence, HC detection can be employed to stabilize the superposition by measuring the polarization state [29].

As an example, a general amplifier array in a bus-type spatial combination scheme is depicted in Fig. 4.1a. In order to explain the working principle of an HC detector, only the first two amplifier channels are considered. A small power fraction, directly after superposing the beams of those two amplifiers, is sent to the HC_1 detector, comprising a QWP, a PBS and two photo-diodes. The QWP is set to $\theta = 45°$ with respect to the p-polarization axis introducing a fixed phase difference of $\pm\pi/2$ between the orthogonal components of the superposed fields projected to the axis of the QWP. These are split at the subsequent PBS and separately detected by their respective photo-diode. Assuming the field $\mathbf{J} = A_\mathrm{p}\hat{\mathbf{p}} + A_\mathrm{s}\hat{\mathbf{s}}$ is a superposition from the two channels, and using the Jones
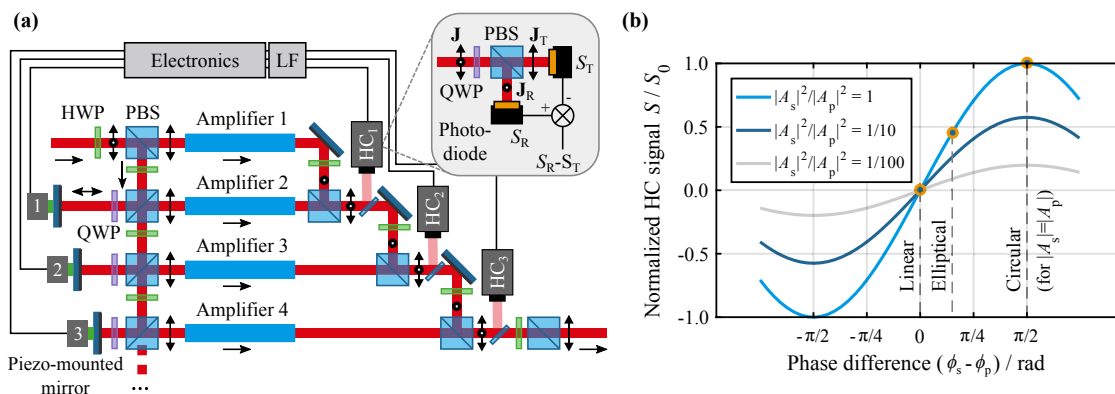

Figure 4.1.: (a) Schematic of an HC stabilization setup for an amplifier array in a bus-type spatial combination scheme (LF: low-pass filtering at the input of the stabilization electronics, PBS: polarizing beam splitter, HWP: half-wave plate, QWP: quarter-wave plate). (b) Normalized HC signal S/S_0 (with the total signal being $S_0 = S_\mathrm{T} + S_\mathrm{R}$) as a function of the phase difference $\phi_\mathrm{s} - \phi_\mathrm{p}$ between both orthogonal polarization components for different power ratios $|A_\mathrm{s}|^2/|A_\mathrm{p}|^2$.

matrices from Tab. 2.1, the fields measured by each photo-diode are

$$\left.\begin{array}{l} S_{\mathrm{T}} \sim |\mathcal{M}_{\mathrm{T}}\mathcal{M}_{\mathrm{QWP}}(\theta)\mathbf{J}|^2 = \dfrac{|A_{\mathrm{s}}|^2}{2} + \dfrac{|A_{\mathrm{p}}|^2}{2} - |A_{\mathrm{s}}||A_{\mathrm{p}}|\sin(\phi_{\mathrm{s}} - \phi_{\mathrm{p}}), \\[2mm] S_{\mathrm{R}} \sim |\mathcal{M}_{\mathrm{R}}\mathcal{M}_{\mathrm{QWP}}(\theta)\mathbf{J}|^2 = \dfrac{|A_{\mathrm{s}}|^2}{2} + \dfrac{|A_{\mathrm{p}}|^2}{2} + |A_{\mathrm{s}}||A_{\mathrm{p}}|\sin(\phi_{\mathrm{s}} - \phi_{\mathrm{p}}), \end{array}\right\} \tag{4.1}$$

with the complex amplitudes A_{p} and A_{s} defined according to Eq. (2.32). The HC signal S is related to the signal difference $S_{\mathrm{R}} - S_{\mathrm{T}}$, obtained by electronic subtraction, which results in

$$S \sim 2|A_{\mathrm{s}}||A_{\mathrm{p}}|\sin(\phi_{\mathrm{s}} - \phi_{\mathrm{p}}). \tag{4.2}$$

This signal is shown normalized to the total signal $S_0 = S_{\mathrm{T}} + S_{\mathrm{R}}$ in Fig. 4.1b. The HC signal is zero for linear polarization (inclined by 45° for $|A_{\mathrm{s}}| = |A_{\mathrm{p}}|$) of the combined beam. Any phase change (within $\pm\pi/2$) leads to a non-zero error signal for elliptic polarization which reaches its maximum for circular polarization. The sign of the error signal depends on the direction of the phase shift, which can be used for correction at the phase shifters shown in Fig. 4.1a. The feedback-system will operate at a zero error signal, which corresponds to a local optimum of the superposition of the carrier oscillations. However, phase differences that are multiples of 2π cause a shift of the pulse envelope, according to Fig. 3.7a, which decreases the combination efficiency and the signal-to-noise ratio of the HC signal.

In principle, the regulation bandwidth of the HC technique is only limited by the laser repetition rate. Thus, it can be scaled to multiple channels without bandwidth-constraints using multiple HC detectors. According to Fig. 4.1a, for N amplifier channels $N-1$ HC detectors are required. In a cascaded stabilization setup, the response of any subsequent HC detector is influenced by the previous ones. For bus-type arrays, the HC signal of the mth detector is

$$S_m \sim 2\sum_{j=1}^{m} |A_{m+1}||A_j|\sin(\phi_{m+1} - \phi_j), \tag{4.3}$$

with $|A_{m+1}|$ and ϕ_{m+1} being the amplitude and phase of the $(m+1)$th channel (for $m = 1, 2, \ldots, N-1$) that is orthogonally superposed to the already combined channels $j = 1, 2, \ldots, m$ with amplitude $|A_j|$ and phase ϕ_j. The error signal from the detectors further downstream the optical path is influenced by phase errors in previous combination steps.

Furthermore, for a strong HC signal a well-balanced power ratio between both photo-diodes and, thus, the amplifier channels is beneficial, such that $|A_{\mathrm{s}}|^2/|A_{\mathrm{p}}|^2 = 1$. This condition is always fulfilled in tree-type arrays but it is only met for the first combination step

in bus-type arrays. Here, the power ratio between the superposed beams changes at each subsequent combination step to $1/m$. Hence, according to Eqs. (4.1) and (4.3) the ratio between the strength of the error signal and the DC component $\max(S)/S_0 = 2\sqrt{m}/(1+m)$ decreases the signal-to-noise ratio of the HC signal at the respective step. This is illustrated in Fig. 4.1b for the ratios $|A_{\mathrm{s}}|^2/|A_{\mathrm{p}}|^2 = 1$, $1/10$ and $1/100$. Depending on the sensitivity of the electronics, the stabilization of hundred channels per bus is still feasible.

4.2. LOCSET Method

LOCSET [146] is a phase-stabilization method for amplifier arrays requiring only a single detector at the system output, as illustrated in Fig. 4.2a. Based on a dithering and coherent demodulation technique using distinct RF modulation frequencies, independent error signals can be determined from the beat notes caused by the interference between all the individual beams on the photo-detector. LOCSET is referred to as a self-synchronous configuration when all channels are modulated and as a self-referenced configuration when one channel acts as an unmodulated reference.

The error-signal generation can be described analytically for the most general case of self-synchronous LOCSET [146]. Using the notation from Eq. (2.7) and Eq. (2.32), the modulated real electric field $\mathcal{E}_m(t)$ of the mth amplifier (all the amplifiers emit radiation
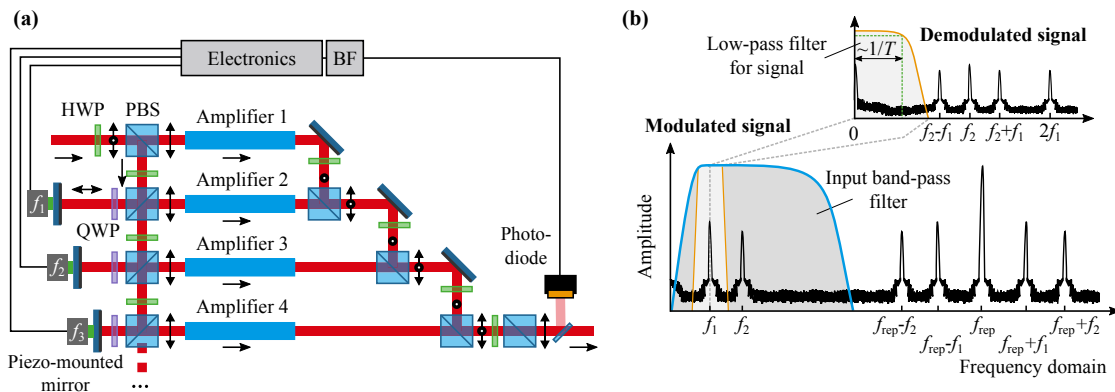

Figure 4.2.: (a) Schematic of a LOCSET stabilization setup for an amplifier array in a bus-type spatial combination scheme (BF: band-pass filtering at the input of the stabilization electronics, PBS: polarizing beam splitter, HWP: half-wave plate, QWP: quarter-wave plate). (b) Cartoon of the modulation (with the modulation frequencies f_1 and f_2 as well as the band-pass filtering at the input shown in blue) and coherent demodulation showing the generated side-bands up to the first harmonic of the laser repetition rate f_{rep}. The low-pass filtering for the demodulation at f_1 is also shown in orange.

that is identically polarized and spatially uniform) can be expressed as

$$\mathcal{E}_m(t) = \frac{1}{2}\Re\left\{|A_m(t)|\exp\left[i(\phi_m + \beta_m\sin(2\pi f_m t))\right]\right\}, \tag{4.4}$$

with $|A_m(t)|$ and ϕ_m being the complex amplitude and phase, respectively, and f_m and β_m being the RF modulation frequency and modulation depth of the mth amplifier channel. The intensity on the photo-detector from all N superposed fields is

$$I(t) \sim \frac{1}{2}\left\{\left[\sum_{l=1}^{N}\mathcal{E}_l(t)\right]\cdot\left[\sum_{j=1}^{N}\mathcal{E}_j^*(t)\right] + c.c.\right\}, \tag{4.5}$$

with l and j being the summation indices for the N phase-modulated channels. From Eq. (4.5) the mth error signal S_m expected when demodulating with the respective RF modulation frequency f_m and after an integrating low-pass filter can be deduced:

$$S_m \sim \frac{1}{T}\int_0^T I(t)\sin(2\pi f_m t)\mathrm{d}t. \tag{4.6}$$

The integration time should be chosen to be sufficiently long to isolate the individual modulation signals and mitigate cross-talk between them ($T \gg 1/|f_m - f_{j\neq m}|$) but, at the same time, it should be short compared to the time scale of the fluctuations to be canceled. This becomes clear in frequency domain, which is illustrated in Fig. 4.2b for the example of two modulation frequencies f_1 and f_2 that appear as side-bands around the laser repetition rate[1] f_{rep}. The phase changes to be detected are within a frequency band around f_1 and f_2, which is typically band-pass filtered at the input of the stabilization electronics. After demodulation at the respective frequency, for example f_1, new components are generated at $f \pm f_1$. The newly created baseband includes the desired phase information, which is low-pass filtered by integrating the signal with time T. This corresponds to a filter bandwidth proportional to $1/T$. On the one hand, if the integration time is too short, frequency components of the $f_2 - f_1$ (or $2f_1$) peak will be within the filter bandwidth distorting the error signal. On the other hand, if the integration time is too long, only slow phase changes within the f_1 band will be detected. Hence, the spacing between two adjacent modulation frequencies should be larger than twice the bandwidth to be regulated.

The contributions from all undesired dither frequencies to the error signal will be significantly smaller than the desired ones, if the above mentioned integration-time condition

---

[1]In this example, only frequencies up to the first harmonic are considered.

is met. Applying it to Eq. (4.6), the error signal can be approximated by [146, 148]

$$S_m \sim \sqrt{I_m} J_1(\beta_m) \sum_{\substack{j=1 \\ j \neq m}}^{N} \sqrt{I_j} J_0(\beta_j) \sin(\phi_j - \phi_m), \tag{4.7}$$

with J_n being the Bessel function of the first kind and nth order. Equation (4.7) resembles the weighted phase difference of the mth channel to the mean phase of the ensemble of all channels. As in the HC technique, the sign of the error signal corresponds to the direction of the phase change, which is minimized to zero in the feedback-loop.

The signal strength depends on the modulation depth and the intensities from the amplifier channels on the photo-detector. The magnitude of β_m constitutes a trade-off between sufficient signal-to-noise ratio supporting stable operation and degradation of the combination efficiency [149]. For the experiments herein, self-referenced LOCSET is applied as special case of Eq. (4.7), with one channel being unmodulated, i.e. $\beta_0 = 0$.

The combination of N channels requires $N-1$ different modulation frequencies, which are significantly lower than the laser repetition rate. This reduces the achievable regulation bandwidth. Additionally, the phase modulators have a maximum supported bandwidth, which needs to be taken into account. In this regard, a single frequency dithering method based on time division multiplexing has been suggested [150]. However, this technique encounters similar restrictions in the number of time slots that can be allocated in the time domain as in the number of frequencies that can be addressed in the frequency domain. For very large amplification arrays, a cascaded implementation of LOCSET using more than one photo-detector for channel groups can be applied [151], reducing the number of modulation frequencies needed.

In summary, the HC method exhibits the advantage over LOCSET of being scalable without losing regulation bandwidth. On the other hand, LOCSET provides a simpler setup and does not require any defined polarization properties. In the experiments, the HC method is applied for polarization-based spatial combination. Unfortunately, it cannot be applied in its classical form for temporal combination based on actively-controlled DPA. Therefore, LOCSET is used in this respect, which will become clear in the following chapter.

5. Spatio-Temporal Combination of Ultrashort Pulses

In the previous chapters the fundamentals for both spatial and temporal combination as power-scaling concepts for ultrafast fiber-laser systems were worked out and their specific requirements were discussed. Moreover, the current state of the art of laser systems based on these concepts was reviewed. In this chapter, an actively stabilized spatio-temporal combination scheme will be experimentally demonstrated for the first time. First, the principle of the actively controlled divided-pulse amplification concept and its experimental demonstration will be described. Second, this concept will be applied as an extension to the spatial combination approach and both its feasibility and the requirements for its realization are investigated. Finally, a high-power laser system achieving 12 mJ of pulse energy with 700 W of average power, corresponding to a record performance for ultrafast fiber-based laser systems, will be presented.

5.1. Active Divided-Pulse Amplification

5.1.1. Principle

The concept of divided-pulse amplification was introduced in Sec. 3.2. It was shown that the symmetry requirements of passively stable Sagnac-type implementations hinder their use for high-energy applications. Therefore, in order to obtain a full control over the pulse-burst shape, the generation of the burst has to be separated from its stacking. This has the advantage that saturation effects from the amplifier can be counteracted. Due to the necessity of an active stabilization to ensure stable pulse stacking, this technique is referred to as active divided-pulse amplification (aDPA) [140].

A schematic of the aDPA implementation is depicted in Fig. 5.1. The pulse division and stacking is done using free-space delay lines, which comprise combinations of HWPs and PBSs, and it follows the same procedure described in Subsec. 3.2.1. Here, a double pass through a single PBS is used both for compactness and for obtaining perpendicular
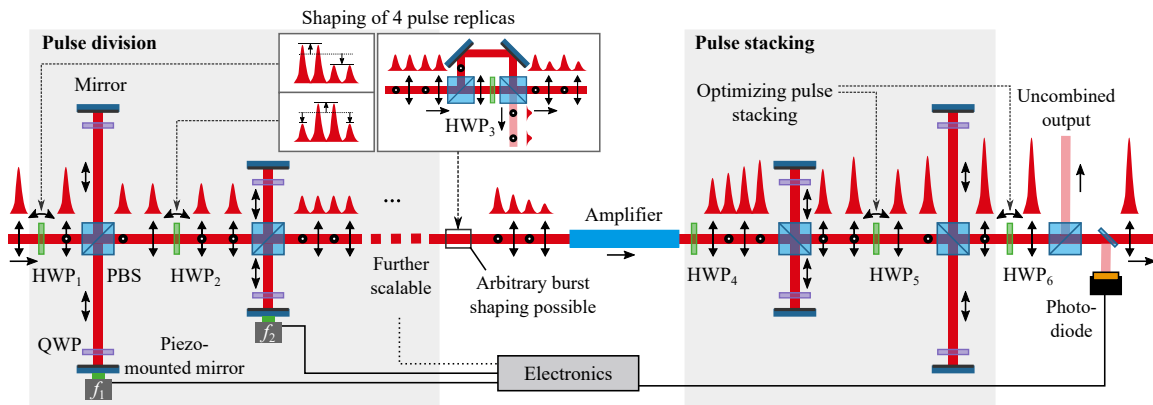
Figure 5.1.: Schematic of the aDPA implementation showing the pulse burst generation and shaping of up to four pulse replicas before amplification and pulse burst stacking afterwards.

incidence on a piezo-mounted mirror employed to achieve optical-path matching. More specifically, the delay line is divided in two parts each containing a QWP which rotates the linear polarization state by 90° after passing through it twice. Hence, the p-polarized component is directly transmitted through the PBS, while the s-polarized component goes through the delay line and then it is reflected at the PBS in the same direction as the initially transmitted p-component. The delay lines decrease in length, resulting in an alternating pattern of orthogonal polarizations in the pulse burst. Their lengths should be appropriately chosen to ensure a complete separation of the pulse replicas. Since this is also the configuration used in the experiments, the generation of four pulse replicas using two delay lines is illustrated in Fig. 5.1. However, this can be easily extended using further delay lines, as indicated by the dotted beam part. After amplification, the generated burst is stacked back to a single pulse on a setup as that used for pulse division (but in reverse order).

In contrast to passive DPA implementations, the most important difference is that the HWP orientation angles can be modified independently in both the pulse division and the pulse stacking stages, providing more degrees of freedom. In this context, to arbitrarily shape the relative amplitudes of a burst of four pulse replicas, three degrees of freedom are necessary. For the example depicted Fig. 5.1, both HWP$_1$ and HWP$_2$ can be used to alter the power balance between the pulses. The resulting response to the burst is shown as an inset in Fig. 5.1. A further degree of freedom is obtained by inserting another small delay line, also shown in the inset, which controls the attenuation of all p-polarized pulses by using HWP$_3$. It is worth noting that this kind of shaping setup provides an instantaneous response, which is advantageous for investigations, and works well for four pulse replicas. However, it becomes challenging for an increasing number K of delay lines, since the binary pulse division generates 2^K pulses, but provides intrinsically only K degrees of

freedom. In this respect, a further scaling seems more feasible by using an electronically controlled burst shaping, by applying, for example, acousto-optic modulators. Finally, the pulse stacking can also be optimized using HWP_5 and HWP_6. Note that HWP_4 needs to be fixed at $\theta = 45°$ in order to rotate the polarization of the burst by $90°$.

Due to the separation of the stages for pulse division and stacking, the delay lines need to be matched and be actively stabilized, in order to compensate for any perturbations. In Chap. 4, both the HC technique and the LOCSET technique were introduced. The first one, in its classical configuration, cannot be applied to polarization-based temporal combination schemes, since the orthogonal polarizations of subsequent pulses lead to a vanishing HC signal. Thus, LOCSET will be applied in the following, since it has the advantage of maximizing the power measured at the system output (after pulse stacking). The path length of each individual delay line is independently optimized using piezo-mounted mirrors placed within the delay lines used for pulse division. Due to the distinct RF modulation frequencies, applied to the dither of each path, they can be addressed for phase correction in the feedback system. Therefore, a small power fraction at the output is sent to a photo-diode. In the following, the results of the first experimental demonstration of aDPA are presented and discussed.

5.1.2. Experimental Demonstration

Setup

The feasibility of aDPA is demonstrated in a first proof-of-principle experiment applying it to an already existing state-of-the-art fiber-CPA system, which is depicted in Fig. 5.2. As seed source, a commercially available 40 MHz bulk mode-locked oscillator is employed. It delivers 300 fs pulses at a central wavelength of 1028 nm (6 nm bandwidth) with an average power of 150 mW. These pulses are stretched to a duration of about 2 ns in an Offner-type stretcher [152] employing a 35 cm wide dielectric grating with 1740 lines/mm and a diffraction efficiency of about 90%. Two roof prisms displace the beam twice allowing for two passes through the stretcher, resulting in eight passes on the grating. The stretcher supports a total spectral width (hard-cut) of 7.5 nm, with the path difference between the shortest and the longest wavelength corresponding to a temporal spread of 4.2 ns [53]. In order to keep the system dimensions moderate, the stretcher and the final compressor share the same grating. The final compressed pulse duration can be optimized by slightly detuning the stretched pulse duration using a motorized mini-compressor placed right after the stretcher, to avoid any movement of the large compressor gratings.

Afterwards, a clock signal is extracted from the beam, in order to trigger the acousto-

optic modulators (AOMs) in the system. To ultimately increase the pulse energy, the repetition rate is reduced to 1 MHz by a first fiber-coupled AOM. It is followed by a core-pumped 1 m long 6 μm-core Yb-doped step-index fiber (SIF), where the optical signal is amplified to 300 mW. Throughout the system, optical isolators are placed between the amplifiers to suppress any feedback. A phase-shaper, consisting of a spatial-light modulator (SLM) with 128 pixels, is employed to pre-compensate the nonlinear terms of the spectral phase accumulated in the system due to, for example, SPM or higher-order dispersion terms. The phase to be compensated is retrieved using a multiphoton intrapulse interference phase scan (MIIPS) device [153], which measures the second-harmonic spectrum at the output of the compressor. Since the SLM setup introduces about 50% losses, another amplifier is employed. It comprises a counter-propagating pumped large-pitch fiber (LPF) with a core diameter of 63 μm and a length of 80 cm, fixed in a water-cooled aluminum module. Angle-polished end-caps are spliced on both sides of each LPF to protect the facets and to avoid feedback. The fiber-coupled pump diodes employed in the system operate at 976 nm. A second AOM sets the final desired repetition rate. Both AOMs in the system are synchronized to the clock signal with the help of electronic pulse-pickers. The last component of the front-end system is another water-cooled amplifier module comprising a counter-propagating pumped 90 μm-core LPF with a length of 80 cm, used to provide sufficient seed for the main amplifier.

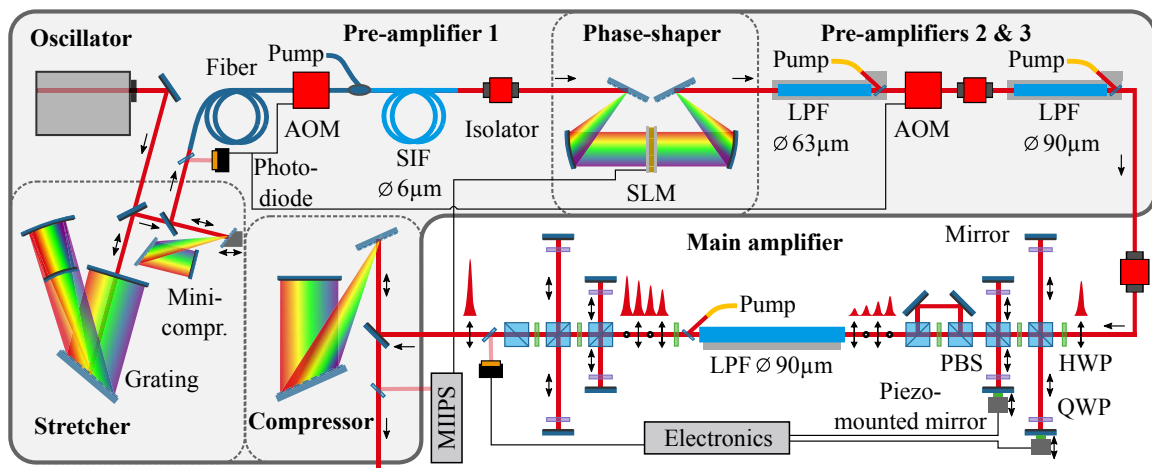Finally, for the main amplification stage the aDPA technique is applied, as described in

Figure 5.2.: Experimental setup consisting of an oscillator, a stretcher and a compressor, acousto-optic modulators (AOMs), a phase-shaper with a spatial-light modulator (SLM), three pre-amplifiers and the main amplifier (SIF: step-index fiber, LPF: large-pitch fiber) as well as the temporal pulse division and stacking stages. The red lines denote free-space propagation, the blue lines denote propagation in fibers (light blue corresponds to Yb-doped fibers) and the black lines are electronic connections. The grey box represents the part of the setup placed in a housing.

detail in Subsec. 5.1.1. The lengths of the first and second delay lines are 3.7 m and 2.2 m, respectively, corresponding to temporal delays of 12.3 ns and 7.3 ns. A single stretched pulse or a burst of two or four pulses can be generated depending on the settings of the HWPs. In the delay lines, PBS cubes specified with $T_{\mathrm{p}} > 0.97$ and $R_{\mathrm{s}} > 0.99$ are applied. The main amplifier is a 90 µm-core LPF with a length of 1.1 m. It possesses an air-clad diameter of 280 µm and is pumped in the counter-propagating direction with a 200 µm fiber-coupled pump diode providing up to 200 W of average power at 976 nm. After amplification, the pulses are stacked back to a single pulse, which is ultimately compressed in a Treacy-type grating compressor [154].

Experiment

In order to demonstrate the potential of the pulse division approach, the seed pulse energy is set to 500 µJ at a repetition rate of 10 kHz, which is launched into the pulse divider to generate a burst of four pulses. Shaping it iteratively in order to keep the peak powers of the amplified pulses equal after amplification even when increasing the pump power, an overall energy of 6.5 mJ could be achieved at the fiber output[1], which illustrates the energy-scaling capability of DPA. This value was limited by the available pump power for the chosen repetition rate[2]. Please note that this experiment was aimed solely at demonstrating the ability to overcome the damage threshold of the fiber when using the amplification of divided pulses and not at maximizing the combination efficiency. The shaped input burst and the corresponding amplified output burst are depicted in Fig. 5.3. It is worth noting that a non-divided pulse at this energy would instantaneously damage the fiber. According to Eq. (2.30), the energy-damage threshold can be estimated to be 3.4 mJ (assuming an MFD of 75 µm and 5 mm thick end-caps; without end-caps it is 1.4 mJ). In this experiment, damage is prevented by the temporal distribution of the energy over 22 ns corresponding to an effective stretched pulse duration of $4 \cdot 2\,\mathrm{ns} = 8\,\mathrm{ns}$, with approximately 1.6 mJ contained in each pulse replica after amplification. In this regard it has recently been verified that the damage threshold (according to Eq. (2.30)) for M times the (stretched) pulse duration (T_0) scales accordingly for M pulse divisions ($E_{\mathrm{dam}} \sim \sqrt{T_0} \sim \sqrt{M}$) [155]. Using a split-step Fourier simulation tool[3] based on the

---

[1]The theoretical maximum extractable energy in this experiment is estimated to be $\sim 10\,\mathrm{mJ}$ according to Eq. (2.28), with a saturation energy of $E_{\mathrm{sat}} = 1.3\,\mathrm{mJ}$.

[2]The repetition rate was not decreased further to keep ASE negligible.

[3]The main simulation parameters are: $\bar{P}_{\mathrm{s}} = 2\,\mathrm{W}$, $f_{\mathrm{rep}} = 10\,\mathrm{kHz}$, $\bar{P}_{\mathrm{p}} = 100\,\mathrm{W}$ (counter propagation), $\lambda_{\mathrm{s}} = 1028\,\mathrm{nm}$, $T_0 = 200\,\mathrm{fs}$ (spectral hard-cut considered), $\lambda_{\mathrm{p}} = 976\,\mathrm{nm}$, $L = 1.1\,\mathrm{m}$, MFD = 75 µm, $d_{\mathrm{clad}} = 280\,\mathrm{µm}$, $d_{\mathrm{dop}} = 70\,\mathrm{µm}$, $n_2 = 3.2 \cdot 10^{-20}\,\mathrm{m^2/W}$, $\beta_2 = 19\,\mathrm{fs^2/mm}$, $N_{\mathrm{tot}} = 3 \cdot 10^{25}\,\mathrm{m^{-3}}$, $\tau_2 = 800\,\mathrm{µs}$ and the cross-sections shown in Fig. 2.1a. Here, the seed power, the pump power and the MFD were matched in order to fit the burst shape and the output energy.
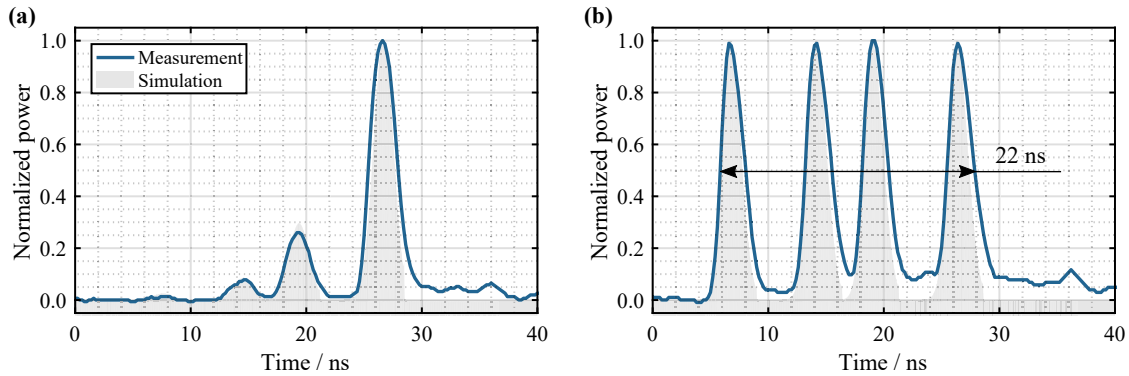
Figure 5.3.: Simulated and measured (with a 1-ns-rise-time photo-diode) amplification of a burst of four pulses that has been shaped to deliver equal amplitudes after amplification showing (a) the pre-shaped input and (b) the amplified output at a total pulse energy of 6.5 mJ. For the simulations, the hard-cut in the stretcher is considered.

theory described in Sec. 2.2 and Sec. 2.4, the amplification can be simulated and reveal B-integrals of 25 rad, 18 rad, 12 rad and 7 rad for the first, second, third and fourth pulse, respectively. According to the discussion of the impact of B-integral mismatches between pulses to be combined, as illustrated by Fig. 3.7b in Subsec. 3.1.3, the combination efficiency drops significantly for $\Delta B \gtrsim 1$ rad. Additionally, not only the large B-integral mismatches make the pulses difficult to combine, but the high nonlinearity level itself reduces the pulse quality. As already indicated in Subsec. 3.2.3, the equalization of the pulse amplitudes is only efficient for B-integrals $\lesssim 1$ rad. At higher B-integrals, the ΔB among the pulse replicas need to be reduced. This typically results in a shape of the amplified burst with decreasing amplitudes.

To illustrate this behavior, the three major burst shaping scenarios are summarized in Fig. 5.4. This simulations are related to the experimental conditions[4] with an amplified output of 2.4 mJ. First, the amplification of a burst of stretched pulses with equal input amplitudes is assumed without any shaping and optimization. In Fig. 5.4a-d the input (shaded in grey) and the output burst, the evolution along the amplifier fiber of the pulse energies and the B-integrals of the individual pulse replicas as well as the stacked (uncompressed) pulse burst are shown. Since the first pulse experiences the full inversion of the fiber, it gets the highest gain, which progressively decreases for subsequent pulses. Thus, the output pulse energies are very different among the individual pulses of the burst. Associated to this is a strong spreading of the B-integrals, with a total difference of 4.3 rad. This, indeed, leads to a degradation of the pulse quality, the apparition of side-pulses and a drastic drop in the stacking efficiency. Moreover, a phase variation across

---

[4]The changed simulation parameters are: $\bar{P}_s = 1$ W, $f_{rep} = 30$ kHz, $\bar{P}_p = 100$ W.
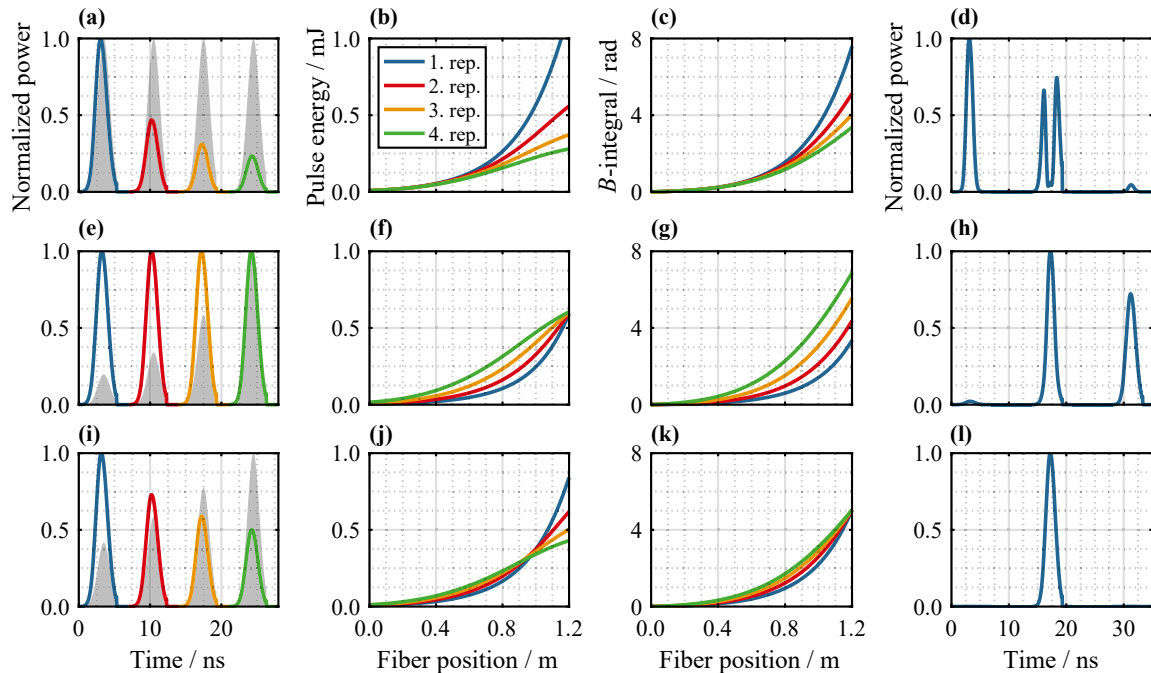
Figure 5.4.: Simulations of different burst shaping scenarios for (a)-(d) the unshaped case, with (a) showing the input (shaded in gray) and the amplified output burst of stretched pulses, (b) showing the evolution of the pulse energies of the pulse replicas along the amplifying fiber, (c) showing the evolution of the B-integrals and (d) the uncompressed stacked pulse, (e)-(h) equivalently the case of matched amplitudes at the output and (i)-(l) the case of matched B-integrals. In each case the total output energy is 2.4 mJ.

the main pulse leads to severe modulations in its pulse envelope. It is easy to see from the figures that the energy contained in the first pulse of the burst is the limiting factor for the energy extraction due to the damage limit of the fiber. This can be considerably improved if the input burst is shaped such that the output pulses are of equal amplitudes and an optimization[5] for the pulse stacking is applied, which is illustrated in Fig. 5.4e-h. As can be seen, the pulse energies of the individual pulses evolve in such a way that they become identical at the fiber output. Due to the uniform energy distribution, the energy contained in the first pulse is approximately halved compared to the unshaped case. However, there is still a discrepancy in the B-integrals, which hampers an efficient pulse stacking. For the last case, the input burst is shaped to match the B-integrals of the individual pulses of the output burst, which is illustrated in Fig. 5.4i-l. As a consequence, a burst shape of decreasing amplitudes is obtained, but to a much weaker extent compared to the unshaped case. The stacking efficiency is greatly improved, with only $< 0.2\%$ of energy lost in side-pulses. Depending on the strength of the nonlinearities,

---

[5]The optimization includes the variation of the HWPs and a constant compensation phase, as done by the active stabilization, for each pulse stacking step.

the optimum case will usually be somewhere in between the cases of matching amplitudes and B-integrals. However, B-integral mismatches have the most severe impact on the efficiency and are typically the dominating effect. It is worth noting that at a certain extracted energy the energy contained in the first pulse determines the damage limit.

Despite these shaping strategies, saturation-induced burst deformation typically is an unwanted effect. When targeting a certain energy at the output of the fiber, this deformation can be mitigated by increasing the saturation energy[6]. According to Eq. (2.24), this can be realized, for example, by increasing the core size of the fiber.

In order to experimentally verify these findings, in a first proof-of-principle the amplified burst is sent through the stacking stage. The repetition rate is set to 30 kHz to exploit the average-power capability of the fiber. Applying active stabilization, stable operation up to about 2.4 mJ overall energy (72.5 W average power) at the fiber output could be achieved. This energy (E) corresponds to an operation at $E/E_{\mathrm{sat}} \approx 2$. At this energy the system efficiency decreased from initially more than 89% to 75%. This system efficiency is shown in Fig. 5.5a as a function of the energy contained in the stacked pulse (red solid markers). Additionally, the results using the split-step Fourier simulation tool[7], including dispersion, SPM and the B-integral optimization, are depicted (green square markers). There is a clear discrepancy between the experiment and the theoretical expectation, which will be discussed later on. In contrast, with passive DPA, according to the simulated efficiencies depicted in Fig. 3.14g, an operation at $E/E_{\mathrm{sat}} \gtrsim 2$ would not have been possible. The corresponding combined pulse is shown in Fig. 5.5b, where pre- and post-pulses are hard to discern. The possible temporal positions of these pulse replicas are indicated by the dashed lines. Finally, the pulses are compressed with a compressor efficiency of 75% resulting in 1.25 mJ pulse energy (37.5 W average power). The measured autocorrelation, depicted in Fig. 5.5c, shows wings arising from residual nonlinear phase terms. The (matched) B-integral is estimated to be 6.3 rad. Assuming a sech^2 pulse shape (corresponding to a deconvolution factor of 1.54), the pulse duration is estimated to be 380 fs, which corresponds to a peak power of 2.9 GW [140].

Theoretically, a system efficiency $> 90\%$ should be possible according to the simulation, which is denoted in Fig. 5.5a by the green square markers. Although this confirms

---

[6]This can be seen from Eqs. (2.22) and (2.23). Increasing the saturation energy reduces the exponential term containing the integral that is responsible for the deformation. Otherwise the seed pulse energy has to be decreased.

[7]The main simulation parameters are: $\bar{P}_{\mathrm{s}} = 1$ W, $f_{\mathrm{rep}} = 30$ kHz, $\bar{P}_{\mathrm{p}} = 48 \ldots 120$ W (counter propagation), $\lambda_{\mathrm{s}} = 1028$ nm, $T_0 = 200$ fs (spectral hard-cut considered), $\lambda_{\mathrm{p}} = 976$ nm, $L = 1.1$ m, MFD = 75 μm, $d_{\mathrm{clad}} = 280$ μm, $d_{\mathrm{dop}} = 70$ μm, $n_2 = 3.2 \cdot 10^{-20}$ m^2/W, $\beta_2 = 19$ fs^2/mm, $N_{\mathrm{tot}} = 3 \cdot 10^{25}$ m^{-3}, $\tau_2 = 800$ μs, the cross-sections shown in Fig. 2.1a, $T_{\mathrm{p}} = 0.97$ and $R_{\mathrm{s}} = 0.99$ for the PBSs.
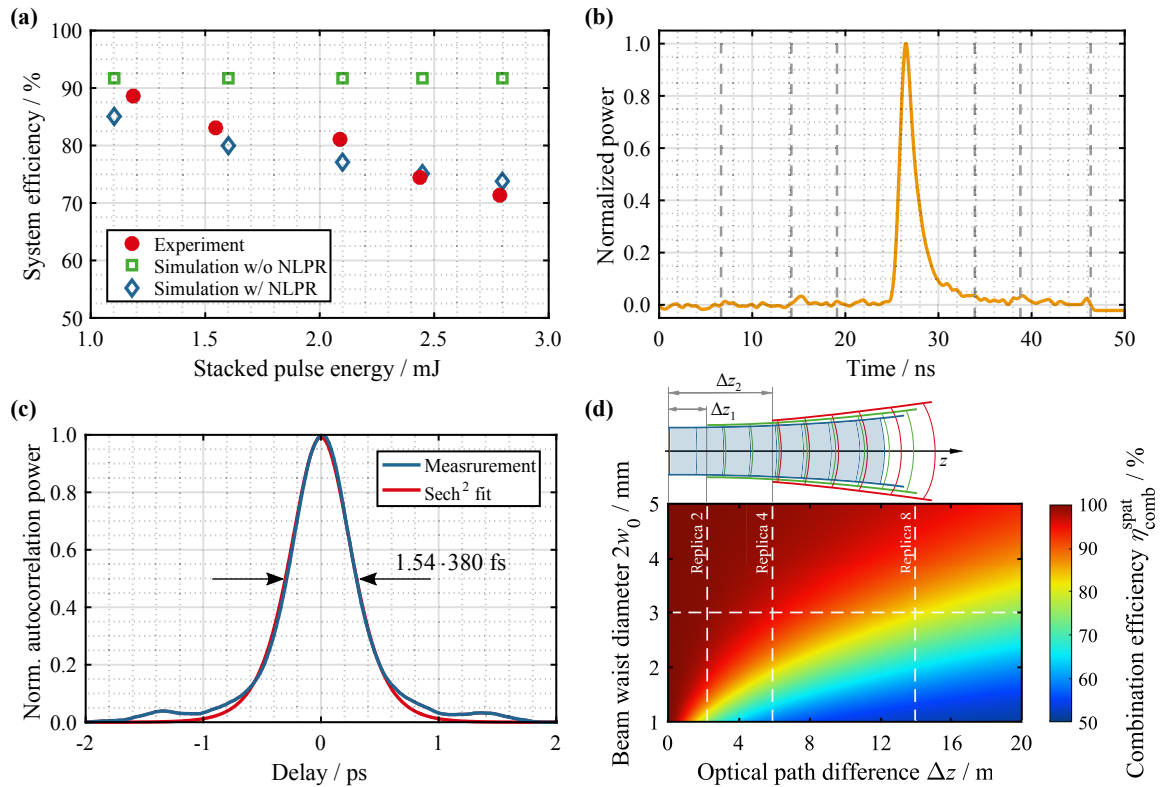
Figure 5.5.: (a) System efficiency as a function of the stacked (uncompressed) pulse energy for the experiment (red solid circle markers) and the simulation with and without NLPR (blue diamond markers and green square markers, respectively). (b) Photo-diode trace of the stacked pulse at a pulse energy of 2.4 mJ (measured with a 1-ns-rise-time photo-diode). (c) Measured autocorrelation trace and sech^2 fit. (d) Simulated combination efficiency for two Gaussian beams originating at $z = 0\,\mathrm{m}$ as a function of their beam-waist diameters $2w_0$ and of the optical path difference Δz between them. The lengths corresponding to the two delay lines from the experiment (as well as a potential third one) and the beam waist diameter are marked as dashed lines.

the predictions from Subsec. 3.2.3, experimentally an energy- or peak-power-dependent decrease in efficiency is observed. In order to investigate this mismatch with the simulation, different effects need to be taken into account. Effects, such as the onset of self-focusing (Subsec. 2.4.2), the spectral reshaping (Subsec. 3.2.3) and the electronically-induced refractive-index change [156, 157] have been considered and it was found that these play a minor role. Another possibility for the degradation of the efficiency is non-linear polarization rotation (NLPR) in optical fibers (Subsec. 2.4.2). Regarding a fiber amplifier operating with high nonlinearity, this effect is recognized as a power loss when placing a linear polarizer after the amplifier. Due to the peak-power differences between the pulse replicas within the amplified burst (which is required to match their B-integrals) NLPR is different for each replica hampering a correct power division at a subsequent PBS

in the delay lines. This may result in an efficiency decrease. A drop in efficiency similar to that observed in the experiment could be obtained in the simulations when adding the effect of NLPR[8]. This is, additionally, depicted in Fig. 5.5a using blue diamond markers. The experimental observations can, then, be potentially explained by this effect.

Moreover, differences in the optical path between the delayed and the non-delayed beams occurring in the pulse stacking stage may lead to beam-parameter mismatches, in terms of wavefront curvature and beam size, caused by beam divergence. While the optical path difference between the first and the second pulse is $\Delta z_1 = 2.2\,\mathrm{m}$ according to the first delay line, the difference between the first and the fourth pulse is $\Delta z_2 = 5.9\,\mathrm{m}$. Thus, depending on the beam size and the optical path difference Δz, as discussed in Subsec. 3.1.3, this may degrade the combination efficiency. To illustrate this effect, the resulting combination efficiency for the superposition of two Gaussian beams, according to Eq. (2.10), as a function of the beam-waist diameter $2w_0$ is shown in Fig. 5.5d. Thereby, one of the two beams is propagated a distance Δz, according to Eq. (2.11). As predicted by the beam-parameter product [49], smaller beams diverge more strongly, which leads to a more pronounced impact on the combination efficiency. The beam size in the experiment was about $3\,\mathrm{mm}$. This diameter and, additionally, the lengths Δz_1 and Δz_2 are marked in Fig. 5.5d by dashed lines. A potential third delay line, required for stacking eight pulse replicas, is additionally marked. As can be seen, while the impact of the short delay line is negligible, both delay lines together should cause a combination loss of about 5%. Please note that the results presented correspond to the combination of two pulse replicas. In the case of four or more pulses the effect on the efficiency is expected to be lower.

On top of this, the power ratio between the pulse replicas can be as high as two, as can be seen from Fig. 5.4i, which has an additional impact on the efficiency because of the unmatched powers between the pulses to be combined, as can be seen in Fig. 3.6c. Note, however, that this represents a constant loss, neglecting mode-size changes at the fiber output, and does not explain the energy-dependent loss from Fig. 5.5a. Experimentally, this loss can be observed as a ring-shaped beam being ejected at the loss port of the final PBS (see Fig. 5.1). In general, the beam-parameter mismatch can be improved either by increasing the beam size to $\gtrsim 5\,\mathrm{mm}$ or by employing $4f$-imaging delay lines.

In the last part of this section different implementations of the delay lines for pulse division/stacking are discussed. The reason for this is the unstable operation of the main amplifier observed when employing high-gain amplifiers (as it will be reported in the next

---

[8]In general, the interaction of both intrinsic and nonlinear birefringence and degenerate four-wave mixing, governed by the coupled Schrödinger equations [26], is of complicated nature. Although NLPR has been added to the simulation tool and the overall trend of the efficiency decrease in Fig. 5.5a can be reproduced, the results are not reliable since the birefringence of the fiber is unknown.

experiment presented in Subsec. 5.2.2) in conjunction with double-pass delay lines (used for the experiment described in this section, see Fig. 5.2). Double-pass delay lines are employed for the temporal pulse division due to their advantage of being compact and easy to adjust. This implementation has also been used for pulse stacking. However, in case of non-ideal PBSs ($T_{\mathrm{p}} < R_{\mathrm{s}} < 1$) the interferometric match of the beam path may cause back reflections and, thus, lasing of the main amplifier. The stacking of two orthogonally-polarized pulses of equal power is depicted in Fig. 5.6a as an illustration of this. The *s*-polarized pulse is delayed and superposed with the *p*-polarized non-delayed pulse, as already described in Subsec. 5.1.1. More specifically, the *s*-polarized pulse is reflected in the first part of the delay line and, after a double pass through a QWP, its polarization is rotated to *p*-state so that it is transmitted through the PBS, entering the second part of the delay line. However, upon this transmission, a small amount of the power within the delay line, namely $R_{\mathrm{s}}(1 - T_{\mathrm{p}})$, can be reflected back towards the input. For example, in case of the PBSs used in the experiment, with $T_{\mathrm{p}} = 0.97$ and $R_{\mathrm{s}} = 0.99$ and assuming two pulse replicas of the same power, this results in about 1.5% feedback. This may lead to an unstable operation for high-gain amplifiers.

In order to prevent back reflections, single PBS ring-implementations or double PBS implementations can be used. For the first case, the delayed beam travels along a loop being reflected twice at the PBS as illustrated in Fig. 5.6b. In the case of two PBSs, as illustrated in Fig. 5.6c, potential pre- and post-pulses are mitigated by the second PBS. The pulse contrast, as discussed in Subsec. 3.2.2, can be an important parameter for particular applications. Thus, while for both single PBS cases the fraction $(1 - R_{\mathrm{s}})$ of the power from the first pulse is generated as pre-pulse, for the case of two PBSs it is $(1 - R_{\mathrm{s}})^2$ and, thus, much weaker. Assuming the values from above, these result in
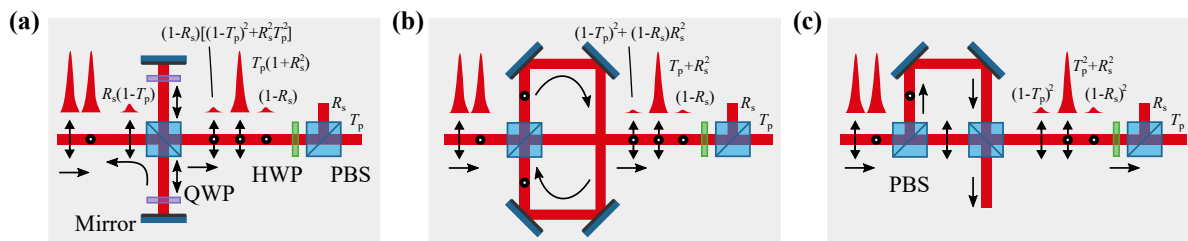

Figure 5.6.: Different possibilities of the delay-line layout using (a) a single PBS implementation with a double pass, (b) a single PBS implementation with a ring pass and (c) a double PBS implementation. The power content of each pulse is given in terms of the power transmissivity T_{p} and power reflectivity R_{s} of the PBS.

0.5% and 0.005% of the total energy[9], respectively. The power fractions of the generated pre- and post-pulses of either case are given in Fig. 5.6a-c. Please note that, since the polarization state of any pre- and post-pulse is rotated approximately 45° with respect to the main pulse, about half of their power is ejected at the subsequent PBS. In the following experiments, back-reflection-free delay lines for pulse stacking are used.

5.2. Spatio-Temporal Combination

In the previous section, aDPA has been presented and demonstrated in a proof-of-principle experiment. In contrast to passive DPA, saturation effects of the amplifier can be counteracted and higher pulse energy achieved. Compared to the state of the art prior to this work, the pulse energy could be improved by a factor of almost three [38]. In the following, the temporal combination concept will be used in a setup that also incorporates spatial combination. Therefore, the scalability of the aDPA architecture is exploited and applied to an amplifier array.

5.2.1. Principle

The second experimental part of this thesis focuses on merging both the spatial and the temporal combination concepts in order to scale the achievable pulse energy at high average powers beyond the current state of the art. The conceptual changes to the aDPA architecture presented in Subsec. 5.1.1 are explained in the following.

A principle scheme is depicted in Fig. 5.7. While the temporal pulse division and subsequent pulse stacking stages correspond to the aDPA implementation shown in Fig. 5.1, the single amplifier is now replaced by an amplifier array. Here, a burst of four pulse replicas (potentially shaped), analogous to the description from Subsec. 5.1.1, is considered. The pulse replicas within the burst are orthogonally polarized, i.e. s- and p-polarized, in alternating order. Thus, another HWP (set to $\theta = 22.5°$) and PBS can divide the burst into the two branches of a Mach-Zehnder-type interferometer. As a result, bursts of four pulses enter each branch. While the reflected burst is s-polarized, the transmitted burst is p-polarized, which is rotated to the s-polarization upon a double pass in a delay line including a piezo-driven mirror for active-phase stabilization. Please note that the respective phase information in terms of the incident state of polarization remains imprinted

---

[9]Please note that including angle uncertainties of the HWPs (Subsec. 3.2.2) will increase the energy contained in these parasitic pulses. Moreover, in the case of more than two pulse replicas saturation-induced amplitude and nonlinear-phase mismatches (Subsec. 3.2.3) will additionally affect this pulse contrast.
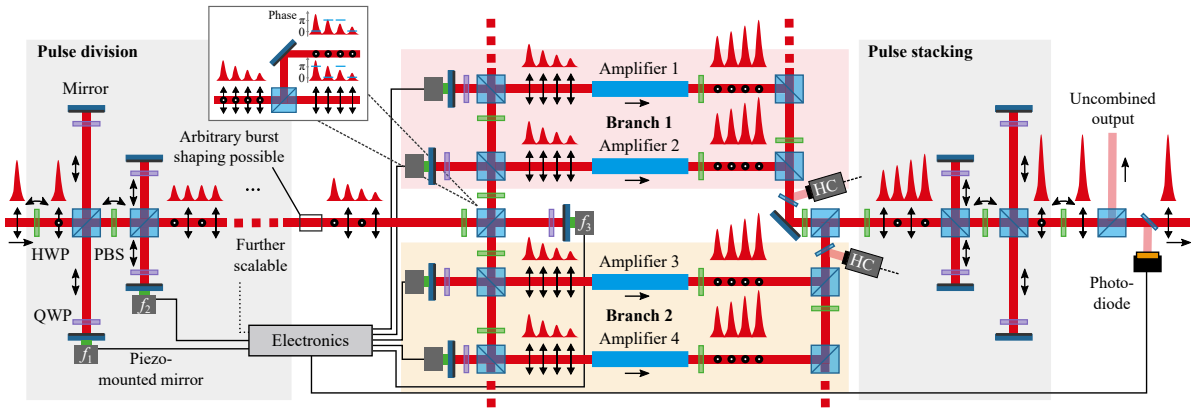
Figure 5.7.: Schematic of the spatio-temporal combination implementation showing the pulse burst generation and shaping of up to four pulse replicas, their amplification in four amplifier channels and subsequent combination. Dotted beam parts indicate further potential extensions.

on each pulse replica, which is illustrated by the inset in Fig. 5.7. Thus, upon combination, the initial polarization pattern will be recovered. As introduced in Subsec. 3.1.2, the division into two separate branches is considered as a tree-type division. Within each branch of the Mach-Zehnder-type interferometer further divisions in sub-branches can be introduced, which is indicated in Fig. 5.7 for four amplifier channels using a bus-type implementation. For each sub-branch, an active stabilization is required. Please note that the number of channels within each branch can be scaled independently; however, the powers of the two branches or the splitting ratio of the combination element have to be matched, as discussed in Subsec. 3.1.3.

After amplification, all divided beams are combined and all divided pulses are stacked upon each other. For active stabilization of both the temporal and the spatial combination, LOCSET (as explained in Chap. 4) can be applied. In Subsec. 5.1.1 it has already been mentioned that the HC method cannot be used to stabilize the stacking of temporally divided pulses with orthogonal polarizations. However, the number of modulation frequencies required for LOCSET scales linearly with the number of channels and delay lines to be stabilized, reducing the available regulation bandwidth. Fortunately, the polarization of the bursts within the sub-branches is homogeneous, making the application of HC possible. Therefore, for each combination step within the main branches, HC detectors are required. This is indicated in Fig. 5.7 for the combination of two amplifiers denoted by 1 and 2 in branch 1 as well as 3 and 4 in branch 2. LOCSET, again, is required later in order to stabilize the final spatial superposition, after which the orthogonal polarization pattern in the burst is recovered. Thus, for the stabilization of N amplifier channels and M delay lines $M + 1$ modulation frequencies and $N - 2$ HC detectors are

necessary. It is worth noting that all uncombined fractions upon the beam combination of the sub-branches are ejected by subsequent PBSs, while those of the final spatial combination step and all temporal stacking steps are ejected at the final PBS in the following manner: half through the loss port and half through the output. In the following, the first experimental demonstration of an actively-controlled spatio-temporal combination setup will be presented.

5.2.2. Experimental Demonstration

The small-signal gain and the saturated amplification regime were explained in Subsec. 2.2.4 and in Subsec. 3.2.3 it was shown that aDPA allows for high system efficiencies in both regimes. The intention of the following experiment is to demonstrate the spatio-temporal combination, i.e. aDPA with four pulse replicas amplified in two amplifier channels, and to investigate its efficiency in the mentioned amplification regimes.

Setup

In order to demonstrate and explore the feasibility of the actively-controlled spatio-temporal combination scheme, a proof-of-principle experiment has been performed [141]. A low-power setup has been built, which is shown in Fig. 5.8. The goal of this setup is to test the system efficiency in both the small-signal gain and in the saturated amplification regimes with different B-integrals. Even though, for a given amplifier, short pulses are required to increase the impact of nonlinear effects without saturating the amplifier, longer pulses are advantageous for saturating the amplifier while keeping the nonlinearity moderate. Thus, two different front-ends, providing femtosecond pulses with different stretching ratios, are employed. While for the first one 200 fs pulses from a 40 MHz bulk mode-locked oscillator are stretched in 170 m fiber with a 6 µm core to a duration of approximately 50 ps, for the second one pulses from the CPA front-end described in Subsec. 5.1.2 (which are femtosecond pulses stretched to approximately 1.5 ns duration) are used. These pulses are pre-amplified in two core-pumped Yb-doped 6 µm-core SIFs with lengths of 1 m each, enclosing an AOM in order to provide mW-level seed pulses adjustable in energy. The clock signal is picked with a photo-diode after the output of the front-end and optical isolators are used between the amplifiers. The pulse division and shaping of up to four pulse replicas is realized using the same free-space delay lines described in Subsec. 5.1.2. The lengths are chosen to provide a constant temporal separation of 4.3 ns between each pulse replica. After the temporal division a spatial one is done using another HWP and a PBS cube, which split the burst in two amplifier channels. Thus, according
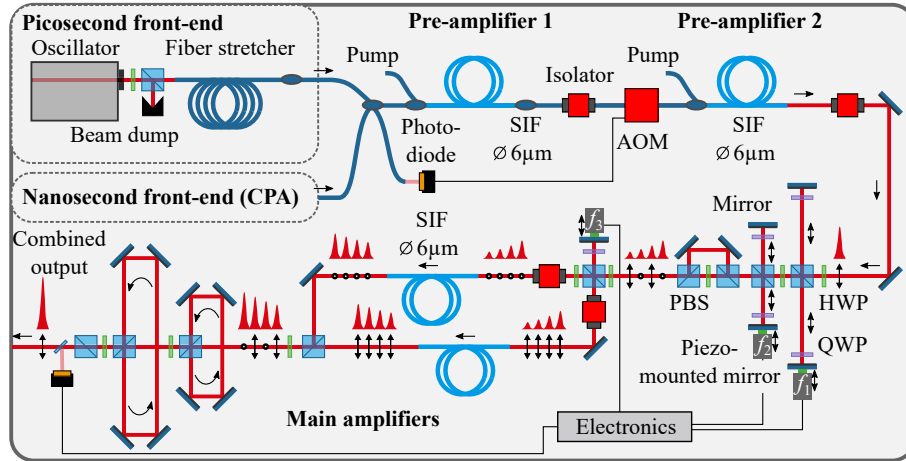
Figure 5.8.: Experimental setup used to demonstrate the spatio-temporal amplification and combination of bursts comprising up to four pulse replicas amplified in two amplifier channels. The setup can be seeded by two different front-ends that deliver femtosecond pulses stretched to either picosecond or nanosecond duration. Additionally, the system includes two pre-amplifiers and two parallel main amplifiers all using step-index-fibers (SIFs), as well as an acousto-optic modulator (AOM), optical isolators, temporal and spatial pulse division and combination stages. The red lines denote free-space propagation, the blue lines denote propagation in fibers (light blue corresponds to Yb-doped fibers) and the black lines are electronic connections. The grey box represents the part of the setup placed in a housing.

to the description from Subsec. 5.2.1, bursts of four pulses and homogeneous polarization enter each channel. Please note that due to the single polarization state of the burst, standard optical isolators can be employed in each channel. The bursts are amplified in polarization-maintaining Yb-doped SIFs with core diameters of 6 µm and 1.2 m length. Each pump diode provides up to 300 mW at 976 nm. After amplification, the bursts are superposed and the initial polarization pattern is recovered. A piezo-driven-mirror delay line is employed to stabilize this Mach-Zehnder-type interferometer. In order to stack the burst again, the polarization orientation of the initial burst is rotated 90° by another HWP. Then the stacking is achieved using ring-delay lines to protect the high-gain main amplifiers from back reflections and, thus, lasing. Finally, a PBS cube separates the combined pulse from uncombined fractions. LOCSET is used for active stabilization, imprinting the modulation frequencies $f_1 = 7.3$ kHz, $f_2 = 6$ kHz and $f_3 = 4.5$ kHz with a modulation depth of around $\beta \approx 0.1$ on each delay line with the piezo actuators. Using a single detection at the output, error signals for the respective paths are generated, as described in Sec. 4.2, to maximize the combined output power.

Experiment

First, the 50 ps front-end is employed to investigate the system efficiency at high B-integrals in absence of amplifier saturation. Each main amplifier is seeded with 1 mW of average power that is amplified to a maximum of 280 mW. In order to increase the pulse energy and, thus, the B-integral, the repetition rate is decreased step-wise from initially 10 MHz down to 56.8 kHz. The energy of each channel is kept well below the damage threshold of the fiber, which is estimated to be 3 μJ (according to Eq. (2.30) assuming an MFD of 7.3 μm without end-cap). Moreover, the amplifiers are not saturated, since the saturation energy is about 12 μJ per channel (Eq. (2.24)). The system efficiency achieved is depicted in Fig. 5.9a as a function of the stacked pulse energy, i.e. the energy at the output of the final PBS contained in the main pulse. This efficiency includes the spatial combination of both amplifiers for the case of a single pulse and the division into bursts of two or four pulse replicas, depending on the settings of the HWPs in the pulse division and stacking stages. As can be seen from the figure, with increasing pulse energy and, therewith, B-integral only a slight decrease in efficiency is observable. For each further pulse division, the energy can be increased further, while the system efficiency stayed above 80% even for operation above the damage threshold ($E_{\mathrm{dam}} < E_{\mathrm{sat}}$, shown as dotted line in Fig. 5.9a). The B-integrals in the main amplifiers at the maximum energies are 28 rad, 22 rad and 18 rad when using one, two, and four pulse replicas, respectively. Of course, such high B-integrals drastically degrade the pulse quality after compression; however, this is not considered here since only the combination process is analyzed in this study. The decay in efficiency is attributed to residual B-integral differences between
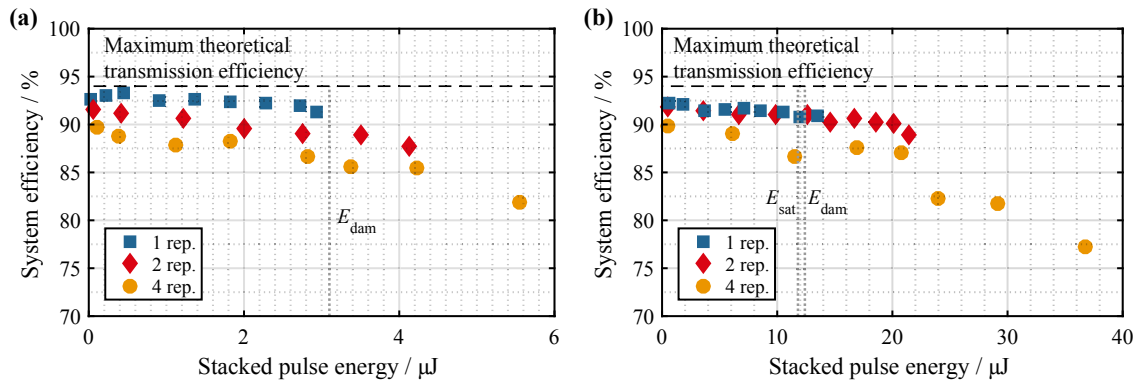

Figure 5.9.: System efficiency as a function of the stacked pulse energy (within the main pulse at the output) for the combination of two amplifier channels with or without pulse division (1 rep., 2 rep., 4 rep.) for (a) 50 ps pulses and (b) 1.5 ns pulses. The maximum theoretical system efficiency for the transmission through the combination setup for $T_{\mathrm{p}} = 0.98$ and $R_{\mathrm{s}} = 0.99$ is indicated by the horizontal dashed line. The damage energy E_{dam} and the saturation energy E_{sat} are indicated by the dotted lines.

the amplifiers[10] and among the individual pulses in the bursts, which gets aggravated for high B-integrals. Furthermore, the maximum possible system efficiency depends on the specifications of the PBS cubes (disregarding Fresnel reflections at the surfaces of all optical components), leading to constant levels below 100% efficiency. The transmission characteristics of K PBSs used for the spatial combination and pulse stacking can be calculated by $(T_p^K + R_s^K)/2$. Thus, considering $K = 3$ (for the case of four pulses) and, additionally, a transmission through the final PBS (T_p), this maximum system efficiency is $\sim 94\%$ (for $T_p = 0.98$ and $R_s = 0.99$), which is indicated by the dashed line in Fig. 5.9a. The offset between the measurement series for different pulse numbers is most likely due to slight beam-parameter mismatches, according to the discussion in Subsec. 3.1.3.

In a next step, the 1.5 ns front-end is employed in order to saturate the amplifiers. Note that, due to the longer pulse duration, the damage threshold increases to reach a level similar to the saturation energy. Again, the system efficiency for the same cases described above is determined, which is depicted in Fig. 5.9b ($E_{dam} \approx E_{sat}$, shown as dotted lines). Now the overall seed pulse energy is increased from 2 nJ to 0.5 µJ by reducing the repetition rate from 1 MHz to 3.9 kHz. The pulses are amplified to a maximum average power of 300 mW for each channel, while the energy of each pulse replica is kept below the damage energy. The stacked pulse energy, shown in Fig. 5.9b, is corrected for both the system efficiency and the amplified spontaneous emission (ASE), which is determined to be $< 7\%$ below 10 kHz. For a pulse energy below E_{sat}, the decrease in efficiency is attributed to the same effects as for the picosecond pulses. Above E_{sat} saturation becomes more pronounced leading to a further drop in efficiency caused by residual phase mismatches between both channels and among the pulse replicas in the burst. A maximum stacked pulse energy of 37 µJ (verified by energy-meter measurements at < 10 kHz) is achieved, which is about three times above the fiber damage threshold for a single pulse. At that energy, the B-integral in the main amplifier is estimated to be 7 rad, while the system efficiency stayed above 76%. This achievement already proves the power-scaling capability of the spatio-temporal combination approach. Please note that for this setup the repetition rate had to be decreased below the modulation frequencies for the active stabilization in order to reach a high seed-pulse energy. Thus, only short-term stable operation thanks to a housing could be achieved for repetition rates $\lesssim 10$ kHz.

The input and amplified bursts of both main amplifiers at the highest energy are shown in Fig. 5.10a, whereas the corresponding stacked pulse is shown in Fig. 5.10b (the beam profile is shown in the inset). Please note that, due to the time-frequency mapping at

---

[10]Please note that NLPR (see Subsec. 2.4.2) can be neglected due to the high stress-induced birefringence of the polarization-maintaining fibers.
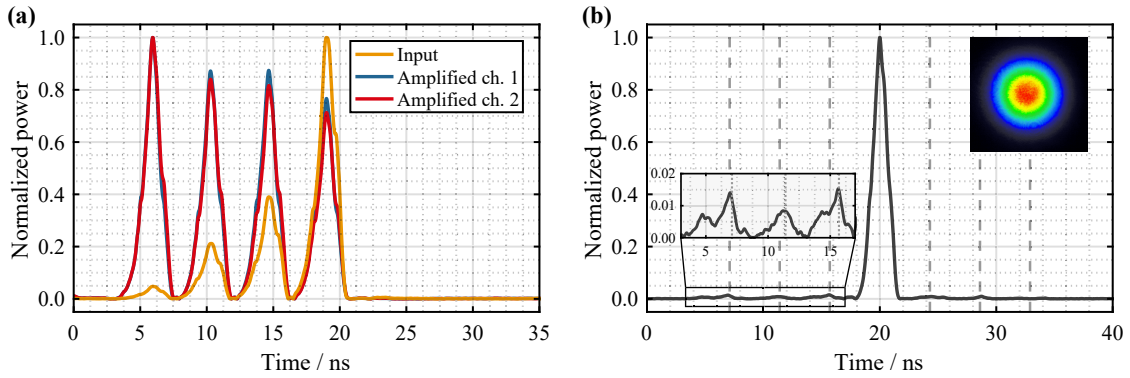
Figure 5.10.: Photo-diode traces of (a) the shaped input burst prior spatial division (orange) and at the outputs of both amplifiers (red and blue) and (b) of the stacked pulse at the stacked pulse energy of $37\,\mu J$ (measured with a $< 18\,ps$ rise-time photo-diode together with a $30\,GS/s$ sampling scope). Beam profile and magnified pre-pulses shown as insets.

large stretching ratios, the temporal pulse shape corresponds to the spectral shape. From the shaped input burst, the strength of the saturation effect is clearly visible. As discussed in Subsec. 5.1.2, the equalization of the B-integrals results in a slight amplitude decrease of the individual pulse replicas within the amplified burst, which has an impact on the pulse contrast (Subsec. 3.2.2). Moreover, non-matched powers between both channels (or branches of the last spatial combination step) in polarization-based spatio-temporal combination setups can decrease the system efficiency and the pulse contrast, too. This power mismatch results in an unbalance between the superposed pulse amplitudes and, therewith, polarization components, which causes a change of the expected orthogonal polarization states between the pulse replicas after combination (for more details see Appendix B). However, in the experiment, the power ratio between the bursts shown in Fig. 5.10a is ~ 0.9 and, compared to the impact of nonlinear phase mismatches, negligible[11]. At the maximum energy level, the pre- and post-pulse contrast, according to Eq. (3.12), is $\mathcal{C} = 18\mathrm{dB}$. This is visualized by the magnifying inset in Fig. 5.10b.

In conclusion, actively stabilized spatio-temporal combination has been demonstrated for the first time in a proof-of-principle experiment. Efficient operation has been achieved for both low pulse energy at high B-integral and high pulse energy in amplifier saturation, demonstrating the capability of the actively-controlled implementation. However, during this experiment another effect during long-term operation has been observed, which will be discussed in the following subsection.

---

[11]The powers between both amplifier channels were almost matched. However, the saturation effect on the bursts from both channels was slightly different, as can be seen from Fig. 5.10a, leading to a varying power ratio between the polarization components along the superposed burst.

5.2.3. Temporal Gating

In order to investigate the long-term stability of such a spatio-temporal combination setup, the combined output power is measured over the duration of one hour. Using the nanosecond front-end and operating at a repetition rate of 2.5 MHz to exclude saturation and nonlinearities, the measured trace of the combined average power is shown in Fig. 5.11a. This plot has been obtained when employing a burst of four pulse replicas on both amplifier channels. Besides a weak thermal drift that reduces the power by ~2%, an undesired bistable operation is observable. Over the course of several minutes the power switches between the desired maximum level and a roughly 25% lower power level, which will be referred to as state 1 and state 2, respectively. The corresponding temporal characteristic of the stacked burst is shown as captured by a fast-photo-diode measurement in Fig. 5.11b. The bursts are either stacked correctly into a single pulse (state 1) or distributed symmetrically around the expected temporal position (state 2). This behavior was not observed in the first aDPA experiment. Thus, it seems to occur only for more than two temporal pulse divisions.

An analytic solution of the corresponding LOCSET error signals for the setup shown in Fig. 5.8 is derived, following the same calculation steps as explained in Sec. 4.2 [158], to analyze this phenomenon. In order to do this the temporal and spatial pulse division and combination is considered using a simplified quasi-time-resolved Jones calculus based on the formalism described in Subsec. 2.3.3. The complete derivation is described in detail in Appendix C. To stabilize both temporal stacking steps (denoted as 1 and 2), as well as the spatial combination step (3) using the relative phase errors $\Delta\phi_m$, the modulation frequencies f_m and the modulation depths β_m are considered, with $m = 1, 2, 3$. Finally, the error signals after demodulation, according to Eq. (4.6) and choosing an integration
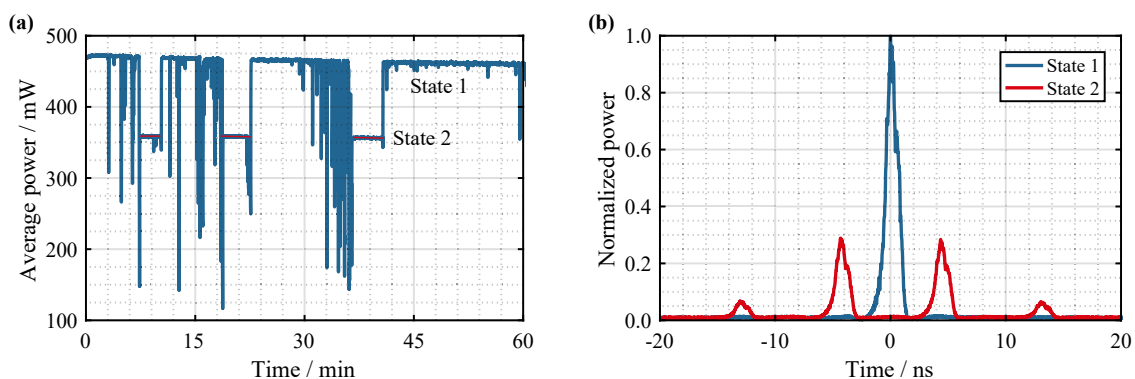

Figure 5.11.: Long-term stability showing (a) the measured average power for the combination of two amplifier channels and four pulse replicas and (b) the corresponding photo-diode traces of the stacked pulses for the two dominant operation states.

time such that it isolates neighboring modulation frequencies, are given by

$$S_1 \sim J_1(\beta_1)\sin(\Delta\phi_1)\left\{J_0(\beta_3)\cos(\Delta\phi_3)\left[J_0(\beta_2)\cos(\Delta\phi_2)+2\right]+J_0(\beta_2)\cos(\Delta\phi_2)\right\}, \quad (5.1)$$

$$S_2 \sim J_1(\beta_2)\sin(\Delta\phi_2)J_0(\beta_1)\cos(\Delta\phi_1)\left[J_0(\beta_3)\cos(\Delta\phi_3)+1\right], \quad (5.2)$$

$$S_3 \sim J_1(\beta_3)\sin(\Delta\phi_3)J_0(\beta_1)\cos(\Delta\phi_1)\left[J_0(\beta_2)\cos(\Delta\phi_2)+2\right], \quad (5.3)$$

where J_n are Bessel functions of the first kind and nth order. Comparing to Eq. (4.7), there are additional terms occurring. As can be seen, the respective error signals depend mutually on the phase errors of the different regulation channels. Thus, they influence each other. The reaction of the closed-loop regulation depends then on both the sign and the slope of the respective error signal as it strives for vanishing signals. Hence, for each zero-crossing with the same slope of S_m, a stable operation point is obtained, which in general can be expressed by

$$S_m = 0 \quad \wedge \quad \frac{\partial S_m}{\partial \Delta\phi_m} > 0 \quad , \; \forall \, m \in \{1,2,3\}. \quad (5.4)$$

Applying Eq. (5.4) to Eqs. (5.1)-(5.3) reveals the observed states from Fig. 5.11. State 1 (correct pulse combination) is obtained for $\Delta\phi_1 = \Delta\phi_2 = \Delta\phi_3 = 0\,\mathrm{rad}$, while the undesired state 2 is obtained for $\Delta\phi_1 = \Delta\phi_2 = \Delta\phi_3 = \pi\,\mathrm{rad}$. The latter one rotates the expected polarization pattern of the burst upon spatial superposition by $90°$. For purposes of understanding, the burst combination after amplification is considered step-wise, following Fig. 5.8. There, the p- and s-polarized pulses from the burst propagate along the opposite optical paths at the subsequent temporal pulse-stacking delay line, leading to a further temporal spreading of the burst instead of to a superposition. Since both the short and the long delays τ_2 and τ_1, respectively, are not matched interferometrically, i.e. $2\tau_2 \neq \tau_1$, the pulses are superposed only partially at the second temporal pulse-stacking delay line, resulting in the observed state 2 from Fig. 5.11b. Hence, if there are instantaneous phase perturbations (such as mechanical vibrations or even a shock of the laser system) that are significant enough to flip the sign of the respective error signal, the stabilization system will switch between both mentioned states.

The reason of this bistability can be found in the different possibilities for optical paths that the delay lines provide in the temporal pulse-stacking stage. This problem is not limited to LOCSET, for example hill-climbing algorithms such as SPGD will yield the same result, since the combined output average power exhibits two local maxima (compare to Eq. (C.27) in the appendix).

There are different possibilities to mitigate the mentioned bistability issue. Besides a

peak-power sensitive measurement, such as a nonlinear process, and introducing a minimum power threshold, altering the error signals themselves such that the undesired states vanish, ultimately eliminates the instability. This can be realized by using a temporal gate for the raw-signal acquisition that lets only the desired stacked pulse go through. This can be implemented optically by employing, for example, a Pockels cell or electronically by employing a fast electronic switch. Then, the error signals according to Eqs. (5.1)-(5.3) change to[12]

$$S_m \sim J_1(\beta_m) \sin(\Delta\phi_m) \left[1 + J_0(\beta_i) \cos(\Delta\phi_i)\right] \left[1 + J_0(\beta_j) \cos(\Delta\phi_j)\right], \qquad (5.5)$$

with the permutations $\{m, i, j\}$ of the regulator channels $\{1, 2, 3\}$. The error signals from Eq. (5.5) still influence each other, but no sign reversal occurs[13], which suppresses the undesired secondary stable state. This becomes evident when applying Eq. (5.4). It is worth noting that a temporally-gated HC detection may also be applied to temporal pulse stacking, since a single pulse will be windowed.

In order to generalize Eq. (5.5), a simplified simulation is done that resembles the analytic calculation described in Appendix C. With this, the number of temporal and spatial pulse divisions can be increased. However, no more than two amplifier channels need to be considered, since each further spatially separated amplifier channel can be treated as an independent subsystem (compare to Subsec. 5.2.1) for which the classical LOC-SET solution described by Eq. (4.7) remains valid (or the HC technique can be applied). Considering systems employing $N = 1$ or 2 amplifier channels and up to $K = 5$ delay lines for temporal pulse stacking, the obtainable number of stable states are illustrated in Tab. 5.1. For the case of $N = 1$ and $K = 5$, which is equivalent to $N = 2$ and $K = 4$, up to five stable states are possible. These are shown in Fig. 5.12. In all undesired stable states, temporally separated pulses are symmetrically distributed around the expected temporal position. For example, setting the first occurring combination steps to $\Delta\phi_1 = \Delta\phi_2 = 0\,\text{rad}$ reproduces the measurement from Fig. 5.11b with the analytic solutions shown in Fig. 5.12a and Fig. 5.12b. However, when applying the temporally-gated error-signal acquisition from above, the undesired states are suppressed and Eq. (5.5) can be expressed more generally, for K delay lines or $K-1$ delay lines and one spatial division,

---

[12]Only pulses at the temporal position $\tau_1 + \tau_2$ of Eq. (C.27) are considered.

[13]This can be seen from the cosine terms by comparing Eqs. (5.1)-(5.3) to Eq. (5.5). For the case without a temporal gate this cosine terms appear as factor, which may cause a sign change of the respective error signal S. In the case of a temporal gate being employed, these terms change to $[1 + J_0(\beta) \cos(\Delta\phi)]$. Since, typically, $0 < \beta < 1$ it follows that $J_0(\beta) < 1$ and, thus, no sign change occurs.

Table 5.1.: Stable states for spatio-temporal combination implementations with N amplifier channels and K delay lines (2^K pulse replicas).

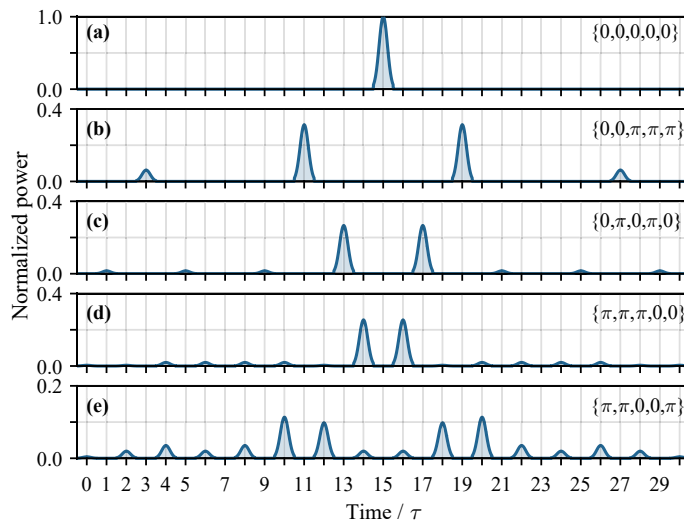| 2^K	N	
	1	≥ 2
2^0	1	1
2^1	1	1
2^2	1	2
2^3	2	3
2^4	3	5
2^5	5	> 5

Figure 5.12.: Illustration of the possible stable states plotted as multiples of the not interferometrically matched delay τ for a setup combining $N = 2$ channels and $K = 4$ delay lines with the corresponding phase errors denoted by $\{\Delta\phi_1, \Delta\phi_2, \Delta\phi_3, \Delta\phi_4, \Delta\phi_5\}$ (pulse traces are normalized to the peak power of the desired state (a)).

as[14]

$$S_m \sim J_1(\beta_m) \sin(\Delta\phi_m) \prod_{\substack{j=1 \\ j \neq m}}^{K} [1 + J_0(\beta_j)\cos(\Delta\phi_j)]. \tag{5.6}$$

All these findings from the proof-of-principle experiment are applied to the final experiment, which will be explained in the following.

5.2.4. High-Energy, High-Power Experiment

Setup

In this part the redesigned fiber-CPA system is described [137, 142], with which the spatio-temporal-combination approach could be scaled to high-performance levels. A schematic of the system is depicted in Fig. 5.13. The seed source is a 64 MHz Kerr-lens mode-locked Yb:KGW oscillator delivering 60 fs pulses at an average power of 1 W and a central wavelength of 1027 nm. These pulses are stretched to 1.3 ns FWHM duration using an Offner-type grating stretcher [152], which has a spectral hard-cut of 22 nm that is centered around 1032 nm. The stretcher and the final compressor share the same grating (even though it has been drawn separately in Fig. 5.13). Again, a mini-compressor and an

---

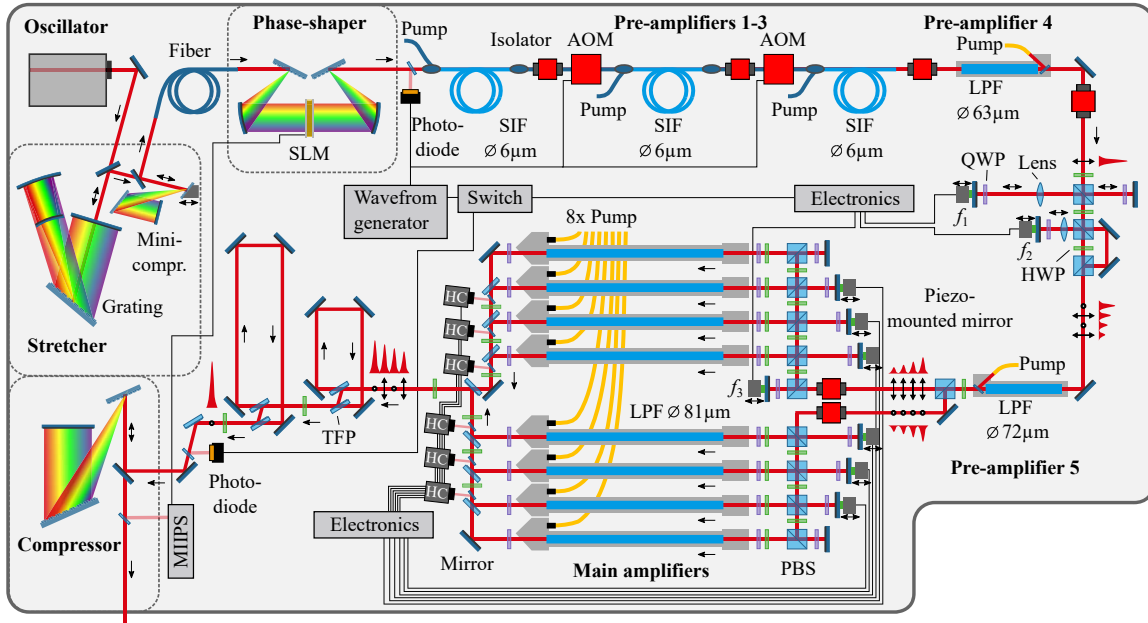[14]Equation (5.6) does not apply for the case of $K = 0$ and $N = 1$, as no combining occurs.

Figure 5.13.: High-power fiber-CPA system incorporating temporal pulse stacking of up to four pulse replicas that are amplified in eight main amplifier channels. The setup consists of an oscillator, a stretcher and a compressor, acousto-optic modulators (AOMs), a phase-shaper comprising a spatial-light modulator (SLM), five pre-amplifiers and eight main amplifiers including step-index fibers (SIFs) and large-pitch fibers (LPFs) as well as the temporal pulse division and stacking stages. Active stabilization is achieved by temporally-gated LOCSET and Hänsch-Couillaud (HC). The red lines denote free-space propagation, the blue lines denote propagation in fibers (light blue corresponds to Yb-doped fibers) and the black lines are electronic connections. The grey box represents the housing of the setup.

SLM are used to optimize the compressed pulse quality at the laser output. Afterwards, a clock signal is extracted using a photo-diode, to trigger all electronics in the system. The pulses are amplified in a three-stage all-fiber pre-amplifier section enclosing two AOMs with electronic pulse monitoring and emergency shutdown for damage protection of the main amplifiers [159]. This setup provides seed pulses with repetition rates adjustable between 55.9 kHz and 1.06 MHz corresponding to average powers between 8 mW and 40 mW, respectively. For stability improvements, all following free-space paths have been minimized. Next, the pulses are amplified in a free-space-coupled 80 cm long LPF with a core diameter of 63 μm to average powers between 200 mW and 400 mW. It is fixed in a water-cooled aluminum module to ensure high thermal stability. Throughout the system, optical isolators are placed in-between the amplifiers for feedback suppression. Subsequently, a burst of up to four orthogonally-polarized pulse replicas is generated by means of two double-pass delay lines, with lengths of 2.4 m and 1.2 m corresponding to delays of 8 ns and 4 ns, respectively. These, similar to those employed to previous experiments, comprise PBS cubes, HWPs and QWPs as well as piezo-driven mirrors for active phase

stabilization. For arbitrary burst shaping, an additional HWP is required, which is now included in the second delay line. In order to counteract mismatches in the divergence of the small beams due to their different propagation lengths, and to adapt them for coupling in the next amplifier, $4f$-imaging lenses are introduced in both delay lines. The final water-cooled pre-amplifier module consists of another LPF with a core-diameter of 72 μm and a length of 80 cm, which provides average powers up to 20 W as seed for the main amplifiers. Moreover, this fiber acts as spatial filter for the separate beams of the individual pulse replicas, which facilitates consistent coupling efficiencies in the subsequent main amplifiers.

In the main amplification stage the beam is divided in up to eight parallel amplifiers. The first division produces two main branches, each including linearly polarized bursts of up to four pulse replicas, which can be separately isolated from the pre-amplifier. Within each branch each beam is further split in a subsequent bus-type division stage and directed to four amplifiers. Piezo-driven mirrors are used in double-pass delay lines for active stabilization. Each main amplifier consists of an LPF with a core diameter of 81 μm and 1.1 m length, which is fixed in a compact, water-cooled aluminum module and is pumped by a wavelength-stabilized fiber-coupled pump diode that delivers up to 250 W. All pump diodes throughout the system operate at 976 nm. Furthermore, to prevent surface-damage, all LPFs are equipped with anti-reflection-coated (and up to 5 mm thick) end-caps. Besides, circular polarization is applied during amplification using QWPs before and after the amplifiers, in order to reduce the SPM-induced pulse degradation [62]. Additionally, HWPs are required before the amplifiers to have sufficient degrees of freedom to compensate for NLPR (see Subsec. 2.4.2). After amplification, the eight beams are spatially combined in a setup similar to that used for the beam division but used in the reverse direction. In this stage Brewster-type thin-film polarizers[15] (TFPs) with $T_p > 0.99$ and $R_s > 0.999$ are employed [127], because they provide high polarization contrast, less material and, thus, less heating than PBS cubes. In a first step, the sub-beams within each main branch are combined. HC detection (Sec. 4.1) is employed to actively stabilize the two blocks of four amplifiers. Next, the two combined beams from both branches are superposed into a single beam containing the amplified burst with the initial polarization pattern. The beam is then enlarged to a diameter of 8 mm in order to reduce divergence and ensure high temporal stacking efficiency (see Fig. 5.5d). Therefore, two-inch diameter optical components are employed for pulse stacking. A HWP rotates the polarization pattern of the burst by 90°. Then, the burst is stacked in back-reflection-

---

[15]Please note that the TFPs are optimized for 56° incidence, which for simplicity is sketched for 45° in Fig. 5.13.

free delay lines employing Brewster-type TFPs. Both temporal stacking steps as well as the last spatial combination step are stabilized via LOCSET (Sec. 4.2). The signal for the stabilization electronics is obtained from a leak in the mirror placed after the final TFP (a laser window, as sketched in Fig. 5.13 for clarity, can be used alternatively). The retrieval of the error signals is achieved by the piezo modulation frequencies $f_1 = 2\,\text{kHz}$, $f_2 = 3\,\text{kHz}$ and $f_3 = 4.3\,\text{kHz}$ with modulation depths of approximately $\beta = 0.1$. Besides, temporal gating of the acquired photo-diode signal is also employed (Subsec. 5.2.3) to suppress undesired multi-stable operation. In this experiment, a fiber-coupled electro-optic amplitude modulator with $12\,\text{GHz}$ bandwidth and 30dB extinction ratio is set as a fast switch in front of the photo-diode. The rectangular window function (with $4\,\text{ns}$ width) and the electronic delay are provided by a waveform generator that is triggered with the initial clock signal. Finally, the combined pulse is compressed by a Treacy-type reflection-grating compressor [154], which has a transmission efficiency of 90%.

Experiment

In order to investigate the power- and energy-scaling capability of spatio-temporal combination, the number of pulse replicas and amplifier channels is step-wise increased. Therefore, the system is operated with one, two and four pulse replicas that are amplified in two, four and eight amplifier channels. Additionally, the total seed pulse energy is increased to increase the extracted energy from the amplifiers. The achieved combined and compressed pulse energies are shown in Fig. 5.14a, with the corresponding system efficiencies shown in Fig. 5.14b.

First, the system is operated only with single pulses that are amplified in two, four and eight amplifier channels without any temporal pulse division. While each amplifier operates at average powers between $110\,\text{W}$ and $120\,\text{W}$, the pulse energy is increased by decreasing the repetition rate from $1.06\,\text{MHz}$ to $208\,\text{kHz}$. The stacked pulse energies after compression are shown in Fig. 5.14a marked as circles. By the spatial combination of two, four and eight amplifier channels a maximum compressed pulse energy of $1.0\,\text{mJ}$, $1.9\,\text{mJ}$ and $3.7\,\text{mJ}$, corresponding to average powers of $206\,\text{W}$, $389\,\text{W}$ and $775\,\text{W}$, has been achieved, respectively. In Fig. 5.14b the system efficiency is depicted. It can be seen that this parameter is between 98% and 90% even for the maximum pulse energy. Damage has been observed at a single-pulse energy of about $900\,\text{µJ}$ at the fiber output, which is in the order of the saturation energy (that is estimated to be $E_{\text{sat}} = 1\,\text{mJ}$). The expected damage threshold according to Eq. (2.30) is $\sim 3\,\text{mJ}$ when considering the end-cap and $\sim 900\,\text{µJ}$ without. In spite of this, damage occurred within the end-cap, even though the maximum peak power was about five times below the critical self-focusing
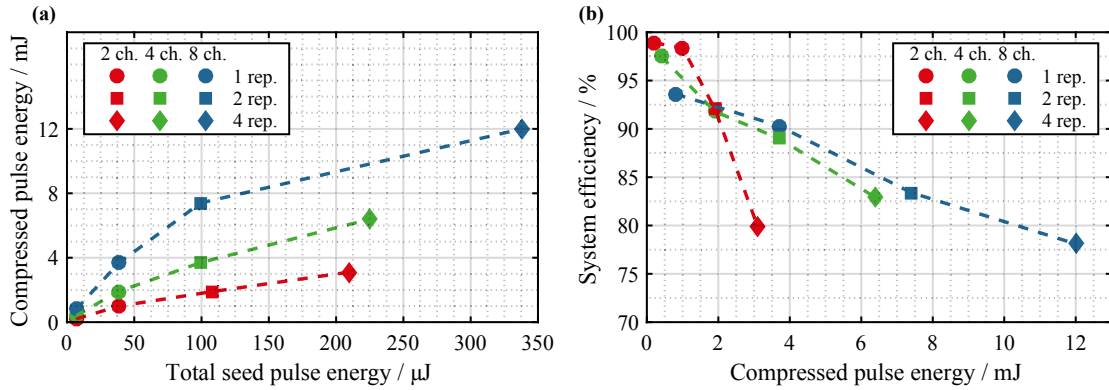
Figure 5.14.: (a) Stacked and compressed pulse energy as a function of the total seed pulse energy and (b) the corresponding system efficiencies for the combination of two (red), four (green) and eight (blue) amplifier channels operated with one (circles), two (squares) and four (diamonds) pulse replicas (dashed lines are for the guidance of the eye).

limit. The cause of this damage is yet unknown and is currently being investigated. At the achieved combined energies, the amplifiers were not operated at their limits, keeping the pulse energy at the fiber output around $600\,\mu$J. The decrease in efficiency with an increasing number of combined channels is mainly attributed to a non-perfect beam-parameter matching (Subsec. 3.1.3). Nevertheless, an almost linear energy-scaling with the number of channels can be seen and the system output is more than four times above the damage threshold of a single pulse in a single fiber.

Next, the HWPs of the delay lines for pulse division and stacking have been adjusted to generate a burst of two pulse replicas. This configuration allowed decreasing the repetition rate further to $99.6\,$kHz in order to extract more energy from the amplifiers while maintaining the average power constant. At higher pulse energies the amplifiers start to saturate, making a shaping of the envelope of the burst necessary to match their nonlinear phases (Subsec. 3.2.3). Furthermore, the onset of NLPR (see Subsec. 2.4.2) during amplification becomes noticeable as a reduced power transmission at the subsequent TFPs. This is compensated for with the HWP-QWP combination in front of each amplifier. Since this effect manifests itself with different strength in each individual fiber and since the exact evolution of the polarization state and, thus, the overall accumulated nonlinear phase is unknown, the compressed powers of the amplifiers are slightly adjusted to obtain the shortest autocorrelations (Subsec. 3.1.3). NLPR affects each pulse replica differently, due to the different pulse energy, which leads to a not compensable power loss at the subsequent polarizing element, as described in Subsec. 5.1.2. Nevertheless, a compressed main-pulse energy of $1.9\,$mJ, $3.7\,$mJ and $7.4\,$mJ, corresponding to average powers of $200\,$W, $385\,$W and $758\,$W, for the combination of two, four and eight channels

has been achieved, respectively. These values are shown as squares in Fig. 5.14a with the corresponding system efficiencies ranging between 92% and 83% in Fig. 5.14b. This further drop in the efficiency can be attributed to NLPR and/or residual nonlinear phase mismatches between the pulse replicas as well as between the amplifier channels. The B-integral accumulated in each main amplifier, taking into account SPM, is estimated to be ~ 6 rad, which can potentially be even higher due to NLPR. In Fig. 5.15a-c the traces for the shaped input burst before spatial division, as well as the amplified burst after spatial combination and the stacked pulse before compression are shown for the highest pulse energy. The overall pulse energy at the fiber outputs is about 1.2 mJ, while 55% of it is contained in the first pulse, which is marked in Fig. 5.15b. The possible pre- and post-pulse positions around the stacked pulse are indicated in Fig. 5.15c by dashed lines. A magnified pre-pulse is shown in the inset, corresponding to a pulse contrast of $\mathcal{C} = 17$dB.

Finally, all four pulse replicas are used which allowed for a further increase of the pulse energy. A stacked and compressed main-pulse energy of 3.1 mJ, 6.4 mJ and 12 mJ, corresponding to average powers of 186 W, 380 W and 700 W, for the combination of two, four, and eight amplifier channels has been achieved at a repetition rate of 55.9 kHz, respectively. These values are depicted in Fig. 5.14a as diamonds. The maximum reached pulse energy is 13 times higher than the observed damage threshold for a single pulse in a single fiber. This performance level cannot be reached with conventional ultrafast
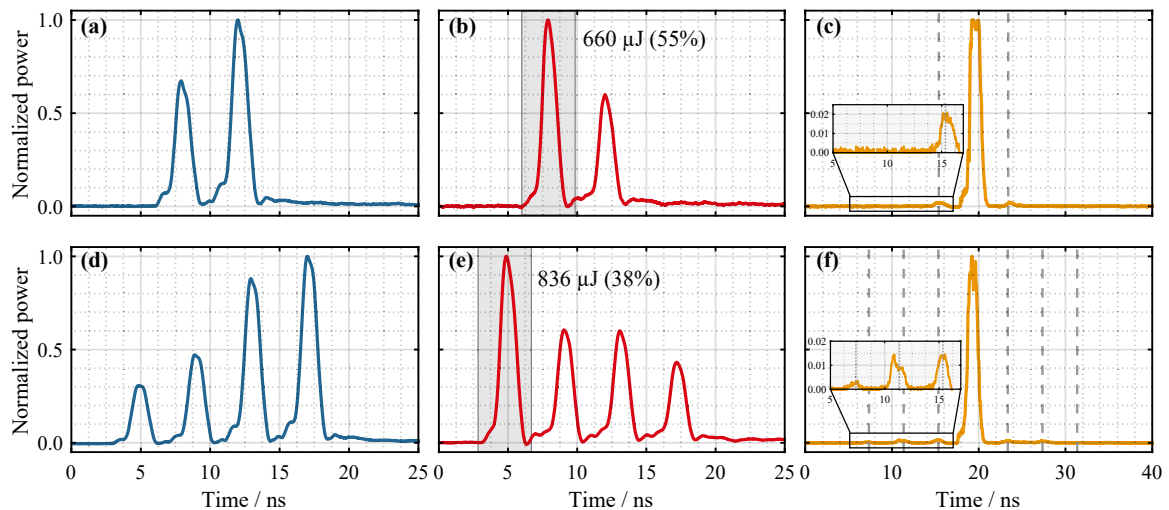

Figure 5.15.: Measured photo-diode traces at the maximum achieved pulse energy of the shaped input burst before spatial division, the amplified burst after spatial combination (< 1 ns rise-time photo-diode) and the stacked pulse before compression (< 18 ps photo-diode together with a 30 GS/s sampling scope) applying (a)-(c) a burst of two pulses and (d)-(f) a burst of four pulses together with eight amplifier channels. Possible pre- and post-pulse positions around the stacked pulses shown in (c) and (f) are indicated by dashed lines.

fiber-amplifier systems [61]. The corresponding system efficiencies are between 83% and 78%, as shown in Fig. 5.14b, with an estimated B-integral of ~ 6.5 rad. Generally, the pulse energy scales almost linearly with the number of amplifier channels independently from the burst length. However, due to the required burst-envelope shaping, the pulse energy does not scale linearly with the number of pulse replicas within the burst. The measured traces for the input and the amplified burst as well as for the stacked pulse are shown for the case of 12 mJ in Fig. 5.15d-f. The total burst energy at the fiber outputs is 2.2 mJ, corresponding to $E/E_{\text{sat}} = 2.2$, which is also more than two times larger than the damage energy[16]. However, the energy could not be further increased, since about 38% of it is contained in the first pulse, as shown in Fig. 5.15b, which is very close to the observed damage threshold. The pulse contrast is $\mathcal{C} = 19$dB with the possible pre- and post-pulse positions being indicated by dashed lines in Fig. 5.15f.

The spectrum of the compressed pulse at 12 mJ is shown in Fig. 5.16a. While the hard-cut at about 1040 nm is caused by the aperture of the grating in the stretcher/compressor,
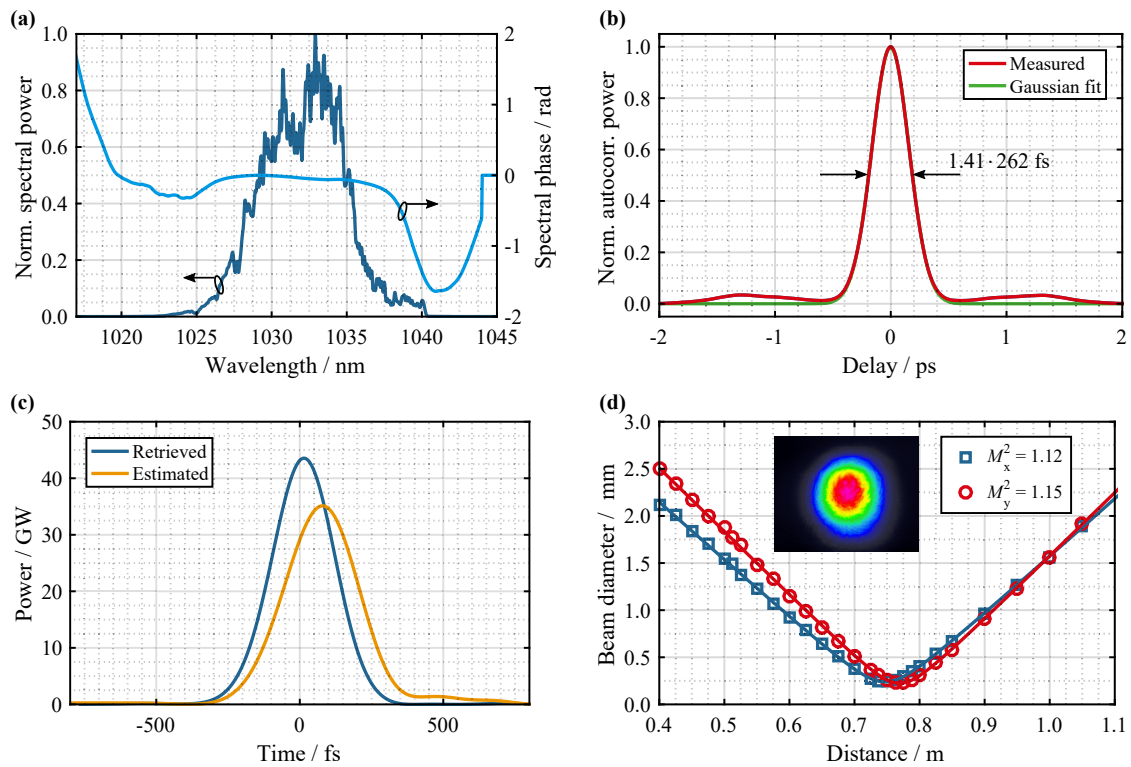

Figure 5.16.: (a) Measured spectrum and residual spectral phase, (b) autocorrelation with Gaussian fit, (c) retrieved and estimated pulse, and (d) M^2 measurement at the maximum pulse energy of 12 mJ (the beam profile is shown in the inset).

---

[16]The theoretical maximum extractable energy per fiber is estimated to be ~ 8.5 mJ (according to Eq. (2.28)).

the spectral modulation originates from the pixel mask (128) of the SLM covering a bandwidth of 25 nm. This causes a weak initial spectral modulation with a period of ~ 0.2 nm, which make side-pulses arising. SPM causes an energy transfer between these side-pulses and the main pulse, that is enhanced during amplification [160]. The measured autocorrelation is shown in Fig. 5.16b having a duration of 370 fs, which corresponds to a pulse duration of 262 fs assuming a Gaussian pulse. Using the residual spectral phase obtained from the MIIPS algorithm, which is additionally depicted in Fig. 5.16a, and the spectrum, the temporal pulse can be retrieved, which is shown in Fig. 5.16c. From this, a pulse duration of 255 fs has been achieved, with a peak power of 43 GW. However, in order to protect the laser system from damage, the MIIPS procedure was run only with a single amplifier channel in operation. Thus, the exact phase of the overall combined output can differ from that shown in Fig. 5.16a. Estimating the amount of spectral phase required to fit the shape of the measured autocorrelation trace revealed a peak power of 35 GW and a pulse duration of 298 fs. The corresponding pulse is additionally depicted in Fig. 5.16c (in orange). In either case this represents the highest peak power and pulse energy achieved with a fiber-based femtosecond laser system to date. Finally, the beam quality has been measured. After compression, the onset of self-focusing in air due to the high peak intensities has been observed which degrades the beam quality. Therefore, a weak power fraction from the output of the compressor has been used for the diagnostics. As a future improvement, this issue can be solved by increasing the beam diameter or by doing the compression and potential beam delivery for applications in vacuum. In any case, the M^2 measurement [50] from the weak reflection confirmed the excellent beam quality ($M^2 < 1.15$) delivered by the laser system, which is shown in Fig. 5.16d with the far-field beam profile also shown in the inset.

5.3. Future Perspectives

The energy extraction from an amplifier can be increased using DPA, which has been demonstrated with the experiments presented in the previous sections. In terms of further energy scaling with this approach, however, it is necessary to optimize the number of pulse replicas, which will be considered in this last section. While, on the one hand, the minimum number of pulse replicas necessary is determined by physical limitations, such as damage, the maximum number, on the other hand, is determined by practical limitations, such as losses that can be accumulated due to a large number of optical elements. Because of the latter, typically, the number of pulse replicas is tried to keep as low as possible. Since the performance of a particular amplifier system depends on a variety of parameters,

the discussion in the following will be restricted to the energy and extraction efficiency in combination with the system efficiency, B-integral and damage, which represent the main constraints. This analysis will be illustrated with the help of an example related to the final experiment.

The first focus of the analysis is on energy extraction. For this, the extraction efficiency can be considered as a measure of the energy yield related to the input energy for a particular amplifier. In order to get all of the extractable energy out of the amplifier, an infinitely high input energy ($E_0 \gg E_{sat}$) is necessary. However, from a certain input energy upwards, the extraction efficiency converges quite slowly towards its maximum, i.e. the ratio between the energy extraction and the input energy becomes unprofitable from a practical point of view. As an illustration, the extraction efficiency η_{extr} (Eq. (2.29)) is shown in Fig. 5.17a as a function of the input energy E_0 normalized to the saturation energy E_{sat} for a small-signal gain of $G_0 = 30$dB. It can be seen from the figure that, as η_{extr} increases, the slope saturates. Therefore, the slope of η_{extr} as a function of E_0/E_{sat} can be used as a general parameter to identify the most profitable operation point for a certain amplifier layout. Using Eq. (2.26) and Eq. (2.29), this slope parameter can be defined as

$$\zeta = \frac{\partial \eta_{extr}}{\partial \left(\frac{E_0}{E_{sat}} \right)} = \frac{1}{\ln(G_0)} \left\{ \frac{G_0 \exp\left(\frac{E_0}{E_{sat}} \right)}{1 + G_0 \left[\exp\left(\frac{E_0}{E_{sat}} \right) - 1 \right]} - 1 \right\}, \tag{5.7}$$

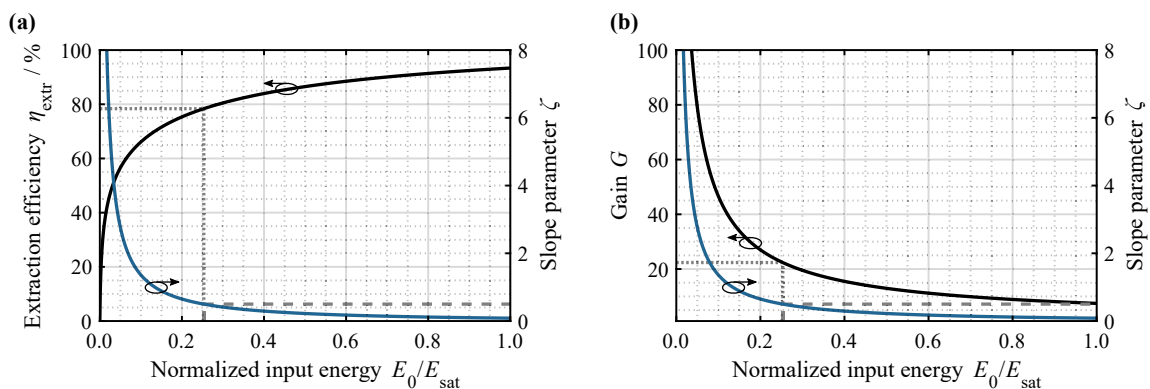which is additionally shown in Fig. 5.17a (in blue). The slope parameter ζ describes the

Figure 5.17.: (a) Extraction efficiency η_{extr} and (b) gain G as a function of the input pulse energy E_0 normalized to the saturation energy E_{sat} for a small-signal gain $G_0 = 30$dB. The slope parameter ζ is shown in both plots with E_0/E_{sat} corresponding to $\zeta = 0.5$ being marked by dashed lines and with η_{extr} and G corresponding to E_0/E_{sat} being marked by dotted lines.

resulting change in extraction efficiency (or in output energy) to small changes of the input energy. For example, for values of $\zeta > 2$ the extraction efficiency is very sensitive to changes of the input energy, which corresponds to high-gain operation. The related gain G according to Eq. (2.27) is shown in Fig. 5.17b. Despite a high gain, for a low input energy the extraction efficiency and, thus, the output energy are low. For $\zeta < 1$ the extraction efficiency becomes more and more insensitive to a change (increase) of the input energy. At some point it becomes impractical to further increase the input signal energy, because this change does not lead to any significant variation of η_{extr} anymore. Thus, with the choice of ζ, a practical operation point for an amplifier with a given G_0 can be set. Please note that such an optimum operation condition is strongly dependent on the application. Solving Eq. (5.7) for E_0/E_{sat} results in the input energy required to obtain the optimum η_{extr}:

$$\frac{E_0}{E_{\text{sat}}}(\zeta) = \ln\left\{\frac{[\zeta \ln(G_0) + 1]}{\zeta \ln(G_0)}\frac{(G_0 - 1)}{G_0}\right\}. \tag{5.8}$$

Plugging Eq. (5.8) into Eq. (2.29) gives the corresponding extraction efficiency

$$\eta_{\text{extr}}(\zeta) = 1 - \frac{\ln[\zeta \ln(G_0) + 1]}{\ln(G_0)} \tag{5.9}$$

and, using additionally Eqs. (2.26) and (2.27), the output energy

$$\frac{E}{E_{\text{sat}}}(\zeta) = \ln\left[\frac{G_0 - 1}{\zeta \ln(G_0)}\right]. \tag{5.10}$$

As an example, $\zeta = 0.5$ will be assumed as the most profitable operation point of the system, which is marked in Fig. 5.17a and Fig. 5.17b by dashed lines. Hence, looking at the illustration above ($G_0 = 30$dB) this slope parameter will be obtained with an input energy of $E_0 \approx 0.25 E_{\text{sat}}$, which corresponds to an output energy of $E \approx 5.7 E_{\text{sat}}$ and an extraction efficiency of $\eta_{\text{extr}} \approx 78\%$. This is additionally indicated in Fig. 5.17a and Fig. 5.17b by dotted lines. In this case, the gain remains $G > 20$, which is still an acceptable performance for high-power fiber amplifiers in most situations.

These considerations can be applied to the main fiber-amplifiers used in the final experiment presented in Subsec. 5.2.4. In that example, with an input energy of $\sim 43\,\mu\text{J}$ (per channel) an output of $2.2\,\text{mJ}$ has been achieved. The theoretically estimated maximum

small-signal gain[17] of this particular fiber is $\sim 36.8\,\text{dB}$ (assuming sufficient pump power at $976\,\text{nm}$). According to Eq. (2.28), this corresponds to a maximum extractable energy of $E_{\text{extr}}^{\text{max}} \approx 8.5\,\text{mJ}$ ($E_{\text{sat}} = 1\,\text{mJ}$). Setting $\zeta = 0.5$ results in a required input energy of $E_0 \approx 210\,\text{µJ}$ in order to achieve $E \approx 7\,\text{mJ}$ at the fiber output with $\eta_{\text{extr}} \approx 80\%$. It is worth noting, however, that G_0 depends on the energy being deposited in the amplifier by the pump laser. Thus, the pump rate (i.e the average power) and the energy-extraction rate (being related to the repetition rate) determine $E_{\text{extr}}^{\text{max}}$. With the currently applied pump power of $250\,\text{W}$ (per channel), the repetition rate would have to be decreased[18] to $f_{\text{rep}} = 15\,\text{kHz}$ to achieve $E \approx 7\,\text{mJ}$. Please note that more than $16\,\text{mJ}$ could be extractable when pumping at $915\,\text{nm}$, but this, due to the low pump absorption, would require more than twice as much pump power when keeping the fiber parameters unchanged.

In order to operate the fiber amplifier at $7\,\text{mJ}$, both the material damage and the accumulated nonlinearity have to be taken into account. On the one hand, the damage threshold of a single pulse (whether in terms of peak power or pulse energy) determines the minimum number of pulse divisions necessary. On the other hand, the accumulated nonlinearity determines the quality of the compressed pulse, which is additionally related to the number of pulse divisions. Furthermore, saturation-induced intra-pulse deformation and, related to it, nonlinear-phase variations among the pulse replicas are reduced when using more pulse divisions, which affects the combination efficiency of the pulses. The accumulated nonlinearity is represented by the B-integral and depends on the evolution of the peak power in the amplifier and, thus, on the pulse shape. For the example considered here Gaussian-shaped pulses are assumed. Moreover, a phase-compensation device (phase-shaper) can be employed in practice to mitigate detrimental pulse degradation at high B-integrals. Depending on the ability of the device and according to the experimental experience, the B-integral should be kept, for example, below $\sim 10\,\text{rad}$ with and below $\sim 3\,\text{rad}$ without phase-shaper being applied, in order to avoid severe pulse distortions. Moreover, circular polarization can be used during amplification to further reduce the overall nonlinearity [62]. Please note that higher order effects such as NLPR[19] are not considered here. As an illustration of these considerations, some simulations[20]

---

[17]The theoretical maximum small-signal gain is obtained for a sufficiently high pump power ($\bar{P}_{\text{p}} \gg P_{\text{p,sat}}$, according to Subsec. 2.2.2) and results in $G_0^{\text{max}} = \exp\left\{\sigma(\omega_0)\Gamma_{\text{s}}\left[N_{2,\text{tr}}(\omega_{\text{p}}) - N_{2,\text{tr}}(\omega_0)\right]L\right\}$. The parameters $\lambda_{\text{s}} = 1028\,\text{nm}$ and a bandwidth of $\Delta\lambda_{\text{s}} \approx 6\,\text{nm}$, $\lambda_{\text{p}} = 976\,\text{nm}$, $L = 1.1\,\text{m}$, $\text{MFD} = 60\,\text{µm}$, $d_{\text{clad}} = 255\,\text{µm}$, $d_{\text{dop}} = 63\,\text{µm}$, $N_{\text{tot}} = 3 \cdot 10^{25}\,\text{m}^{-3}$ and the cross-sections shown in Fig. 2.1a (weighted average using a Gaussian spectrum) are assumed.

[18]For too low repetition rates, a phase stabilization using LOCSET may become unstable. In this case, temporally-gated HC detectors might be a solution.

[19]For example, neglecting NLPR would be a valid assumption for polarization-maintaining fibers.

[20]Dispersion is neglected for the simulations because it has a negligible impact for short fibers. On the other hand, SPM, the Frantz-Nodvik amplification model and burst-shaping optimization are included.

related to the fiber and the stretched pulse duration (1.3 ns) used for the final experiment explained in the previous section have been carried out. Using these parameters and keeping the total input energy (210 µJ) and, therefore, the total output energy (7 mJ) fixed, the number of pulse divisions K is progressively increased. When doing this, the system efficiency η_{sys}, the B-integral and the energy-damage threshold are plotted as a function of the number $M = 2^K$ of pulse replicas with $K = 1, 2, \ldots, 9$ pulse divisions. This is summarized in Fig. 5.18. For the case considered, the bursts are either shaped to match the B-integrals of the output pulse replicas (solid lines) or their amplitudes (dashed lines), which is discussed in the following.
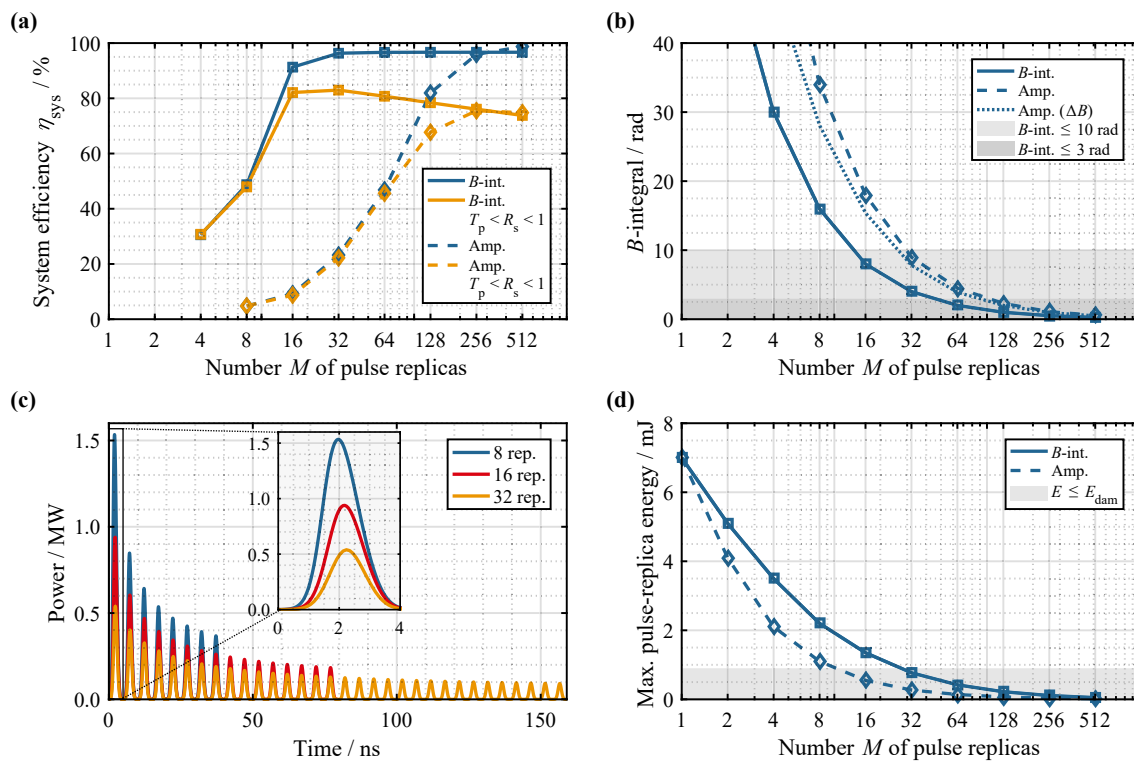
Figure 5.18.: (a) System efficiency η_{sys} as a function of the number M of pulse replicas (logarithmic scale) for an output energy of 7 mJ in the cases of matched B-integrals (solid lines) and matched amplitudes (dashed lines) of the amplified pulse replicas. PBSs with $T_{\text{p}} = R_{\text{s}} = 1$ are assumed (blue lines). Additionally, the impact of PBSs with $T_{\text{p}} = 0.98$ and $R_{\text{s}} = 0.99$ (orange lines) is shown. (b) Corresponding B-integral (i.e. the maximum within a burst) as a function of M. Additionally, the maximum B-integral difference between the pulse replicas (i.e. the first and the last replica) for the amplitude-matched case is shown as a dotted line. The B-integral limits of 10 rad and 3 rad are indicated by the light-grey and the darker grey shaded regions, respectively. (c) Amplified pulse bursts for 8, 16 and 32 pulse replicas in the B-integral-matched case. The intra-pulse deformation of the first pulses is shown as inset. (d) Corresponding energy of the first pulse replica within the burst (maximum) as a function of M. The energy below the damage threshold is indicated by the light-grey shaded region.

The resulting system efficiencies for both cases are shown in Fig. 5.18a (assuming ideal PBSs with $T_\mathrm{p} = R_\mathrm{s} = 1$). As can be seen, the system efficiency improves with an increasing number of pulse divisions. Moreover, while at least 128 pulse replicas are necessary for the amplitude-matched case in order to obtain $\eta_\mathrm{sys} > 80\%$, in the B-integral-matched case 16 pulse replicas are enough. The reason for this difference is the nonlinear-phase mismatch among the pulse replicas. To illustrate this, the corresponding B-integrals are shown in Fig. 5.18b. Associated with the increase in efficiency is an overall decrease of the nonlinearity. In the B-integral-matched case, $B < 10\,\mathrm{rad}$ is achieved with 16 pulse replicas (indicated by the light-grey shaded region), which also comes along with $\eta_\mathrm{sys} > 80\%$. If, for example, $B < 3\,\mathrm{rad}$ is required (indicated by the darker grey shaded region), 64 pulse replicas will be necessary. Although in the amplitude-matched case with 32 pulse replicas $B < 10\,\mathrm{rad}$ is obtained, at least 128 pulse replicas are required to keep $\eta_\mathrm{sys} > 80\%$ (and, according to Subsec. 3.1.3 Fig. 3.7b, B-integral differences $\Delta B \lesssim 3\,\mathrm{rad}$, indicated by the dotted line in Fig. 5.18b).

On top on this, fiber damage has to be considered. The experimentally observed damage threshold for a pulse replica was[21] $\sim 900\,\mathrm{µJ}$ (see Subsec. 5.2.4). While in the amplitude-matched case all pulse replicas possess an identical pulse energy, in the B-integral-matched case the amplified burst envelope decreases in amplitude (which is shown in Fig. 5.18c for the cases of 8, 16 and 32 pulse replicas). Thus, the first pulse contains more energy compared to the remaining pulses. In Fig. 5.18d this maximum energy of the first pulse is depicted for both cases as a function of M. It can be seen that matching the amplitudes allows going below the damage threshold (indicated by the light-grey shaded region) with only 16 pulse replicas, whereas at least 32 pulse replicas are required when the B-integrals are matched to obtain the minimum number of pulses required for a system. Thus, considering the efficiency and the level of nonlinearity alone is not sufficient in terms of the B-integral-matched case.

As can be seen from Fig. 5.18a, the system efficiency increases with increasing M for both the B-integral-matched case and the amplitude-matched case. However, a large number of delay lines have to be used in the latter case. In practice, this can lead to alignment mismatches that can accumulate losses upon the pulse stacking, in turn, degrading the system efficiency (and the pulse contrast). The drawbacks of a high M become obvious considering the losses that can be introduced by the quality of the PBSs for a power reflectance and a transmittance of $T_\mathrm{p} < R_\mathrm{s} < 1$. As an illustration of this, the impact on the system efficiency is indicated in Fig. 5.18a by orange lines, assuming $T_\mathrm{p} = 0.98$ and $T_\mathrm{p} = 0.99$. It can be seen that the maximum achievable system efficiency

---

[21]The damage threshold, of course, will change for different system parameters.

is decreased and drops further with an increasing number of delay lines. Comparing both cases, in this regard a higher efficiency can be achieved by matching the B-integrals while simultaneously using a much lower number of pulse replicas. From the analysis it can be concluded that for a system, with the parameters considered above, 32 pulse replicas will be required in the B-integral-matched case to obtain 7 mJ from the main fiber-amplifier.

It is worth noting that potentially a higher pulse contrast will be achieved in the amplitude-matched case using much more pulse replicas, if the pulse contrast is an important requirement for a particular application. However, the pulse contrast is improved at the expense of efficiency. Thus, there is potentially an optimum between both cases[22].

In terms of further scaling, the requirements for > 10 mJ from a fiber can be extrapolated. On the one hand, this can be achieved by increasing the fiber length. But this would tremendously increase the B-integral and would, again, require more pulse divisions. On the other hand, to increase the extractable energy the core diameter[23] of the fiber can be scaled. For example, doubling the extractable energy being considered to 14 mJ can be achieved by increasing the core size by a factor of $\sqrt{2}$ (while keeping Γ_s and Γ_p constant), since $E_{\mathrm{extr}}^{\mathrm{max}} \sim L \sim d_{\mathrm{dop}}^2$. Since both the overall energy (and, thus, the energy contained in the first pulse) and the damage threshold are linearly increased with the core area, in first order approximation, no further pulse divisions are necessary. In addition, the stretched pulse duration could be increased[24] to ~ 4 ns to reduce the number of pulse replicas to 16. Finally, employing additionally spatial combination using ten channels (assuming a total efficiency of 80%) will make a > 100 mJ kW-average-power fiber-laser system feasible in the near future.

Spatio-temporal combination systems may become rather complex as their complexity scales with the number of temporal and spatial combination channels, bringing integrated designs in the spotlight. A recent development is electro-optically controlled DPA [161], where the pulse division is circumvented by employing a high-repetition-rate oscillator in combination with an AOM for the burst generation. Using a two-channel operation and electro-optic modulators (EOMs), the polarization pattern required to stack the pulse replicas with delay lines is achieved by imprinting a particular phase pattern on the bursts prior to their orthogonal superposition. Additionally, these EOMs can also be used for the above mentioned phase correction of the individual pulses, in order to compensate for B-integral mismatches in the amplitude-matched case. On a different account, imaging

---

[22]Please note that the algorithm optimizes for either matched amplitudes or (maximum) B-integrals.

[23]Actually the doped-core diameter, but both the doped core diameter and the core diameter usually scale linearly with each other.

[24]For example, exploiting the full bandwidth of the grating used in the experiments by pre-compensating gain narrowing via pulse-envelope shaping can increase the stretched pulse duration potentially from 1.3 ns to ~ 4 ns for a rectangular pulse envelope.

multi-pass cells, such as Herriott cells [162], can be employed for compact and efficient pulse stacking of long delays. Alternatively, if a large number of pulse replicas ($M \gtrsim 32$) is necessary, cavity approaches will be an interesting choice [111, 114, 163–166]. On the other hand, in terms of spatial combination, multicore-fibers can be employed to integrate tens of amplifier channels in a single fiber [167]. Ultimately, the integration of spatio-temporal combination to advanced and compact fiber-laser designs will bring table-top systems delivering tens of kW of average power together with J-class pulse energy within reach.

6. Conclusion

There are already laser applications that demand a combination of performance parameters that is beyond what established laser concepts can currently fulfill. In particular, thermal and nonlinear effects constitute the main challenges, hindering the simultaneous generation of both high average power and high peak power. Even though state-of-the-art scaling approaches, such as increasing the beam size and the stretched pulse duration during amplification enable significant improvements in either respect, the tighter technological requirements restrict the near-future scaling expectations. The need for alternative power-scaling concepts led to the technique of coherent combination of ultrashort pulses [29], which is the topic of this thesis. In this regard, a distinction has to be made between spatially and temporally separated amplification. Hereby, the former leads to a scaling of both the average power and the pulse energy while maintaining all other pulse- and beam-parameters unchanged [136]. However, even though fibers have a very high average-power capability, the pulse energy that can be extracted from them is fairly low and, therefore, a large number of channels is required for the targeted energy-levels. Thus, temporally separated amplification, also referred to as divided-pulse amplification (DPA) [30–32], is considered to scale exclusively the extracted energy from an amplifier. DPA represents the core of this work.

Therefore, pulse-burst generation and pulse stacking based on polarization-sensitive optical delay lines [30, 31], consisting of half-wave plates (HWPs) and polarizing beam splitters (PBSs), has been studied. These delay lines are applicable to stretched pulses and high-energy operation. It has been shown that the polarization purity provided by the PBSs and the alignment precision of the HWPs results in an unbalanced energy distribution between orthogonally-polarized components of the divided pulse replicas. In contrast to spatial combination, pulse energy in unexpected polarization components gets further distributed in the form of pre- and post-pulses surrounding the desired main stacked pulse. This, in turn, degrades the intrinsic pulse contrast and stacking efficiency [131].

The amplification of bursts leads to a saturation-induced deformation of their envelope, which causes an amplitude and nonlinear-phase mismatch among the pulse replicas. It has been demonstrated that in this amplification regime passively stable Sagnac-type

implementations [38, 121] only work for the case of two pulse replicas [138]. The symmetry requirements both for pulse division and stacking as well as the limited number of degrees of freedom for burst shaping lead to a significant drop in the combination efficiency for more than two pulse replicas when operating in saturation [131]. Therefore, active DPA (aDPA) [140] has been introduced, which separates the pulse division from the stacking and allows treating both stages independently. In this respect, burst-shaping strategies have been investigated and it has been shown that the non-matched nonlinear phases of the pulse replicas have a more detrimental effect on the stacking efficiency than non-matched pulse amplitudes. In a first experimental demonstration employing a burst of four stretched pulse replicas, a pulse energy of 2.4 mJ has been achieved from a single fiber, with a peak power of the stacked pulse close to 3 GW after compression [140]. This has been scaled to 6.5 mJ demonstrating the ability of DPA to extract the energy stored in the fiber. An energy-dependent decrease in efficiency has been observed in these demonstrations, which is mainly attributed to residual nonlinear phase mismatches and nonlinear polarization rotation.

In a first demonstration of actively-stabilized spatio-temporal combination, both spatial and temporal combination concepts have been merged in a scalable architecture [141]. A multi-stable operation behavior of the temporal and spatio-temporal combination implementations using single-detector-based phase-stabilization techniques has been discovered and analyzed. As a solution, temporal gating of the signal acquisition has been introduced to suppress undesired stabilization states and allowing for long-term stable operation [158]. Finally, a state-of-the-art fiber-based chirped-pulse-amplification (CPA) system has been redesigned and extended by spatio-temporal combination employing eight parallel main amplifiers in which bursts of up to four stretched pulse replicas are amplified. This allowed for < 300 fs pulses with an energy of 12 mJ, corresponding to a peak power in excess of ~ 35 GW, at an average power of 700 W after pulse stacking and compression [142]. This is the highest pulse energy (or peak power) from fiber-based systems so far, which is beyond what is possible today with conventional ultrafast fiber-amplifier systems [61]. More importantly, this result represents an unprecedented combination of pulse energy and average power delivered by a solid-state laser. Besides a good system efficiency, a pulse contrast of 19dB has also been achieved. In order to further improve the pulse contrast, as required for high-intensity laser experiments, peak-power-sensitive post-processes, such as nonlinear pulse compression [132], could potentially be used, but this possibility will have to be further investigated in future works.

In terms of further scaling, some perspectives of DPA are given. It has been shown that with an increased seed pulse energy and pump power, a pulse energy of 7 mJ can

be achieved (with 32 pulse replicas and the currently employed stretched pulse duration) from each main-amplifier fiber. Even 14 mJ seem feasible with only 16 pulse replicas, but it would require an increased stretching ratio, amplitude shaping and larger-core fibers. Eventually, DPA constitutes a viable scaling approach in addition to state-of-the-art CPA, with which pulse-energy improvements in the order of one magnitude can be achieved. Furthermore, DPA is not limited to fibers and has also found application for other solid-state amplifier concepts [35, 36, 155, 168] and oscillators [169].

In a different context, nonlinear pulse compression [132] in gas-filled hollow-core fibers has become a viable post-process providing high peak-power, high-repetition-rate few-cycle laser pulses [170] to fulfill the demanding requirements, for example for high-harmonic generation [6–8] and, directly linked to it, the generation of attosecond pulses [4]. The concepts of spatial combination [171] and temporal combination [172–174] have also been applied to nonlinear pulse compression to prevent ionization or self-focusing in the nonlinear medium.

In order to keep the complexity of spatio-temporal-combination systems manageable, and their footprint and cost moderate, integrated designs are of interest for future laser systems. For example, with electro-optically controlled DPA [161] the pulse-division stage becomes redundant. As the number of pulse replicas to be stacked and the required delay-line lengths increase further, Herriott cells [162] for compact pulse stacking can be employed. For a large number of pulse replicas, cavity approaches might be an alternative concept [111, 114, 163–166]. Furthermore, the dimensions for spatially separated amplification can be reduced tremendously by employing multicore-fibers [167].

Envisioning all these conceptual techniques, spatio-temporal combination constitutes a promising concept for the next generation of table-top high peak- and average-power laser systems. Exploiting the advantages of fibers, femtosecond ($> 100\,\text{fs}$) laser systems delivering tens of kW average power with J-class pulse energy and diffraction-limited beam quality ($M^2 < 1.1$) are feasible in the near future.

Bibliography

[1] K. Sugioka and Y. Cheng, "Ultrafast lasers – reliable tools for advanced materials processing," Light Sci. Appl. **3**, e149 (2014).

[2] W. Sibbett, A. A. Lagatsky, and C. T. A. Brown, "The development and application of femtosecond laser systems," Opt. Express **20**, 6989–7001 (2012).

[3] W. P. Leemans, B. Nagler, A. J. Gonsalves, C. Tóth, K. Nakamura, C. G. R. Geddes, E. Esarey, C. B. Schroeder, and S. M. Hooker, "GeV electron beams from a centimetre-scale accelerator," Nat. Phys. **2**, 696–699 (2006).

[4] M. Krebs, S. Hädrich, S. Demmler, J. Rothhardt, A. Zaïr, L. Chipperfield, J. Limpert, and A. Tünnermann, "Towards isolated attosecond pulses at megahertz repetition rates," Nat. Photonics **7**, 555–559 (2013).

[5] G. K. Tadesse, R. Klas, S. Demmler, S. Hädrich, I. Wahyutama, M. Steinert, C. Spielmann, M. Zürch, T. Pertsch, A. Tünnermann, J. Limpert, and J. Rothhardt, "High speed and high resolution table-top nanoscale imaging," Opt. Lett. **41**, 5170–5173 (2016).

[6] A. McPherson, G. Gibson, H. Jara, U. Johann, T. S. Luk, I. A. McIntyre, K. Boyer, and C. K. Rhodes, "Studies of multiphoton production of vacuum-ultraviolet radiation in the rare gases," J. Opt. Soc. Am. B **4**, 595–601 (1987).

[7] M. Ferray, A. L'Huillier, X. F. Li, L. A. Lompre, G. Mainfray, and C. Manus, "Multiple-harmonic conversion of 1064 nm radiation in rare gases," J. Phys. B At. Mol. Opt. Phys. **21**, L31–L35 (1988).

[8] S. Hädrich, A. Klenke, J. Rothhardt, M. Krebs, A. Hoffmann, O. Pronin, V. Pervak, J. Limpert, and A. Tünnermann, "High photon flux table-top coherent extreme ultraviolet source," Nat. Photonics **8**, 779–783 (2014).

[9] F. Krausz and M. Ivanov, "Attosecond physics," Rev. Mod. Phys. **81**, 163–234 (2009).

[10] T. Tajima and J. M. Dawson, "Laser electron accelerator," Phys. Rev. Lett. **43**, 267–270 (1979).

[11] V. Malka, J. Faure, Y. A. Gauduel, E. Lefebvre, A. Rousse, and K. T. Phuoc, "Principles and applications of compact laser-plasma accelerators," Nat. Phys. **4**, 447–453 (2008).

[12] W. Leemans, "White Paper of the ICFA-ICUIL Joint Task Force - High Power Laser Technology for Accelerators," ICFA Beam Dyn. Newsl. **56**, 11–88 (2011).

[13] S. Banerjee, P. D. Mason, K. Ertel, P. J. Phillips, M. de Vido, O. Chekhlov, M. Divoky, J. Pilar, J. Smith, T. Butcher, A. Lintern, S. Tomlinson, W. Shaikh, C. Hooker, A. Lucianetti, C. Hernandez-Gomez, T. Mocek, C. Edwards, and J. L. Collier, "100 J-level nanosecond pulsed diode pumped solid state laser," Opt. Lett. **41**, 2089–2092 (2016).

[14] M. Hornung, H. Liebetrau, S. Keppler, A. Kessler, M. Hellwing, F. Schorcht, G. A. Becker, M. Reuter, J. Polz, J. Körner, J. Hein, and M. C. Kaluza, "54 J pulses with 18 nm bandwidth from a diode-pumped chirped-pulse amplification laser system," Opt. Lett. **41**, 5413–5416 (2016).

[15] T. J. Yu, S. K. Lee, J. H. Sung, J. W. Yoon, T. M. Jeong, and J. Lee, "Generation of high-contrast, 30 fs, 1.5 PW laser pulses from chirped-pulse amplification Ti:sapphire laser," Opt. Express **20**, 10807–10815 (2012).

[16] Y. Chu, X. Liang, L. Yu, Y. Xu, L. Xu, L. Ma, X. Lu, Y. Liu, Y. Leng, R. Li, and Z. Xu, "High-contrast 2.0 Petawatt Ti:sapphire laser system," Opt. Express **21**, 29231–29239 (2013).

[17] Y. Chu, Z. Gan, X. Liang, L. Yu, X. Lu, C. Wang, X. Wang, L. Xu, H. Lu, D. Yin, Y. Leng, R. Li, and Z. Xu, "High-energy large-aperture Ti:sapphire amplifier for 5 PW laser pulses," Opt. Lett. **40**, 5011–5014 (2015).

[18] C. J. Saraceno, F. Emaury, O. H. Heckl, C. R. E. Baer, M. Hoffmann, C. Schriber, M. Golling, T. Südmeyer, and U. Keller, "275 W average output power from a femtosecond thin disk oscillator operated in a vacuum environment," Opt. Express **20**, 23535–23541 (2012).

[19] J.-P. Negel, A. Voss, M. Abdou Ahmed, D. Bauer, D. Sutter, A. Killi, T. Graf, and M. A. Ahmed, "1.1 kW average output power from a thin-disk multipass amplifier for ultrashort laser pulses," Opt. Lett. **38**, 5442–5445 (2013).

[20] P. Russbueldt, T. Mans, J. Weitenberg, H. D. Hoffmann, and R. Poprawe, "Compact diode-pumped 1.1 kW Yb:YAG Innoslab femtosecond amplifier," Opt. Lett. **35**, 4169–4171 (2010).

[21] T. Eidam, S. Hanf, E. Seise, T. V. Andersen, T. Gabler, C. Wirth, T. Schreiber, J. Limpert, and A. Tünnermann, "Femtosecond fiber CPA system emitting 830 W average output power," Opt. Lett. **35**, 94–96 (2010).

[22] H. J. Eichler, A. Haase, R. Menzel, and A. Siemoneit, "Thermal lensing and depolarization in a highly pumped Nd:YAG laser amplifier," J. Phys. D. Appl. Phys. **26**, 1884–1891 (1999).

[23] T. Eidam, C. Wirth, C. Jauregui, F. Stutzki, F. Jansen, H.-J. Otto, O. Schmidt, T. Schreiber, J. Limpert, and A. Tünnermann, "Experimental observations of the threshold-like onset of mode instabilities in high power fiber amplifiers," Opt. Express **19**, 13218–13224 (2011).

[24] A. V. Smith and J. J. Smith, "Mode instability in high power fiber amplifiers," Opt. Express **19**, 10180–10192 (2011).

[25] C. Jauregui, T. Eidam, H.-J. Otto, F. Stutzki, F. Jansen, J. Limpert, and A. Tünnermann, "Physical origin of mode instabilities in high-power fiber laser systems," Opt. Express **20**, 12912–12925 (2012).

[26] G. P. Agrawal, *Nonlinear Fiber Optics* (Academic Press, 2013), 5th ed.

[27] W. Koechner, *Solid-State Laser Engineering* (Springer, New York, 2006), 6th ed.

[28] D. Strickland and G. Mourou, "Compression of amplified chirped pulses," Opt. Commun. **56**, 219–221 (1985).

[29] E. Seise, A. Klenke, J. Limpert, and A. Tünnermann, "Coherent addition of fiber-amplified ultrashort laser pulses," Opt. Express **18**, 27827–27835 (2010).

[30] S. Szatmari and P. Simon, "Interferometric multiplexing scheme for excimer amplifiers," Opt. Commun. **98**, 181–192 (1993).

[31] S. Podleska, "Verfahren und Vorrichtung zum Strecken und Rekomprimieren von optischen Impulsen, insbesondere von Laserimpulsen hoher Intensität," DE Patent 102006060703A1 (2006).

[32] S. Zhou, F. W. Wise, and D. G. Ouzounov, "Divided-pulse amplification of ultrashort pulses," Opt. Lett. **32**, 871–873 (2007).

[33] S. N. Bagayev, V. E. Leshchenko, V. I. Trunov, E. V. Pestryakov, and S. A. Frolov, "Coherent combining of femtosecond pulses parametrically amplified in BBO crystals," Opt. Lett. **39**, 1517–1520 (2014).

[34] M. Kienel, M. Müller, S. Demmler, J. Rothhardt, A. Klenke, T. Eidam, J. Limpert, and A. Tünnermann, "Coherent beam combination of Yb:YAG single-crystal rod amplifiers," Opt. Lett. **39**, 3278–3281 (2014).

[35] J. Pouysegur, B. Weichelt, F. Guichard, Y. Zaouter, C. Hönninger, E. Mottay, F. Druon, and P. Georges, "Simple Yb:YAG femtosecond booster amplifier using divided-pulse amplification," Opt. Express **24**, 9896–9904 (2016).

[36] B. Webb, A. Azim, N. Bodnar, M. Chini, L. Shah, and M. Richardson, "Divided-pulse amplification to the joule level," Opt. Lett. **41**, 3106–3109 (2016).

[37] T. Eidam, J. Rothhardt, F. Stutzki, F. Jansen, S. Hädrich, H. Carstens, C. Jauregui, J. Limpert, and A. Tünnermann, "Fiber chirped-pulse amplification system emitting 3.8 GW peak power," Opt. Express **19**, 255–260 (2011).

[38] Y. Zaouter, F. Guichard, L. Daniault, M. Hanna, F. Morin, C. Hönninger, E. Mottay, F. Druon, and P. Georges, "Femtosecond fiber chirped- and divided-pulse amplification system," Opt. Lett. **38**, 106–108 (2013).

[39] E. Seise, A. Klenke, S. Breitkopf, J. Limpert, and A. Tünnermann, "88 W 0.5 mJ femtosecond laser pulses from two coherently combined fiber amplifiers," Opt. Lett. **36**, 3858–3860 (2011).

[40] A. Klenke, E. Seise, S. Demmler, J. Rothhardt, S. Breitkopf, J. Limpert, and A. Tünnermann, "Coherently-combined two channel femtosecond fiber CPA system producing 3 mJ pulse energy," Opt. Express **19**, 24280–24285 (2011).

[41] J. Limpert, F. Stutzki, F. Jansen, H.-J. Otto, T. Eidam, C. Jauregui, and A. Tünnermann, "Yb-doped large-pitch fibres: effective single-mode operation based on higher-order mode delocalisation," Light Sci. Appl. **1**, e8 (2012).

[42] R. Paschotta, J. Nilsson, A. Tropper, and D. Hanna, "Ytterbium-doped fiber amplifiers," IEEE J. Quantum Electron. **33**, 1049–1056 (1997).

[43] H. Pask, R. Carman, D. Hanna, A. Tropper, C. Mackechnie, P. Barber, and J. Dawes, "Ytterbium-doped silica fibre lasers: versatile sources for the 1-1.2 µm region," IEEE J. Sel. Top. Quantum Electron. **1**, 2–13 (1995).

[44] A. W. Snyder and J. D. Love, *Optical Waveguide Theory* (Kluwer Academic Publishers, Boston, 1983).

[45] C. J. Koester and E. Snitzer, "Amplification in a Fiber Laser," Appl. Opt. **3**, 1182–1186 (1964).

[46] P. Russell, "Photonic crystal fibers," Science **299**, 358–362 (2003).

[47] F. Stutzki, F. Jansen, H.-J. Otto, C. Jauregui, J. Limpert, and A. Tünnermann, "Designing advanced very-large-mode-area fibers for power scaling of fiber-laser systems," Optica **1**, 233–242 (2014).

[48] M. Born and E. Wolf, *Principles of Optics* (Cambridge University Press, 1999), 7th ed.

[49] A. E. Siegman, *Lasers* (University Science Books, 1986).

[50] ISO Standard 11146, "Lasers and laser related equipment: Test methods for laser beam widths, divergence angles and beam propagation ratios," (2005).

[51] A. Hardy and R. Oron, "Signal amplification in strongly pumped fiber amplifiers," IEEE J. Quantum Electron. **33**, 307–313 (1997).

[52] Y. Wang and H. Po, "Dynamic Characteristics of Double-Clad Fiber Amplifiers for High-Power Pulse Amplification," IEEE J. Light. Technol. **21**, 2262–2270 (2003).

[53] T. Eidam, "Ultrashort-Pulse Fiber Amplifiers for High Peak and Average Powers," Ph.D. thesis, Friedrich-Schiller-Universität Jena (2012).

[54] W. H. Lowdermilk and J. E. Murray, "The multipass amplifier: Theory and numerical analysis," J. Appl. Phys. **51**, 2436–2444 (1980).

[55] L. M. Frantz and J. S. Nodvik, "Theory of pulse propagation in a laser amplifier," J. Appl. Phys. **34**, 2346–2349 (1963).

[56] D. N. Schimpf, "Pulse-shaping strategies in short-pulse fiber amplifiers," Ph.D. thesis, Friedrich-Schiller-Universität Jena (2009).

[57] J. Limpert, F. Röser, D. N. Schimpf, E. Seise, T. Eidam, S. Hädrich, J. Rothhardt, C. Jauregui Misas, and A. Tünnermann, "High Repetition Rate Gigawatt Peak Power Fiber Laser Systems: Challenges, Design, and Experiment," IEEE J. Sel. Top. Quantum Electron. **15**, 159–169 (2009).

[58] B. E. A. Saleh and M. C. Teich, *Fundamentals of Photonics* (Wiley-Interscience, Hoboken, 2007), 2nd ed.

[59] R. W. Boyd, *Nonlinear Optics* (Academic Press, 2008), 3rd ed.

[60] R. C. Jones, "A new calculus for the treatment of optical systems I. Description and discussion of the calculus," J. Opt. Soc. Am. **31**, 488–493 (1941).

[61] D. N. Schimpf, J. Limpert, and A. Tünnermann, "Optimization of high performance ultrafast fiber laser systems to >10 GW peak power," J. Opt. Soc. Am. B **27**, 2051–2060 (2010).

[62] D. N. Schimpf, T. Eidam, E. Seise, S. Hädrich, J. Limpert, and A. Tünnermann, "Circular versus linear polarization in laser-amplifiers with Kerr-nonlinearity," Opt. Express **17**, 18774–18781 (2009).

[63] M. D. Perry, T. Ditmire, and B. C. Stuart, "Self-phase modulation in chirped-pulse amplification," Opt. Lett. **19**, 2149–2151 (1994).

[64] R. L. Farrow, D. A. V. Kliner, G. R. Hadley, and A. V. Smith, "Peak-power limits on fiber amplifiers imposed by self-focusing," Opt. Lett. **31**, 3423–3425 (2006).

[65] M. N. Polyanskiy, "Refractive index database," http://refractiveindex.info, August 2016.

[66] P. D. Maker, R. W. Terhune, and C. M. Savage, "Intensity-Dependent Changes in the Refractive Index of Liquids," Phys. Rev. Lett. **12**, 507–509 (1964).

[67] R. H. Stolen, J. Botineau, and A. Ashkin, "Intensity discrimination of optical pulses with birefringent fibers," Opt. Lett. **7**, 512–514 (1982).

[68] B. Nikolaus, D. Grischkowsky, and A. C. Balant, "Optical pulse reshaping based on the nonlinear birefringence of single-mode optical fibers," Opt. Lett. **8**, 189–191 (1983).

[69] C. Vinegoni, M. Wegmuller, B. Huttner, and N. Gisin, "Measurement of nonlinear polarization rotation in a highly birefringent optical fibre using a Faraday mirror," J. Opt. A Pure Appl. Opt. **2**, 314–318 (2000).

[70] J. E. Ripper and T. L. Paoli, "Optical coupling of adjacent stripe-geometry junction lasers," Appl. Phys. Lett. **17**, 371–373 (1970).

[71] J. R. Leger, G. J. Swanson, and W. B. Veldkamp, "Coherent laser addition using binary phase gratings," Appl. Opt. **26**, 4391–4399 (1987).

[72] A. Klenke, "Performance scaling of laser amplifiers via coherent combination of ultrashort pulses," Ph.D. thesis, Friedrich-Schiller-Universität Jena (2016).

[73] S. J. Augst, A. K. Goyal, R. L. Aggarwal, T. Y. Fan, and A. Sanchez, "Wavelength beam combining of ytterbium fiber lasers," Opt. Lett. **28**, 331–333 (2003).

[74] S. Klingebiel, F. Röser, B. Ortaç, J. Limpert, and A. Tünnermann, "Spectral beam combining of Yb-doped fiber lasers with high efficiency," J. Opt. Soc. Am. B **24**, 1716–1720 (2007).

[75] T. Y. Fan, "Laser beam combining for high-power, high-radiance sources," IEEE J. Sel. Top. Quantum Electron. **11**, 567–577 (2005).

[76] T. Schreiber, C. Wirth, O. Schmidt, T. V. Andersen, I. Tsybin, S. Bahme, T. Peschel, F. Brackner, T. Clausnitzer, F. Raser, R. Eberhardt, J. Limpert, and A. Tannermann, "Incoherent beam combining of continuous-wave and pulsed Yb-Doped fiber amplifiers," IEEE J. Sel. Top. Quantum Electron. **15**, 354–360 (2009).

[77] C. Wirth, O. Schmidt, I. Tsybin, T. Schreiber, R. Eberhardt, J. Limpert, A. Tünnermann, K. Ludewigt, M. Gowin, E. ten Have, and M. Jung, "High average power spectral beam combining of four fiber amplifiers to 8.2 kW," Opt. Lett. **36**, 3118–3120 (2011).

[78] Y. Zheng, Y. Yang, J. Wang, M. Hu, G. Liu, X. Zhao, X. Chen, K. Liu, C. Zhao, B. He, and J. Zhou, "10.8 kW spectral beam combination of eight all-fiber superfluorescent sources and their dispersion compensation," Opt. Express **24**, 12063–12071 (2016).

[79] E. Shcherbakov, V. Fomin, A. Abramov, A. Ferin, D. Mochalov, and V. P. Gapontsev, "Industrial Grade 100 kW Power CW Fiber Laser," in "Adv. Solid-State Lasers Congr.", (Optical Society of America, 2013), p. ATh4A.2.

[80] Z. Chen, J. Hou, P. Zhou, X. Wang, X. Xu, Z. Jiang, and Z. Liu, "Mutual injection locking and coherent combining of three individual fiber lasers," Opt. Commun. **282**, 60–63 (2009).

[81] C. Corcoran and F. Durville, "Passive Phasing in a Coherent Laser Array," IEEE J. Sel. Top. Quantum Electron. **15**, 294–300 (2009).

[82] T.-W. Wu, W.-Z. Chang, A. Galvanauskas, and H. G. Winful, "Model for passive coherent beam combining in fiber laser arrays," Opt. Express **17**, 19509–19518 (2009).

[83] B. Wang, E. Mies, M. Minden, and A. Sanchez, "All-fiber 50 W coherently combined passive laser array," Opt. Lett. **34**, 863–865 (2009).

[84] M. Khajavikhan and J. R. Leger, "Modal Analysis of Path Length Sensitivity in Superposition Architectures for Coherent Laser Beam Combining," IEEE J. Sel. Top. Quantum Electron. **15**, 281–290 (2009).

[85] E. Ronen, A. A. Friesem, and N. Davidson, "Passive beam combining in compact slab lasers," IEEE J. Quantum Electron. **46**, 76–79 (2010).

[86] L. Daniault, M. Hanna, D. N. Papadopoulos, Y. Zaouter, E. Mottay, F. Druon, and P. Georges, "Passive coherent beam combining of two femtosecond fiber chirped-pulse amplifiers," Opt. Lett. **36**, 4023–4025 (2011).

[87] G. D. Goodno, H. Komine, S. J. McNaught, S. B. Weiss, S. Redmond, W. Long, R. Simpson, E. C. Cheung, D. Howland, P. Epp, M. Weber, M. McClellan, J. Sollee, and H. Injeyan, "Coherent combination of high-power, zigzag slab lasers," Opt. Lett. **31**, 1247–1249 (2006).

[88] E. Seise, A. Klenke, J. Limpert, and A. Tünnermann, "Coherent addition of fiber-amplified ultrashort laser pulses," Opt. Express **18**, 27827–27835 (2010).

[89] C. X. Yu, S. J. Augst, S. M. Redmond, K. C. Goldizen, D. V. Murphy, A. Sanchez, and T. Y. Fan, "Coherent combining of a 4 kW, eight-element fiber amplifier array," Opt. Lett. **36**, 2686–2688 (2011).

[90] L. Daniault, M. Hanna, L. Lombard, Y. Zaouter, E. Mottay, D. Goular, P. Bourdon, F. Druon, and P. Georges, "Coherent beam combining of two femtosecond fiber chirped-pulse amplifiers," Opt. Lett. **36**, 621–623 (2011).

[91] S. J. Augst, T. Y. Fan, and A. Sanchez, "Coherent beam combining and phase noise measurements of ytterbium fiber amplifiers," Opt. Lett. **29**, 474–476 (2004).

[92] X. Wang, J. Leng, P. Zhou, Y. Ma, X. Xu, and Z. Liu, "1.8-kW simultaneous spectral and coherent combining of three-tone nine-channel all-fiber amplifier array," Appl. Phys. B **107**, 785–790 (2012).

[93] S. J. McNaught, P. A. Thielen, L. N. Adams, J. G. Ho, A. M. Johnson, J. P. Machan, J. E. Rothenberg, C.-C. Shih, D. M. Shimabukuro, M. P. Wacks, M. E. Weber, and G. D. Goodno, "Scalable Coherent Combining of Kilowatt Fiber Amplifiers Into a 2.4-kW Beam," IEEE J. Sel. Top. Quantum Electron. **20**, 174–181 (2014).

[94] G. Krauss, S. Lohss, T. Hanke, A. Sell, S. Eggert, R. Huber, and A. Leitenstorfer, "Synthesis of a single cycle of light with compact erbium-doped fibre technology," Nat. Photonics **4**, 33–36 (2010).

[95] R. Banici and D. Ursescu, "Spectral combination of ultrashort laser pulses," Europhys. Lett. **94**, 44002 (2011).

[96] C. Manzoni, S.-W. Huang, G. Cirmi, P. Farinello, J. Moses, F. X. Kärtner, and G. Cerullo, "Coherent synthesis of ultra-broadband optical parametric amplifiers," Opt. Lett. **37**, 1880–1882 (2012).

[97] L. W. Casperson and A. Yariv, "Spectral narrowing in High-Gain Lasers," IEEE J. Quantum Electron. **8**, 80–85 (1972).

[98] F. Guichard, M. Hanna, L. Lombard, Y. Zaouter, C. Hönninger, F. Morin, F. Druon, E. Mottay, and P. Georges, "Two-channel pulse synthesis to overcome gain narrowing in femtosecond fiber amplifiers," Opt. Lett. **38**, 5430–5433 (2013).

[99] G. D. Goodno, C.-C. Shih, and J. E. Rothenberg, "Perturbative analysis of coherent combining efficiency with mismatched lasers," Opt. Express **18**, 25403–25414 (2010).

[100] G. D. Goodno, C.-C. Shih, and J. E. Rothenberg, "Perturbative analysis of coherent combining efficiency with mismatched lasers: errata," Opt. Express **20**, 23587–23588 (2012).

[101] A. Klenke, E. Seise, J. Limpert, and A. Tünnermann, "Basic considerations on coherent combining of ultrashort laser pulses," Opt. Express **19**, 25379–25387 (2011).

[102] H. Dammann and K. Görtler, "High-efficiency in-line multiple imaging by means of multiple phase holograms," Opt. Commun. **3**, 312–315 (1971).

[103] S. M. Redmond, D. J. Ripin, C. X. Yu, S. J. Augst, T. Y. Fan, P. A. Thielen, J. E. Rothenberg, and G. D. Goodno, "Diffractive coherent combining of a 2.5 kW fiber laser array into a 1.9 kW Gaussian beam," Opt. Lett. **37**, 2832–2834 (2012).

[104] P. A. Thielen, J. G. Ho, D. A. Burchman, G. D. Goodno, J. E. Rothenberg, M. G. Wickham, A. Flores, C. A. Lu, B. Pulford, C. Robin, A. D. Sanchez, D. Hult, and K. B. Rowland, "Two-dimensional diffractive coherent combining of 15 fiber amplifiers into a 600 W beam," Opt. Lett. **37**, 3741–3743 (2012).

[105] G. Mourou, B. Brocklesby, T. Tajima, and J. Limpert, "The future is fibre accelerators," Nat. Photonics **7**, 258–261 (2013).

[106] UAB Altechna, "Polarisierende Strahlteilerwürfel für Hochleistungsanwendungen," http://www.altechna.de, October 2016.

[107] J. Limpert, A. Klenke, M. Kienel, S. Breitkopf, T. Eidam, S. Hädrich, C. Jauregui, and A. Tünnermann, "Performance Scaling of Ultrafast Laser Systems by Coherent Addition of Femtosecond Pulses," IEEE J. Sel. Top. Quantum Electron. **20**, 268–277 (2014).

[108] Thorlabs GmbH, "Polaris™ Low Drift Kinematic Mirror Mounts," https://www.thorlabs.com, November 2016.

[109] Newport Spectra-Physics GmbH, "SUPREMA™ Low-Drift, High-Sensitivity Mirror Mounts," https://www.newport.com, November 2016.

[110] Newport Spectra-Physics GmbH, "Stainless Steel Crossed-Roller Bearing Translation Stages," https://www.newport.com, November 2016.

[111] R. J. Jones and J. Ye, "Femtosecond pulse amplification by coherent addition in a passive optical cavity," Opt. Lett. **27**, 1848–1850 (2002).

[112] Y. Vidne, M. Rosenbluh, and T. W. Hänsch, "Pulse picking by phase-coherent additive pulse generation in an external cavity," Opt. Lett. **28**, 2396–2398 (2003).

[113] R. J. Jones and J. Ye, "High-repetition-rate coherent femtosecond pulse amplification with an external passive optical cavity," Opt. Lett. **29**, 2812–2814 (2004).

[114] S. Breitkopf, S. Wunderlich, T. Eidam, E. Shestaev, S. Holzberger, T. Gottschall, H. Carstens, A. Tünnermann, I. Pupeza, and J. Limpert, "Extraction of enhanced, ultrashort laser pulses from a passive 10-MHz stack-and-dump cavity," Appl. Phys. B Lasers Opt. **122**, 1–7 (2016).

[115] H. E. Bates, R. R. Alfano, and N. Schiller, "Picosecond pulse stacking in calcite," Appl. Opt. **18**, 947–949 (1979).

[116] B. Dromey, M. Zepf, M. Landreman, K. O'keeffe, T. Robinson, and S. M. Hooker, "Generation of a train of ultrashort pulses from a compact birefringent crystal array," Appl. Opt. **46**, 5142–5146 (2007).

[117] S. Zhou, D. Ouzounov, F. Wise, I. Bazarov, and C. Sinclair, "Efficient temporal shaping of ultrashort pulses with birefringent crystals," Appl. Opt. **46**, 8488–8492 (2007).

[118] A. K. Sharma, T. Tsang, and T. Rao, "Theoretical and experimental study of passive spatiotemporal shaping of picosecond laser pulses," Phys. Rev. Spec. Top. - Accel. Beams **12**, 033501 (2009).

[119] C. W. Siders, J. L. Siders, A. J. Taylor, S. G. Park, and A. M. Weiner, "Efficient High-Energy Pulse-Train Generation Using a 2^n-Pulse Michelson Interferometer," Appl. Opt. **37**, 5302–5305 (1998).

[120] H. E. Bates, "Coherent birefringent optical pulse compression," J. Opt. Soc. Am. **70**, 1017–1020 (1980).

[121] L. Daniault, M. Hanna, D. N. Papadopoulos, Y. Zaouter, E. Mottay, F. Druon, and P. Georges, "High peak-power stretcher-free femtosecond fiber amplifier using passive spatio-temporal coherent combining," Opt. Express **20**, 21627–21634 (2012).

[122] H. Jacqmin, A. Jullien, B. Mercier, M. Hanna, F. Druon, D. Papadopoulos, and R. Lopez-Martens, "Passive coherent combining of CEP-stable few-cycle pulses from a temporally divided hollow fiber compressor," Opt. Lett. **40**, 709–712 (2015).

[123] H. Jacqmin, A. Jullien, B. Mercier, and R. Lopez-Martens, "Temporal pulse division in hollow fiber compressors," J. Opt. Soc. Am. B **32**, 1901–9 (2015).

[124] C. Radzewicz, M. J. la Grone, and J. S. Krasinski, "Passive pulse shaping of femtosecond pulses using birefringent dispersive media," Appl. Phys. Lett. **69**, 272–274 (1996).

[125] T. Robinson, K. O'Keeffe, M. Zepf, B. Dromey, and S. M. Hooker, "Generation and control of ultrafast pulse trains for quasi-phase-matching high-harmonic generation," J. Opt. Soc. Am. B **27**, 763–772 (2010).

[126] D. P. Landau and K. Binder, *A Guide to Monte Carlo Simulations in Statistical Physics* (Cambridge University Press, 2009), 3rd ed.

[127] UAB Altechna, "Dünnschichtpolarisatoren (Brewster Typ)," http://www.altechna.de, February 2017.

[128] UAB Altechna, "Dünnschichtpolarisatoren mit hohem Kontrast (Brewster Typ)," http://www.altechna.de, February 2017.

[129] L. J. Kong, L. M. Zhao, S. Lefrancois, D. G. Ouzounov, C. X. Yang, and F. W. Wise, "Generation of megawatt peak power picosecond pulses from a divided-pulse fiber amplifier," Opt. Lett. **37**, 253–255 (2012).

[130] F. Jansen, F. Stutzki, H.-J. Otto, T. Eidam, A. Liem, C. Jauregui, J. Limpert, and A. Tünnermann, "Thermally induced waveguide changes in active fibers," Opt. Express **20**, 3997–4008 (2012).

[131] M. Kienel, A. Klenke, T. Eidam, M. Baumgartl, C. Jauregui, J. Limpert, and A. Tünnermann, "Analysis of passively combined divided-pulse amplification as an energy-scaling concept," Opt. Express **21**, 29031–29042 (2013).

[132] M. Nisoli, S. De Silvestri, and O. Svelto, "Generation of high energy 10 fs pulses by a new pulse compression technique," Appl. Phys. Lett. **68**, 2793–2795 (1996).

[133] C. Thaury, F. Quéré, J.-P. Geindre, A. Levy, T. Ceccotti, P. Monot, M. Bougeard, F. Réau, P. D'Oliveira, P. Audebert, R. Marjoribanks, and P. Martin, "Plasma mirrors for ultrahigh-intensity optics," Nat. Phys. **3**, 424–429 (2007).

[134] E. Seise, A. Klenke, S. Breitkopf, M. Plötner, J. Limpert, and A. Tünnermann, "Coherently combined fiber laser system delivering 120 µJ femtosecond pulses," Opt. Lett. **36**, 439–441 (2011).

[135] A. Klenke, S. Breitkopf, M. Kienel, T. Gottschall, T. Eidam, S. Hädrich, J. Rothhardt, J. Limpert, and A. Tünnermann, "530 W, 1.3 mJ, four-channel coherently combined femtosecond fiber chirped-pulse amplification system," Opt. Lett. **38**, 2283–2285 (2013).

[136] A. Klenke, S. Hädrich, T. Eidam, J. Rothhardt, M. Kienel, S. Demmler, T. Gottschall, J. Limpert, and A. Tünnermann, "22 GW peak-power fiber chirped-pulse-amplification system," Opt. Lett. **39**, 6875–6878 (2014).

[137] M. Müller, M. Kienel, A. Klenke, T. Gottschall, E. Shestaev, M. Plötner, J. Limpert, and A. Tünnermann, "1 kW 1 mJ eight-channel ultrafast fiber laser," Opt. Lett. **41**, 3439–3442 (2016).

[138] F. Guichard, Y. Zaouter, M. Hanna, K.-L. Mai, F. Morin, C. Hönninger, E. Mottay, and P. Georges, "High-energy chirped- and divided-pulse Sagnac femtosecond fiber amplifier," Opt. Lett. **40**, 89–92 (2015).

[139] Y. Zaouter, F. Guichard, C. Hoenninger, E. Mottay, M. Hanna, and P. Georges, "High average power 600 µJ ultrafast fiber laser for micromachining application," J. Laser Appl. **27**, S29301 (2015).

[140] M. Kienel, A. Klenke, T. Eidam, S. Hädrich, J. Limpert, and A. Tünnermann, "Energy scaling of femtosecond amplifiers using actively controlled divided-pulse amplification," Opt. Lett. **39**, 1049–1052 (2014).

[141] M. Kienel, M. Müller, A. Klenke, T. Eidam, J. Limpert, and A. Tünnermann, "Multidimensional coherent pulse addition of ultrashort laser pulses," Opt. Lett. **40**, 522–525 (2015).

[142] M. Kienel, M. Müller, A. Klenke, J. Limpert, and A. Tünnermann, "12 mJ kW-class ultrafast fiber laser system using multidimensional coherent pulse addition," Opt. Lett. **41**, 3343–3346 (2016).

[143] J. Ye and J. L. Hall, "Optical phase locking in the microradian domain: potential applications to NASA spaceborne optical measurements," Opt. Lett. **24**, 1838–1840 (1999).

[144] G. D. Goodno, C. P. Asman, J. Anderegg, S. Brosnan, E. C. Cheung, D. Hammons, H. Injeyan, H. Komine, W. H. Long, M. McClellan, S. J. McNaught, S. Redmond, R. Simpson, J. Sollee, M. Weber, S. Benjamin Weiss, and M. Wickham, "Brightness-scaling potential of actively phase-locked solid-state laser arrays," IEEE J. Sel. Top. Quantum Electron. **13**, 460–471 (2007).

[145] T. W. Hänsch and B. Couillaud, "Laser frequency stabilization by polarization spectroscopy of a reflecting reference cavity," Opt. Commun. **35**, 441–444 (1980).

[146] T. M. Shay, "Theory of electronically phased coherent beam combination without a reference beam," Opt. Express **14**, 12188–12195 (2006).

[147] M. A. Vorontsov and V. P. Sivokon, "Stochastic parallel-gradient-descent technique for high-resolution wave-front phase-distortion correction," J. Opt. Soc. Am. A **15**, 2745–2758 (1998).

[148] T. M. Shay, V. Benham, J. T. Baker, A. D. Sanchez, D. Pilkington, and C. A. Lu, "Self-Synchronous and Self-Referenced Coherent Beam Combination for Large Optical Arrays," IEEE J. Sel. Top. Quantum Electron. **13**, 480–486 (2007).

[149] L. A. Siiman, W.-z. Chang, T. Zhou, and A. Galvanauskas, "Coherent femtosecond pulse combining of multiple parallel chirped pulse fiber amplifiers," Opt. Express **20**, 18097–18116 (2012).

[150] Y. Ma, P. Zhou, X. Wang, H. Ma, X. Xu, L. Si, Z. Liu, and Y. Zhao, "Coherent beam combination with single frequency dithering technique," Opt. Lett. **35**, 1308–1310 (2010).

[151] H. K. Ahn and H. J. Kong, "Cascaded multi-dithering theory for coherent beam combining of multiplexed beam elements," Opt. Express **23**, 12407–12413 (2015).

[152] G. Cheriaux, P. Rousseau, F. Salin, J. P. Chambaret, B. Walker, and L. F. Dimauro, "Aberration-free stretcher design for ultrashort-pulse amplification," Opt. Lett. **21**, 414–416 (1996).

[153] V. V. Lozovoy, I. Pastirk, and M. Dantus, "Multiphoton intrapulse interference IV. Ultrashort laser pulse spectral phase characterization and compensation," Opt. Lett. **29**, 775–777 (2004).

[154] E. B. Treacy, "Optical Pulse Compression With Diffraction Gratings," IEEE J. Quantum Electron. **QE-5**, 454–458 (1969).

[155] I. Astrauskas, E. Kaksis, T. Flöry, G. Andriukaitis, A. Pugzlys, A. Baltuska, J. Ruppe, S. Chen, A. Galvanauskas, and T. Balciunas, "High-Energy Pulse Stacking via Regenerative Pulse-Burst Amplification," in "Lasers Congr. 2016 (ASSL, LSC, LAC)," (Optical Society of America, 2016), p. AM4A.5.

[156] M. J. F. Digonnet, R. W. Sadowski, H. J. Shaw, and R. H. Pantell, "Resonantly Enhanced Nonlinearity in Doped Fibers for Low-Power All-Optical Switching: A Review," Opt. Fiber Technol. **3**, 44–64 (1997).

[157] F. Guichard, L. Lavenu, M. Hanna, Y. Zaouter, and P. Georges, "Coherent combining efficiency in strongly saturated divided-pulse amplification systems," Opt. Express **24**, 4437–4440 (2016).

[158] M. Müller, M. Kienel, A. Klenke, T. Eidam, J. Limpert, and A. Tünnermann, "Phase stabilization of spatiotemporally multiplexed ultrafast amplifiers," Opt. Express **24**, 7893–7904 (2016).

[159] Active Fiber Systems GmbH, "Active Fiber Systems GmbH," http://www.afs-jena.de/, December 2016.

[160] D. N. Schimpf, E. Seise, J. Limpert, and A. Tünnermann, "The impact of spectral modulations on the contrast of pulses of nonlinear chirped-pulse amplification systems," Opt. Express **16**, 10664–10674 (2008).

[161] M. Müller, M. Wojdyr, M. Kienel, A. Klenke, J. Limpert, and A. Tünnermann, "Electro-optically controlled divided-pulse amplification," in "Proc. SPIE," (2016), pp. 97282J–97282J–5.

[162] D. R. Herriott and H. J. Schulte, "Folded Optical Delay Lines," Appl. Opt. **4**, 883–889 (1965).

[163] S. Breitkopf, T. Eidam, A. Klenke, L. von Grafenstein, H. Carstens, S. Holzberger, E. Fill, T. Schreiber, F. Krausz, A. Tünnermann, I. Pupeza, and J. Limpert, "A concept for multiterawatt fibre lasers based on coherent pulse stacking in passive cavities," Light Sci. Appl. **3**, 1–7 (2014).

[164] T. Zhou, J. Ruppe, C. Zhu, I.-N. Hu, J. Nees, and A. Galvanauskas, "Coherent pulse stacking amplification using low-finesse Gires-Tournois interferometers," Opt. Express **23**, 7442–7462 (2015).

[165] T. Zhou, J. Ruppe, P. Stanfield, J. Nees, R. Wilcox, and A. Galvanauskas, "Resonant cavity based time-domain multiplexing techniques for coherently combined fiber laser systems," Eur. Phys. J. Spec. Top. **224**, 2585–2602 (2015).

[166] J. Ruppe, S. Chen, M. Sheikhsofla, R. Wilcox, J. Nees, and A. Galvanauskas, "Multiplexed Coherent Pulse Stacking of 27 Pulses in a 4 + 1 GTI Resonator Sequence," in "Lasers Congr. 2016 (ASSL, LSC, LAC)," (Optical Society of America, 2016), p. AM4A.6.

[167] A. Klenke, M. Wojdyr, M. Müller, M. Kienel, T. Eidam, H.-J. Otto, F. Stutzki, F. Jansen, J. Limpert, and A. Tünnermann, "Large-pitch Multicore Fiber for Coherent Combination of Ultrashort Pulses," in "Eur. Conf. Lasers Electro-Optics - Eur. Quantum Electron. Conf.", (Optical Society of America, 2015), p. CJ_1_2.

[168] F. Friebel, S. Ricaud, A. Pellegrina, M. Hanna, E. Mottay, P. Camy, J. L. Doualan, and R. Moncorgé, "High energy and broadband Yb:CaF$_2$ multipass amplifier using passive coherent combining," in "Eur. Conf. Lasers Electro-Optics - Eur. Quantum Electron. Conf.", (2013), p. CA_10_4.

[169] E. S. Lamb, L. G. Wright, and F. W. Wise, "Divided-pulse lasers," Opt. Lett. **39**, 2775–2777 (2014).

[170] S. Hädrich, M. Kienel, M. Müller, A. Klenke, J. Rothhardt, R. Klas, T. Gottschall, T. Eidam, A. Drozdy, P. Jójárt, Z. Várallyay, E. Cormier, K. Osvay, A. Tünnermann, and J. Limpert, "Energetic sub-2-cycle laser with 216 W average power," Opt. Lett. **41**, 4332–4335 (2016).

[171] A. Klenke, S. Hädrich, M. Kienel, T. Eidam, J. Limpert, and A. Tünnermann, "Coherent combination of spectrally broadened femtosecond pulses for nonlinear compression," Opt. Lett. **39**, 3520–3522 (2014).

[172] A. Klenke, M. Kienel, T. Eidam, S. Hädrich, J. Limpert, and A. Tünnermann, "Divided-pulse nonlinear compression," Opt. Lett. **38**, 4593–4596 (2013).

[173] F. Guichard, Y. Zaouter, M. Hanna, F. Morin, C. Hönninger, E. Mottay, F. Druon, and P. Georges, "Energy scaling of a nonlinear compression setup using passive coherent combining," Opt. Lett. **38**, 4437–4440 (2013).

[174] H. Jacqmin, B. Mercier, A. Jullien, and R. Lopez-Martens, "Manifold coherent combining of few-cycle pulses in hollow-fiber compressors," Appl. Phys. B Lasers Opt. **122**, 1–11 (2016).

Appendix

A. Jones Matrices

Following Eq. (2.33), the Jones matrix for a general wave plate (phase retarder) is [60]

$$\mathcal{M}_{\text{WP}} = \begin{bmatrix} \exp(i\varphi_{\text{o}}) & 0 \\ 0 & \exp(i\varphi_{\text{e}}) \end{bmatrix} = \exp(i\varphi_{\text{o}}) \begin{bmatrix} 1 & 0 \\ 0 & \exp(i\Delta\varphi) \end{bmatrix}. \tag{A.1}$$

Typically, one is interested in the phase difference and, therefore, the constant phase factor $\exp(i\varphi_{\text{o}})$ is usually omitted.

A rotation of an optical system (i.e. a transformation of its x-y-coordinate system) by an angle θ leads to a transformation of its Jones matrix $\mathcal{M}$ to $\mathcal{M}(\theta)$. Using the rotation matrix [58]

$$\mathcal{R}(\theta) = \begin{bmatrix} \cos(\theta) & \sin(\theta) \\ -\sin(\theta) & \cos(\theta) \end{bmatrix} \tag{A.2}$$

then results in the transformed Jones matrix

$$\mathcal{M}(\theta) = \mathcal{R}(-\theta)\mathcal{M}\mathcal{R}(\theta). \tag{A.3}$$

In case of any beam splitter, there is a phase jump between the transmitted and reflected beam (in Tab. 2.1 indicated by (i) between $\mathcal{M}_{\text{T}}$ and $\mathcal{M}_{\text{R}}$). This can be explained by considering a complex electric field $\mathbf{E}(\mathbf{r}, t)$ that is divided in $\mathbf{E}_1(\mathbf{r}, t)$ and $\mathbf{E}_2(\mathbf{r}, t)$. In terms of power conservation the following equation should be fulfilled:

$$|\mathbf{E}(\mathbf{r}, t)|^2 = |\mathbf{E}_1(\mathbf{r}, t)|^2 + |\mathbf{E}_2(\mathbf{r}, t)|^2. \tag{A.4}$$

Hence, the superposition of both fields (e.g. assuming a Michelson interferometer implementation) should lead to the same result. Thus (brackets omitted)

$$|\mathbf{E}|^2 = (\mathbf{E}_1 + \mathbf{E}_2)(\mathbf{E}_1 + \mathbf{E}_2)^* = |\mathbf{E}_1|^2 + |\mathbf{E}_2|^2 + \mathbf{E}_1\mathbf{E}_2^* + \mathbf{E}_1^*\mathbf{E}_2. \tag{A.5}$$

Consequently, the interference term

$$\mathbf{E}_1\mathbf{E}_2^* + \mathbf{E}_1^*\mathbf{E}_2 = 2\Re\left\{\mathbf{E}_1\mathbf{E}_2^*\right\}\cos(\phi_1 - \phi_2) \tag{A.6}$$

has to be zero, which requires a phase difference of $\phi_1 - \phi_2 = \pm\pi/2$ between the two beams obtained after splitting.

B. Spatio-Temporal Combination

The superposition of two beams (from channel 1 and channel 2) with two pulse replicas is illustrated in Fig. B.1a. The information of the initially orthogonally-polarized pulse replicas before the spatial division is imprinted in their phases (indicated in Fig. B.1a by the blue lines). If the bursts within each channel are amplified differently, the corresponding magnitudes of the p- and s-polarization components will change. As can be seen from the figure, the desired angle of 90° between both resulting pulse replicas is reduced. This cannot be compensated for by a subsequent HWP and, thus, results in pre- and post-pulses. In order to simulate this effect, a burst of two pulse replicas that is split into two channels has been considered. A constant power ratio between them is introduced (the effects of gain saturation and nonlinear phase differences have been neglected). Subsequently, both channels are combined and the pulses are stacked. In Fig. B.1b $\eta_{\text{comb}}^{\text{spat}}$ (orange line) and $\eta_{\text{stack}}^{\text{temp}}$ (green line), according to Eqs. (3.5) and (3.10), are shown. In this particular case, both efficiencies decrease similarly with decreasing power ratio. The difference between both efficiencies will change for bursts with more than two pulse replicas. In any case,
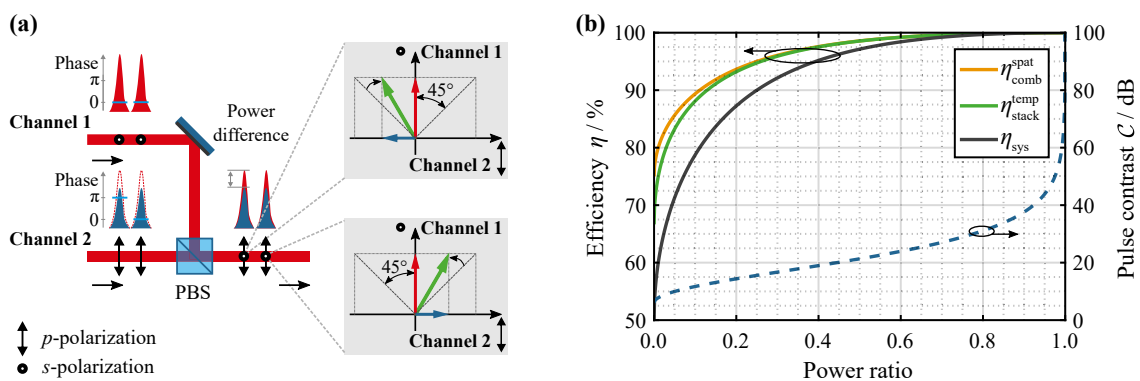
Figure B.1.: (a) Schematic of the polarization-orientation change for the superposition of two bursts comprising two pulse replicas that have different powers (vector representation is illustrated). (b) Simulated spatial combination efficiency $\eta_{\text{comb}}^{\text{spat}}$, temporal stacking efficiency $\eta_{\text{stack}}^{\text{temp}}$, overall system efficiency η_{sys} and pulse contrast $\mathcal{C}$ as a function of the power ratio between two beams (channels), each comprising bursts of two pulse replicas.

the total system efficiency η_{sys} (black line), according to Eq. (3.11), is in the worst case (assuming constructive interference) 50%. What can be seen is that even for a power ratio of, for example, 0.5 the system efficiency remains $> 97\%$, with the content in pre- and post pulses being 1.5%. Even though the efficiency is high, the (theoretically maximum) pulse contrast[1] $\mathcal{C}$, according to Eq. (3.12), is strongly decreased even for power ratios slightly below 1. At a power ratio of 0.5, $\mathcal{C}$ is 21dB.

C. Derivation of the LOCSET Error Signal for Spatio-Temporal Combination

A schematic of the experimental setup shown in Fig. 5.8 is depicted in Fig. C.2. It will be used for illustration purposes of the following derivation. The main functional steps are marked with roman numerals. These include both temporal pulse division and stacking steps (I,II,V,VI), the spatial division and combination (III,IV) and the signal detection at the final output (VII). In order to track all possible temporal positions of the pulse replicas (analogously to Fig. 3.11) within such a system, a quasi-time-resolved Jones formalism (according to Subsec. 2.3.3) is applied. For simplicity, the pulses are considered as complex amplitudes (see Eq. (2.32)) and for, the pulse division, all optical components are assumed to be ideal ($T_{\mathrm{p}} = R_{\mathrm{s}} = 1$).

Thus, the Jones vector of the initial p-polarized pulse $\mathbf{J}_0(t)$ (according to Fig. C.2) is
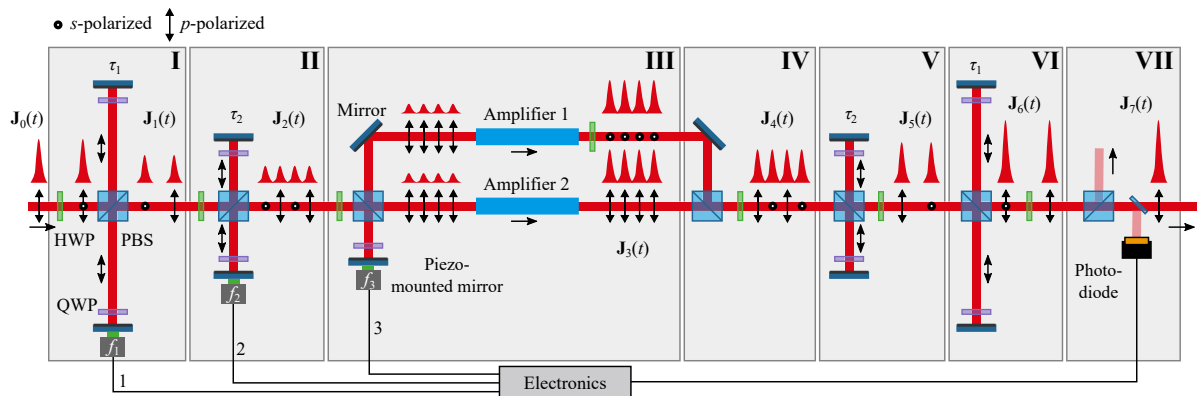
Figure C.2.: Schematic of the spatio-temporal combination setup employing two temporal pulse division stages (I,II), a spatial division into two amplifier channels (III), their combination (IV), two pulse stacking stages (V,VI) and the error signal detection at the final output (VII). HWP: half-wave plate, QWP: quarter-wave plate, PBS: polarizing beam splitter.

---

[1]Regarding Subsec. 3.2.3, angle uncertainties of the HWPs are not considered and $T_{\mathrm{p}} = R_{\mathrm{s}} = 1$ for the PBSs have been assumed.

represented as

$$\mathbf{J}_0(t) = \begin{bmatrix} 1 \\ 0 \end{bmatrix} A\delta(t), \tag{C.7}$$

where A is the complex amplitude and δ is the Dirac delta function. Two pulse replicas of equal power are generated in the subsequent temporal division (I) delayed by τ_1. Using the Jones matrices[2] from Tab. 2.1, the Jones vector at the output of section I is given by

$$\mathbf{J}_1(t) = \left[\mathcal{M}_{\mathrm{T}} + \mathcal{M}_{\mathrm{R}} \, \mathcal{M}_{\mathrm{QWP}}^2(45°)\mathcal{M}_{\mathrm{T}}\mathcal{M}_{\mathrm{QWP}}^2(45°)\mathcal{M}_{\mathrm{R}} \right] \mathcal{M}_{\mathrm{HWP}}(22.5°)\mathbf{J}_0(t) \tag{C.8}$$

$$\mathbf{J}_1(t) = \frac{A}{\sqrt{2}} \left\{ \begin{bmatrix} 1 \\ 0 \end{bmatrix} \delta(t) + \begin{bmatrix} 0 \\ 1 \end{bmatrix} \delta(t - \tau_1) \right\}, \tag{C.9}$$

with the delay τ_1 being accounted for as a shift of the temporal position (indicated by $\rightarrow$) of the delayed pulse to $t - \tau_1$. In order to simplify the derivation, the following short notation will be used:

$$\mathbf{J}_1(t) = \frac{A}{\sqrt{2}} \left\{ \begin{bmatrix} 1 \\ 0 \end{bmatrix} + \begin{bmatrix} 0 \\ 1 \end{bmatrix} * \tau_1 \right\}, \tag{C.10}$$

with the leading pulse being considered as the reference and the temporal position of the trailing pulse being denoted by $*\tau_1$. Please note that the phase dithers imposed by the piezo-mounted mirrors will be accounted for upon combination, since the position of those elements can be freely chosen in the division or stacking stages. Next, the generated pulses are divided again (II). Thereby, a delay τ_2 with $2\tau_2 < \tau_1$ is introduced. Please note that the derivation is based on the condition that $\tau_1 \neq 2\tau_2$. Thus, after the second division, the Jones vector is

$$\mathbf{J}_2(t) = \left[\mathcal{M}_{\mathrm{T}} + \mathcal{M}_{\mathrm{R}} \, \mathcal{M}_{\mathrm{QWP}}^2(45°)\mathcal{M}_{\mathrm{T}}\mathcal{M}_{\mathrm{QWP}}^2(45°)\mathcal{M}_{\mathrm{R}} \right] \mathcal{M}_{\mathrm{HWP}}(22.5°)\mathbf{J}_1(t) \tag{C.11}$$

$$\mathbf{J}_2(t) = \frac{A}{2} \left\{ \begin{bmatrix} 1 \\ 0 \end{bmatrix} + \begin{bmatrix} 0 \\ 1 \end{bmatrix} * \tau_2 + \begin{bmatrix} 1 \\ 0 \end{bmatrix} * \tau_1 + \begin{bmatrix} 0 \\ -1 \end{bmatrix} * (\tau_1 + \tau_2) \right\}. \tag{C.12}$$

Equation (C.12) describes a burst of four pulses with alternating *p*- and *s*-polarization. This burst is divided into two spatially separated amplifier channels (III): While the *s*-polarized part is reflected towards channel 1, the *p*-polarized part goes through channel 2. Thus, these two branches can be treated as the two dimensions of the Jones vector,

---

[2]The phase shift generated upon reflection will be omitted.

which is

$$\mathbf{J}_3(t) = \left[\mathcal{M}_\mathrm{T} + \mathcal{M}_\mathrm{HWP}(45°)\mathcal{M}_\mathrm{T}\mathcal{M}_\mathrm{QWP}^2(45°)\mathcal{M}_\mathrm{R} \right] \mathcal{M}_\mathrm{HWP}(22.5°)\mathbf{J}_2(t) \tag{C.13}$$

$$\mathbf{J}_3(t) = \frac{A}{2\sqrt{2}} \left\{ \begin{bmatrix} 1 \\ 1 \end{bmatrix} + \begin{bmatrix} 1 \\ -1 \end{bmatrix} * \tau_2 + \begin{bmatrix} 1 \\ 1 \end{bmatrix} * \tau_1 + \begin{bmatrix} -1 \\ 1 \end{bmatrix} * (\tau_1 + \tau_2) \right\}. \tag{C.14}$$

Disregarding the amplification, the bursts are subsequently spatially combined (IV). An unknown relative phase Φ_3 between them is considered, expressed by

$$\Phi_3 = \beta_3 \sin(2\pi f_3 t) + \Delta\phi_3 \rightarrow \exp(i\Phi_3) := \Psi_3, \tag{C.15}$$

with β_3 being the modulation depth and f_3 being the modulation frequency of the piezo-mounted mirror for LOCSET. In this context, $\Delta\phi_3$ is the phase error between both amplifier channels. The exponential phase term will be abbreviated by Ψ_3. In the case in which the phases are matched, the alternating linear polarization pattern of the combined burst is rotated by 45°. The subsequent HWP is set to $-22.5°$, which results in an s-polarized leading pulse. Then, the Jones vector becomes

$$\mathbf{J}_4(t) = \mathcal{M}_\mathrm{HWP}(-22.5°) \begin{bmatrix} 1 & 0 \\ 0 & \Psi_3 \end{bmatrix} \mathbf{J}_3(t) \tag{C.16}$$

$$\mathbf{J}_4(t) = \frac{A}{4} \left\{ \begin{bmatrix} 1 - \Psi_3 \\ -1 - \Psi_3 \end{bmatrix} + \begin{bmatrix} 1 + \Psi_3 \\ -1 + \Psi_3 \end{bmatrix} * \tau_2 + \begin{bmatrix} 1 - \Psi_3 \\ -1 - \Psi_3 \end{bmatrix} * \tau_1 + \begin{bmatrix} -1 - \Psi_3 \\ 1 - \Psi_3 \end{bmatrix} * (\tau_1 + \tau_2) \right\}, \tag{C.17}$$

with the two vector components representing, again, p and s-polarization. Next, the temporal delay of the short delay line (τ_2) is removed (V). The relative phase Φ_2 between the superposed p- and s-polarized pulses is

$$\Phi_2 = \beta_2 \sin(2\pi f_2 t) + \Delta\phi_2 \rightarrow \exp(i\Phi_2) := \Psi_2, \tag{C.18}$$

with the modulation depth β_2, the modulation frequency f_2 and the unknown phase error $\Delta\phi_2$. The subsequent HWP is set to 22.5°, resulting in an s-polarized leading pulse and a p-polarized trailing pulse. Combination mismatches will emerge in the form of pre- and post-pulses after the following stacking step, since undesired polarization components will travel along the different optical paths of the delay line. After the first temporal stacking

step the Jones vector is

$$\mathbf{J}_5(t) = \mathcal{M}_{\mathrm{HWP}}(22.5°) \begin{bmatrix} 1 & 0 \\ 0 & \Psi_2 \end{bmatrix} \left[\underset{t \to t}{\mathcal{M}_{\mathrm{T}}} + \underset{t \to t - \tau_2}{\mathcal{M}_{\mathrm{R}}} \mathcal{M}_{\mathrm{QWP}}^2(45°)\mathcal{M}_{\mathrm{T}}\mathcal{M}_{\mathrm{QWP}}^2(45°)\mathcal{M}_{\mathrm{R}} \right] \mathbf{J}_4(t)$$

$$\text{(C.19)}$$

$$\begin{aligned} \mathbf{J}_5(t) = \frac{A}{4\sqrt{2}} \Bigg\{ & \begin{bmatrix} 1 - \Psi_3 \\ 1 - \Psi_3 \end{bmatrix} + \begin{bmatrix} (1 + \Psi_3)(1 - \Psi_2) \\ (1 + \Psi_3)(1 + \Psi_2) \end{bmatrix} * \tau_2 \\ & + \begin{bmatrix} (-1 + \Psi_3)\Psi_2 \\ (1 - \Psi_3)\Psi_2 \end{bmatrix} * 2\tau_2 + \begin{bmatrix} 1 - \Psi_3 \\ 1 - \Psi_3 \end{bmatrix} * \tau_1 \\ & + \begin{bmatrix} (1 + \Psi_3)(-1 - \Psi_2) \\ (1 + \Psi_3)(-1 + \Psi_2) \end{bmatrix} * (\tau_1 + \tau_2) + \begin{bmatrix} (1 - \Psi_3)\Psi_2 \\ (-1 + \Psi_3)\Psi_2 \end{bmatrix} * (\tau_1 + 2\tau_2) \Bigg\}, \end{aligned}$$

$$\text{(C.20)}$$

where the *s*-polarized component is delayed by τ_2. Next, the remaining temporal delay (τ_1) is removed (VI). In the best case there are two pulses left, which are superposed after the delay line. The relative phase Φ_1 between the pulses is given by

$$\Phi_1 = \beta_1 \sin(2\pi f_1 t) + \Delta\phi_1 \to \exp(i\Phi_1) := \Psi_1, \quad \text{(C.21)}$$

with the modulation depth β_1, the modulation frequency f_1 and the unknown phase error $\Delta\phi_1$. A further HWP, set to $-22.5°$, rotates the stacked pulse to *p*-polarization (VI). Hence, it follows

$$\mathbf{J}_6(t) = \mathcal{M}_{\mathrm{HWP}}(-22.5°) \begin{bmatrix} 1 & 0 \\ 0 & \Psi_1 \end{bmatrix} \left[\underset{t \to t}{\mathcal{M}_{\mathrm{T}}} + \underset{t \to t - \tau_1}{\mathcal{M}_{\mathrm{R}}} \mathcal{M}_{\mathrm{QWP}}^2(45°)\mathcal{M}_{\mathrm{T}}\mathcal{M}_{\mathrm{QWP}}^2(45°)\mathcal{M}_{\mathrm{R}} \right] \mathbf{J}_5(t)$$

$$\text{(C.22)}$$

$$\begin{aligned} \mathbf{J}_6(t) = \frac{A}{8} \Bigg\{ & \begin{bmatrix} -1 + \Psi_3 \\ -1 + \Psi_3 \end{bmatrix} + \begin{bmatrix} (1 + \Psi_3)(1 - \Psi_2) \\ (1 + \Psi_3)(-1 + \Psi_2) \end{bmatrix} * \tau_2 + \begin{bmatrix} (-1 + \Psi_3)\Psi_2 \\ (1 - \Psi_3)\Psi_2 \end{bmatrix} * 2\tau_2 \\ & + \begin{bmatrix} (1 - \Psi_3)(1 - \Psi_1) \\ (1 - \Psi_3)(-1 - \Psi_1) \end{bmatrix} * \tau_1 + \begin{bmatrix} -(1 + \Psi_3)(1 + \Psi_2)(1 + \Psi_1)) \\ (1 + \Psi_3)(1 + \Psi_2)(1 - \Psi_1) \end{bmatrix} * (\tau_1 + \tau_2) \\ & + \begin{bmatrix} (1 - \Psi_3)(1 - \Psi_1)\Psi_2 \\ (1 - \Psi_3)(-1 - \Psi_1)\Psi_2 \end{bmatrix} * (\tau_1 + 2\tau_2) + \begin{bmatrix} (-1 + \Psi_3)\Psi_1 \\ (-1 + \Psi_3)\Psi_1 \end{bmatrix} * 2\tau_1 \\ & + \begin{bmatrix} (1 + \Psi_3)(1 - \Psi_2)\Psi_1 \\ (1 + \Psi_3)(1 - \Psi_2)\Psi_1 \end{bmatrix} * (2\tau_1 + \tau_2) + \begin{bmatrix} (1 - \Psi_3)\Psi_2\Psi_1 \\ (1 - \Psi_3)\Psi_2\Psi_1 \end{bmatrix} * (2\tau_1 + 2\tau_2) \Bigg\}, \end{aligned}$$

$$\text{(C.23)}$$

where the s-polarized component is delayed by τ_1. Thus, there are nine possible temporal positions in which pulses can occur. In the best case, i.e. for all $\Psi_m = 1$ where $m = 1, 2, 3$, only a single p-polarized pulse exists at $\tau_1 + \tau_2$. Finally, after the propagation though the PBS (VII) only the p-polarization component is left, which is

$$\mathbf{J}_7(t) = \mathcal{M}_{\mathrm{T}}\mathbf{J}_6(t) \tag{C.24}$$

$$\begin{aligned} A_{7,\mathrm{p}}(t) = \frac{A}{8} \big[& (-1 + \Psi_3) + (1 + \Psi_3)(1 - \Psi_2) * \tau_2 + (-1 + \Psi_3)\Psi_2 * 2\tau_2 \\ & + (1 - \Psi_3)(1 - \Psi_1) * \tau_1 - (1 + \Psi_3)(1 + \Psi_2)(1 + \Psi_1) * (\tau_1 + \tau_2) \\ & + (1 - \Psi_3)(1 - \Psi_1)\Psi_2 * (\tau_1 + 2\tau_2) + (-1 + \Psi_3)\Psi_1 * (2\tau_1) \\ & + (1 + \Psi_3)(1 - \Psi_2)\Psi_1 * (2\tau_1 + \tau_2) + (1 - \Psi_3)\Psi_2\Psi_1 * (2\tau_1 + 2\tau_2) \big]. \end{aligned} \tag{C.25}$$

The slowly varying intensity detected by the photo-diode is then given by

$$I(t) \sim \langle A_{7,\mathrm{p}}(t)^* A_{7,\mathrm{p}}(t) \rangle \tag{C.26}$$

$$I(t) \sim \frac{A^2}{8} \left[4 + \cos\Phi_1 \left(\cos\Phi_3(\cos\Phi_2 + 2) + \cos\Phi_2 \right) \right], \tag{C.27}$$

with $\langle \cdot \rangle$ denoting the time average, which makes the fast optical oscillation vanish. Assuming a linear response of the photo-diode, the error signals S_m for the corresponding Ψ_m are obtained by demodulation at the respective frequency in the electronic domain according to Eq. (4.6). If the integration time $T \gg 1/|f_m - f_{j \neq m}|$ (with j denoting the neighboring modulation frequencies) is sufficiently long to isolate the individual modulation signals, the error signals for the three phase-modulation channels will be given by

$$S_1 \sim J_1(\beta_1)\sin(\Delta\phi_1)\left\{ J_0(\beta_3)\cos(\Delta\phi_3)\left[J_0(\beta_2)\cos(\Delta\phi_2) + 2 \right] + J_0(\beta_2)\cos(\Delta\phi_2) \right\}, \tag{C.28}$$

$$S_2 \sim J_1(\beta_2)\sin(\Delta\phi_2)J_0(\beta_1)\cos(\Delta\phi_1)\left[J_0(\beta_3)\cos(\Delta\phi_3) + 1 \right], \tag{C.29}$$

$$S_3 \sim J_1(\beta_3)\sin(\Delta\phi_3)J_0(\beta_1)\cos(\Delta\phi_1)\left[J_0(\beta_2)\cos(\Delta\phi_2) + 2 \right], \tag{C.30}$$

where J_n are Bessel functions of the first kind and nth order.

Zusammenfassung (Summary)

Ultrakurzpulslaser mit hoher mittlerer Ausgangsleistung sind ein etabliertes Werkzeug für eine Vielzahl von Anwendungen in Wissenschaft und Technik. Die Entwicklung immer anspruchsvollerer Anwendungen erhöht stetig die Anforderungen an das Lasersystem bezüglich mittlerer Leistung, Pulsenergie und -spitzenleistung. Die gleichzeitige Bereitstellung all dieser Parameter stellt große Herausforderungen an jedes Lasersystem, welches immer durch physikalische Gesetze und Fertigungstechnologie begrenzt ist. Eine Möglichkeit diese Limitierungen zu überwinden ist räumliche und zeitliche kohärente Addition ultrakurzer Pulse. Diese Verfahren wurden in dieser Arbeit, basierend auf den dazu hervorragend geeigneten Faserverstärkern, theoretisch und experimentell untersucht. Wohingegen die räumliche Pulsaddition die Aufteilung der Verstärkung auf parallele Verstärker bezeichnet, wird als zeitliche Pulsaddition die Verstärkung von Pulszügen in einem Verstärker mit anschließender Pulsaddition bezeichnet, was den Kern der Arbeit darstellt. Hierbei wird ein (gestreckter) Puls mit Hilfe von optischen Verzögerungsstrecken in eine Sequenz von Pulsen aufgeteilt, womit die Pulsspitzenleistung gesenkt und folglich nichtlineare Effekte im Verstärker reduziert und damit die Energieextraktion erhöht werden kann. In diesem Zusammenhang wurden auf Polarisationsstrahlteiler basierende Verzögerungsstrecken zur Pulsaufteilung und -kombination analysiert. Des Weiteren wurden auftretende Effekte in Verstärkersättigung diskutiert und passiv-stabilisierte Anordnungen, bei denen Pulsaufteilung und -addition mit den gleichen Elementen geschieht, untersucht. Es wurde gezeigt, dass diese in Bezug auf Energieextraktion stark begrenzt sind. Aus diesem Grund wurde eine aktiv-stabilisierte Anordnung demonstriert, bei welcher die Elemente der Pulsaufteilung und -kombination getrennt werden, was eine Kompensation der Sättigungseffekte und damit eine höhere Kombinationseffizienz ermöglicht. Methoden der aktiven Stabilisierung wurden diskutiert und es wurde eine für zeitliche Pulskombination charakteristische Bistabilität entdeckt, welche durch eine gezielte zeitliche Filterung des Detektionssignals behoben werden kann. Schließlich wurde die räumliche und zeitliche Pulsaddition in einem aktiv-stabilisierten und skalierbaren Hochleistungsfaserlaser mit acht Verstärkerkanälen und vier zeitlich kombinierten Pulsen demonstriert. Es konnten Pulse mit 12 mJ Energie und weniger als 300 fs Pulsdauer bei einer mittleren Leistung von 700 W erzeugt werden. Dieser Laser liefert mehr als 35 GW Spitzenleistung. Sowohl die Pulsenergie als auch die Kombination von Pulsenergie und mittlerer Leistung stellt aktuell den Rekord für Faserlaser dar.

Danksagung (Acknowledgements)

Ehrenwörtliche Erklärung

Ich erkläre hiermit ehrenwörtlich, dass ich die vorliegende Arbeit selbständig, ohne unzulässige Hilfe Dritter und ohne Benutzung anderer als der angegebenen Hilfsmittel und Literatur angefertigt habe. Die aus anderen Quellen direkt oder indirekt übernommenen Daten und Konzepte sind unter Angabe der Quelle gekennzeichnet.

Bei der Auswahl und Auswertung folgenden Materials haben mir die nachstehend aufgeführten Personen in der jeweils beschriebenen Weise unentgeltlich geholfen:

1. Cesar Jauregui Misas: Berechnung der Wellenleiterdispersion in optischen Fasern

2. Fabian Stutzki und Hans-Jürgen Otto: Bereitstellung von Skripten zur Bilderstellung mit Hilfe der Software MATLAB

3. Die Koautoren der entsprechenden Publikationen bei den durchgeführten Experimenten

Weitere Personen waren an der inhaltlich-materiellen Erstellung der vorliegenden Arbeit nicht beteiligt. Insbesondere habe ich hierfür nicht die entgeltliche Hilfe von Vermittlungs- bzw. Beratungsdiensten (Promotionsberater oder andere Personen) in Anspruch genommen. Niemand hat von mir unmittelbar oder mittelbar geldwerte Leistungen für Arbeiten erhalten, die im Zusammenhang mit dem Inhalt der vorgelegten Dissertation stehen.

Die Arbeit wurde bisher weder im In- noch im Ausland in gleicher oder ähnlicher Form einer anderen Prüfungsbehörde vorgelegt. Die geltende Promotionsordnung der Physikalisch-Astronomischen Fakultät ist mir bekannt. Ich versichere ehrenwörtlich, dass ich nach bestem Wissen und Gewissen die reine Wahrheit gesagt und nichts verschwiegen habe.

Jena, 8. Dezember 2017   Marco Kienel